8-2012

Phase Control in Atomic Coherence

Utsab Khadka
University of Arkansas, Fayetteville

PHASE CONTROL IN ATOMIC COHERENCE

PHASE CONTROL IN ATOMIC COHERENCE

A dissertation submitted in partial fulfillment
of the requirements for the degree of
Doctor of Philosophy in Physics

By

Utsab Khadka
Hope College
Bachelor of Science in Physics, 2006

August 2012
University of Arkansas

ABSTRACT

In this thesis, atomic coherence is used to enhance nonlinear optical processes in multi-level atoms. The multi-photon transitions are driven resonantly, and at the same time without absorptive losses, by using electromagnetically induced transparency (EIT), thereby allowing the study of $\chi^{(3)}$ and $\chi^{(5)}$ nonlinearities using weak driving fields. The coherently modified probe beam(s) and the atom-radiated signal fields arising from four- and six- wave- mixing (FWM and SWM) processes are measured in the spectral, temporal and spatial domains.

In a three-level ladder-type atomic system, multiple peaks having spectral asymmetries are observed in the EIT window as well as in the FWM signal waveforms due to the diverse multiplicities of the participating atomic states. Using phase control tailored in the frequency domain, we demonstrate all-optical methods to control these spectral waveforms and discuss applications involving waveform-shaping and metrology. For the EIT study we demonstrate a switching of multiple dark peaks into bright peaks via phase-control of interferences in the underlying dark-states. In the FWM study we demonstrate all-optical spectral line shape symmetrization, linewidth narrowing and bandwidth switching.

In a four-level inverted-Y-type atomic system, we drive and measure coexisting and phase-matched FWM and SWM signals. By using precision control of the relative phase and amplitude between these two processes of different nonlinear orders, we demonstrate phase coherence between them. First, a single-phase measurement is performed in the temporal and spatial domains, and the interferogram is used to measure the resonant frequency of the $5D_{5/2}$-$5P_{3/2}$ atomic transition in ^{85}Rb. Second, the method is extended to realize a capacity for two-phase measurement. In this case, the spectral bandwidth of the signal is modified in order to

measure the phase-shift occurring in one Mach-Zehnder interferometer, while the intensity of the total signal waveform measures the phase-shift occurring in a second interferometer.

Finally, we demonstrate phase-dependent spatial fusion between two ultra-weak optical fields by using a strong coupling field to first convert the weak fields into bosonic dark-state polaritons, which are then steered into a common all-optical waveguide mode arising due to the coupling field's intensity distribution and the resulting cross-Kerr refractive index gradient.

This dissertation is approved for recommendation to the Graduate Council.

Dissertation Director:

_____

Professor Min Xiao

Dissertation Committee:

_____

Professor William Harter

_____

Professor Gregory Salamo

_____

Professor Surendra P. Singh

_____

Professor Craig Thompson

DISSERTATION DUPLICATION RELEASE

I hereby authorize the University of Arkansas Libraries to duplicate this dissertation when needed for research and/or scholarship.

Agreed _____

Utsab Khadka

Refused _____

Utsab Khadka

ACKNOWLEDGMENTS

First and foremost, my immense gratitude goes to my research advisor Professor Min Xiao for accepting me in his very active, productive and selective research group. He has been very generous with his time, patience and wisdom, and has guided my growth as a researcher. His high standards and expectations, combined with his encouragement of my efforts and talents, have positively influenced my drive and enhanced my research productivity.

I thank all members of my advisory committee for their encouragement and help throughout the years. I have frequently visited them with research questions and they have always been extremely welcoming, and I have benefited a lot from those discussions.

The person who first introduced me to the ideas of EIT and multi-wave mixing and taught me how to observe these processes experimentally was Dr. Yanpeng Zhang, a postdoc working in Prof. Xiao's lab when I first joined. It is during my training with him that I learned about the various tools and techniques used in a nonlinear optics experiment including lasers, multi-beam alignment methods, data detection and analysis. My work during this phase became material for five articles.

I have also benefited from the visiting scholars and students that Prof. Xiao's lab constantly attracts. One of my most fruitful collaborations was with Huaibin Zheng, a one-year visiting student, whose confidence and efficiency while performing experiments has been contagious. Our collaboration resulted in material for four articles. I also benefited from discussions with Dr. Jing Zhang, a visiting scientist for one semester, on several occasions.

After Huaibin left, I had sole access to our experimental facilities for a while, during which time I tested various new ideas. Our lab then had another visiting scientist, Dr. Xihua

Yang, with whom I had many fruitful discussions. During this time, I also frequently collaborated with Jason (Jiteng) Sheng, a graduate student typically working in a different experiment (ring-cavity setup) in a different optics table. We frequently helped each other out with ideas and skills, and during this time our collaborations yielded material for another five articles. I must also thank Dr. Haibin Wu for sharing his postdoctoral application experience with me.

Besides my experimental collaborators and trainers, I have also learned immensely from the other professors in the department, whose wonderful teachings as well as out-of-class discussions have been a huge part of my education. I must also thank Dr. Gay Stewart, Dr. John Stewart and Dr. William Oliver, whom I worked for as a teaching assistant for several years. Besides helping me become good at teaching, they have also been sources of invaluable help and advice throughout my graduate years.

Finally, I cannot even put to words the immense source of support my parents have been for me. Their belief in me, their constant encouragement, and their never failing warmth and presence despite our continental separations, have been the greatest blessings. The same applies to my younger sister, and it has been a pleasure watching each other's academic progress over the decades. I would also like to thank all my relatives, as well as my friends, colleagues and acquaintances that I have met over these years, for their kind encouragement and best wishes.

...to my

father Dr. Rup Khadka,

mother Mrs. Anita Khadka,

and sister Ms. Upasana Khadka.

TABLE OF CONTENTS

I. Introduction

Much progress has been made in quantum and nonlinear optics to control the flow of electromagnetic radiation near optical frequencies, and to coherently manipulate its various degrees of freedom[1-4]. One of the main motivations for this effort is the fact that light is a highly desirable medium for communication and information processing, both optical and quantum. This is because, apart from its high speed and ability to travel vast distances without losing coherence, light can also carry quantum information in its various degrees of freedom making it a key ingredient in quantum-enhanced technologies. Due to its high frequency and short wavelength, it offers great temporal and spatial resolutions in measurements, standards and interferometry[5]. Many applications can be realized by gaining control over the various parameters of light such as its amplitude, phase, frequency, velocity, direction and polarization in the Fourier, temporal and spatial domains.

However, controlling the flow of light is not trivial. It can propagate in vacuum, but unlike other particles with mass, charge, electric or magnetic moments, photons do not interact with each other in vacuum. Photons do couple with matter via the electromagnetic interaction, but this interaction is often accompanied by incoherent effects such as dissipation making storage and controlled flow difficult. Even when dissipation is small, there are other effects such as dispersion, diffraction and diffusion that have to be assessed.

The interactions of light with matter, including the processes that are incoherent and detrimental to the controlled flow of light, and methods to overcome them, have been well investigated. To date, one of the most promising mediums for such coherent control seems to be multi-level atoms. The interaction between light and atoms increases exponentially near atomic

resonances. Due to the many available quantized transitions, multi-level atoms can interact strongly with disparate photons or light fields simultaneously, thereby serving as effective hosts for multi-photon interactions and higher-order nonlinear optical processes[6-9]. Using atomic coherence to attain dark states and electromagnetically induced transparency[10-35] (EIT), it is possible to manipulate the flow of light such as to eliminate dissipation, drastically slow or increase its group velocity, store it, and suppress its transverse diffraction. Atomic coherence also facilitates dissipation-free resonant enhancement of multi-wave mixing processes[36-65] (MWM), in which multiple light waves are mixed together by the atomic nonlinearity and new waves are reradiated. These new signal waves can be very useful since their degrees of freedom can be precisely controlled using all-optical means, and also because they contain information about the input waves. In these phenomena, quantum interference, both constructive and destructive, plays a crucial role[66-88]; much can be achieved by incorporating phase-control in the interaction of multi-level atoms and light waves.

My research at the Quantum and Nonlinear Optics Laboratory at the University of Arkansas, Fayetteville has mainly involved investigating multi-wave mixing processes mediated by atomic coherence in multi-level atoms. A significant proportion of the attention has been given to phase-control in these processes. Experiments were conducted to observe phase-dependent effects in the spectral, temporal as well as spatial domains and various interesting and potentially useful features were observed. This thesis describes the various experiments performed and the phenomena observed. Before going into the details, in this introductory section, in the simplest "layman" terms, a brief overview will be given of the basic concepts that will be discussed in the rest of the chapters of the thesis.

I.1 Dark states and electromagnetically induced transparency (EIT)

Three-, four-, and in general multi- level atoms offer more degrees of freedom in the way we can alter the flow of a light beam compared to a two-level atomic system. In this section, the two-level atom is first reviewed very briefly. Some important superposition of states occurring in multi-level atomic systems are discussed next, which will be referred to in the subsequent sections and chapters.

I.1.A Two-level atom-field interaction

Many textbooks and references have discussed the interaction between optical fields and two-level atoms[1,4,89], which displays a vast array of interesting phenomena such as saturation, hole-burning, ac-Stark shifting and Autler-Townes splitting, Rabi flopping, spin echo, … We will not be discussing two-level systems in this thesis. We will summarize the basic features of these systems in this section, so as to supplement the subsequent discussions about three-and four-level systems.

When a light wave with electric field **E** flows through a volume containing two-level atoms, it interacts with the atom's electric dipole moments. This interaction is strongest for the Fourier components of the field near atomic resonance. Typically, two-level atoms incoherently scatter photons in all directions, decreasing the output intensity of the light in the original spatial mode. This attenuation of resonant light's intensity occurs rather rapidly along the beam's path; the intensity decays exponentially with the absorption length αL, where L is the geometric length and the absorption coefficient α depends primarily on the atomic density, the dipole transition

strength and the frequency detuning. The absorption line shape depends on several factors such as the natural linewidth of the excited atomic state, the thermal distribution of the atomic ensemble, collisions and the atomic time-of-flight. Accompanying this field attenuation is the field's dispersion across atomic resonance, characterized by the dispersion coefficient β which is related to α via the Kramers-Kronig relations. Both α and β are succinctly contained in the atomic ensemble's linear susceptibility $\chi^{(1)}$, a complex quantity related to the macroscopic polarization via $\mathbf{P} = \varepsilon_0\chi^{(1)}\mathbf{E}$.

The susceptibility can be modeled by using the 2 x 2 Hamiltonian and the density-matrix treatment. The field propagation can be calculated by using the atomic polarization and the Maxwell's equations. Experimentally, the absorption can be determined directly by measuring the transmitted field at the output by a photodiode, and the dispersion can be measured by Mach-Zehnder interferometry of the transmitted field with a free-space reference field.

I.1.B Three-level atom-field interaction and dark states

Single-photon electric dipole transitions can take place only between dipole-allowed atomic energy levels, and the two states of the two-level atom discussed above must have opposite parity. However, by using two-photon processes, photonic transitions can also be induced between dipole-forbidden energy levels that have the same parity. This allows, for instance, resonant transitions between two long-lived states (such as Raman configuration or between a ground state and high-lying states of same parity) using optical fields. The transition amplitudes of such two-photon processes are greatly enhanced when a third real energy level is used as an intermediary resonance[111]. Two-photon-resonant interactions resonantly enhanced by an

intermediate state comprise a very important class of processes in atomic and optical physics, and various three-level atomic configurations have been extensively investigated. Two such configurations, the so-called lambda-type and ladder-type systems, are shown in Fig. 1.

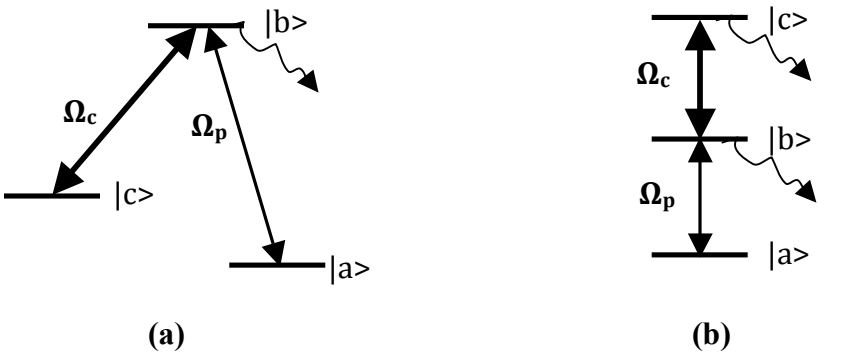

Fig. 1. Three-level (a) lambda-type and (b) ladder-type atomic level configurations. A two-photon transition is driven between the levels $|a\rangle$ and $|c\rangle$ via the intermediate level $|b\rangle$, by two optical fields with Rabi frequencies Ω_p and Ω_c. All three energy levels are real. The wavy arrows represent radiative decay.

The main utility of the three-level atomic system is that it allows for the coherent control of one light beam characterized by Ω_p, typically weak, by using a stronger light beam characterized by Ω_c to steer the atomic response. By manipulating the interference between the various quantum mechanical pathways existing in this two-photon three-level system, a rich variety of phenomena have been realized including that of dark states[12-15, 23]. In dark states, the interaction of the fields and the atoms prepare the resultant system in a quantum superposition of states which is decoupled from the fields, thus quenching absorption, increasing the beam

transmissions and making the atomic medium appear dark. In Fig. 1, the system may be driven into two possible superpositions of the initial and final levels:

$$|NC\rangle = \frac{1}{\Omega}\left(\Omega_c|a\rangle - \Omega_{\mathrm{p}}|c\rangle\right)$$

$$|C\rangle = \frac{1}{\Omega}\left(\Omega_c|c\rangle + \Omega_{\mathrm{p}}|a\rangle\right)$$

where $\Omega = \sqrt{{\Omega_c}^2 + {\Omega_p}^2}$ is the effective total Rabi frequency. We remind that the Rabi frequency can be viewed as a measure of the coupling between the optical field's electric field and the electric dipole moment of the atomic transition: $\Omega_p = -\frac{\mu_{ba}.E_p}{\hbar}$ and $\Omega_c = -\frac{\mu_{bc}.E_c}{\hbar}$.

Unlike the bright state $|C\rangle$, we see that the dark state $|NC\rangle$ is not coupled to the intermediate energy level $|b\rangle$, since $\langle NC|b\rangle = 0$. This implies that when the dark state is driven, the atomic population does not reside in state $|b\rangle$, and thus the radiative decay does not deplete the optical field from its original mode of propagation, as would happen in incoherent fluorescence scattering during two-level-atomic absorption. When the relative strengths of the beams satisfy $\Omega_c >> \Omega_p$, the dark state results in EIT, discussed in the next section. There is broad interest to be able to generate these superpositions at the single photon level for quantum applications, and in fact many experiments have already been demonstrated for few-photon EIT and even vacuum-induced transparency[90].

I.1.C Electromagnetically induced transparency (EIT)

While absorption across resonance in a two-level atom is a powerful spectroscopic tool and much effort has been spent in improving signal resolution and precision (for instance in atomic clocks), the attenuation of the field at resonance right when higher-order transition amplitudes get the biggest boost can be troublesome for other applications such as multi-photon transitions. EIT, initially observed in the works of Hansch[10] as well as Harris[11,12], helps to circumvent the linear absorption of light even as it propagates resonantly through a dense atomic medium which is otherwise absorbing and opaque in the absence of EIT. At EIT, which is attained when $\Omega_c >> \Omega_p$, the resonant atomic medium is transparent to the probe field even when the atomic population resides in the state $|a\rangle$. By suppressing linear absorption, EIT allows for better efficiency (signal output compared to the input energy) and resolution (signal strength compared to the line width, less background noise) in nonlinear wave mixing processes.

Along with the drastic modification of α, EIT also alters the dispersion strongly. The steep and normal dispersion across EIT resonance has been measured by Xiao et al[16], and the accompanying reduction in the group velocity v_g of the light has been measured by many groups, including the value of 17 m/s measured by Hau's group in ultracold atoms[22]. A reduced v_g also means a spatial compression of the light pulse, and several groups have managed to completely stop the pulse inside an atomic sample much smaller than the free-space pulse length, such that the stored pulse can be retrieved later without loss of coherence of initial information[23-32]. Coherent phase manipulation of the light pulse while it is stored amongst the atoms has also been demonstrated. These demonstrations are important steps towards the realization of quantum memory and information processing.

To achieve EIT, one needs a three-level atomic medium as shown in Fig. 1, a weak probe beam and a strong coupling beam with the condition $\Omega_c >> \Omega_p$. In the Fourier domain, both one-photon and two-photon resonances (TPR) should be satisfied. Even when the atomic medium is a Doppler-broadened thermal ensemble, a judicious spatial arrangement of the two beams will allow for a Doppler-free EIT window. For instance, for the ladder–type (lambda-type) configuration, the sum-frequency (difference-frequency) of the two beams should correspond to the transition frequency between the two dipole-forbidden states being coupled, and the two beams should be counter-propagating (co-propagating) in order to satisfy TPR and to get a Doppler-free TPR resonance, respectively. The EIT profile in an inhomogeneously broadened ladder-type atomic medium has been solved analytically, and the following equation contains all the properties discussed in this paragraph[17]:

$$\chi(v)dv = \frac{\frac{4i{\mu_{21}}^2}{\varepsilon_o}}{\gamma_{21} - i\Delta\nu_1 - i\frac{\omega_p}{c}v + \frac{\frac{{\Omega_c}^2}{4}}{\gamma_{31} - i(\Delta\nu_1 + \Delta\nu_2) - \frac{i(\omega_p - \omega_c)v}{c}}} N(v)dv$$

Here, the intergration is performed over the atomic velocity groups v in the thermal distribution N(v). μ_{21} is the electric dipole moment of the probe-driven transition, ε_0 is the vacuum permittivity, Ω_c is the Rabi frequency of the coupling beam, $\omega_p = 2\pi\nu_p$ and $\omega_c = 2\pi\nu_c$ are the frequencies of the probe and coupling beams, and γ_{21} and γ_{31} are the natural linewidths of the transitions driven by the probe beam, and the sum of the probe and coupling beams, respectively. $\Delta\nu_1$ and $\Delta\nu_2$ are the frequency detunings of the probe beam and the coupling beam from their respective atomic transitions, respectively.

I.1.D Four-level atom-field interaction

Even more coherent control can be exerted using four atomic levels instead of only three. Several four-level configurations have been investigated, some of the most popular being N, double-lambda and inverted-Y. In the N-level atomic system, a third "control" beam can be used to modulate the three-level, two-beam EIT of the regular lambda scheme. The advantage of such a system is that drastic alterations to the EIT, as well as enhanced nonlinearities, can be achieved even when the control beam consists of only a few photons. The double-lambda scheme has been one of the most popular systems for investigating four-wave mixing processes, as it allows embedding an EIT resonance in one Raman transition, allowing FWM transition even at low light levels.

In this thesis, we have made several uses of the inverted-Y atomic configuration. In Ch. 2, interference between various dark-states generated in this configuration are studied, and the consequences to the transparency experienced by the probe beam are described both theoretically and experimentally. In Ch. 5 and 6, we use this system to realize coexisting nonlinearities of different orders, and study their mutual interactions. The relative strengths, as well as the relative phases of such coexisting nonlinearities, are tuned via the parameters of the driving beings that couple the various states.

I.2 Enhanced nonlinearity in atomic media

A plethora of nonlinear optical phenomena were discovered immediately following the birth of the laser in 1960, beginning with the observation of second harmonic generation[91] in 1961. To understand the lack of such observations in pre-laser era, one needs to consider the polarization of matter[3,4]:

$$P_i = \varepsilon_0 \chi_{ij}^{(1)} E_j + \varepsilon_0 \chi_{ijk}^{(2)} E_j E_k + \varepsilon_0 \chi_{ijkl}^{(3)} E_j E_k E_l + \ldots$$

The material polarization P is the source term in Maxwell's equations, which describe the propagation of electromagnetic radiation as well as its interaction with matter. Here, $\chi^{(n)}$ are the various orders of the susceptibility, and the subscripts are the Cartesian components. Each higher order term of the susceptibility is several orders of magnitude weaker than the previous order. As a result, for weak optical fields, the linear polarization is dominant and it is difficult to observe phenomena arising from higher orders. As the field E becomes stronger, the linear polarization grows linearly with E, whereas the n^{th} order of the polarization increases polynomially with E. As a result, higher-order effects of the polarization, despite the very weak susceptibility coefficients, start to become observable when the intensity becomes large. The optical intensities required for such observations were provided by lasers.

Different orders of the polarization give rise to different effects, and different materials have been studied such as crystals, atoms and molecules. Depending on the symmetry of the constituent particles of the material medium, some orders of the nonlinearity can be vanishing.

Because alkali atoms are centro-symmetric, the even orders of the susceptibility are vanishing. In this thesis, all the investigations are done using thermal ensembles of rubidium atoms, for which the lowest non-vanishing orders of the electric susceptibility are $\chi^{(1)}$, $\chi^{(3)}$ and $\chi^{(5)}$. In general, $\chi^{(n)}$ is responsible for the mixing of (n+1) waves. For instance, $\chi^{(3)}$ enables four-wave mixing (FWM) and $\chi^{(5)}$ enables six-wave mixing (SWM). Most of the subsequent chapters deal with these multi-wave-mixing (MWM) interactions; we will briefly discuss them below.

I.2.A $\chi^{(3)}$ and four-wave mixing (FWM)

As a very basic definition, FWM is a process where four different waves interact coherently via a medium. These waves do not necessarily have to be electromagnetic; FWM with matter waves have also been demonstrated[92-94]. In this thesis, we deal with FWM of optical waves with atomic ensembles serving as wave-mixers. Various schemes have been used in generating FWM radiations from atomic ensembles. In these processes, the atomic nonlinearity interacts with four electromagnetic fields (distinguishable, for instance, by their directions, frequencies, or the atomic transitions that they drive). Out of these fields, some are externally applied upon the nonlinear medium by using laser sources, while some are generated by the medium; the generated field can be due to the parametric amplification of an initially vacuum mode, as well as the amplification of one of the external driving beams. Depending upon the atomic system and the geometry being used (such as ladder or double-lambda type systems, or the presence of a cavity mode), the number of external driving fields can range from three, two and even only one[95].

In the FWM experiments described in this thesis, three external optical fields $\mathbf{E_i} = A_i e^{-i(\omega_i t - \mathbf{k_i} z + \Phi_i)} \hat{\boldsymbol{e}}_i + \boldsymbol{c.c.}$ with i= 1, 2, 3 are incident on the atomic medium. Here A, ω, k, Φ and $\hat{\boldsymbol{e}}$ are the beam's electric field amplitude, angular frequency, wavevector, phase, and polarization respectively. The waves couple with the third-order nonlinearity of the medium, and the resulting nonlinear polarization $P^{(3)} = \chi^{(3)} \mathbf{E_1 E_2 E_3}$ serves as a source term in Maxwell's equation, thus giving rise to a fourth field $E_f = A_f e^{-i(\omega_f t - \mathbf{k_f} z + \Phi_f)}$. It is clear that the parameters of this new field are governed by the parameters of the incident fields: $\omega_f = \sum \omega_i$, $\mathbf{k}_f = \sum \mathbf{k}_i$, $\Phi_f = \sum \Phi_i$. These phase-matching conditions arise from the conservations of energy and momentum. Careful geometric alignment of the beams and detectors are critical during the experimental setup in order to satisfy these phase-matching criteria before the weak FWM signal can be observed. In addition, the polarization of the fields must satisfy conservation of angular momentum.

EIT resonances are included in the parametric amplifiers in order to resonantly enhance the multi-photon transition amplitudes with suppressed losses for both driving and generated fields, as well as to attain low background noise and high resolution[36-65]. In the absence of these dark-states, the use of resonantly enhanced nonlinear transition amplitudes is also accompanied by resonantly enhanced absorption and losses. In order to overcome the losses, very high-powered pulses typically have to be used, and such nonlinear optical processes can be quite inefficient. Such high-powered and spectrally broad driving pulses also give rise to power-broadening effects, spurious transitions and background noises. The use of EIT, on the other hand, allows for resonantly enhanced multi-photon transitions with vanishing absorptive losses, thus making it possible to drive nonlinear optical processes with low-powered and spectrally narrow continuous-wave beams. Not only does this improve the efficiency of nonlinear optical

conversion, but low-powered driving beams also mean small power-broadening and low background noises, giving rise to high signal-to-noise ratios. Furthermore, by carefully designing phase-matching geometries such as counterpropagating signal and driving beams with orthogonal polarizations, it is possible to have minimal background scattering at the location of the signal detector, thus enhancing the sensitivity and precision of the measurements. More details about EIT-enhanced FWM processes will be presented in chapter 3. Different experimental schemes are described in the subsequent chapters that enable enhanced nonlinear optical processes.

Over the past decades, many interesting and important features have been demonstrated using EIT-assisted coherent FWM processes. They have been used for maximally efficient frequency conversion at optical frequencies. They have proven to be efficient sources for squeezed radiation and correlated photons[53-56]. In certain schemes where the FWM signal gain is accompanied by an amplification of an initially weak probe field, the noises in the two amplified signals have shown to have classical as well as quantum correlations and even entanglement. Using the steep dispersion of a second EIT medium to reduce the speed of one of the correlated fields, a tunable temporal delay of the entanglement has also been demonstrated. Furthermore, the quantum correlations are shown to hold for different spatial modes contained within the spatial bandwidth of the FWM gain medium, thus opening the way for multimode quantum imaging, information processing and communication. Similar to the storage of a weak probe pulse in an EIT medium, a simultaneous photonic memory for FWM signal has also been demonstrated[52,57]. Thus coherently enhanced FWM processes constitute an active area of research with important prospects for future applications involving the generation, storage and manipulation of optical fields for classical as well as quantum applications. Most of the work

presented in the subsequent chapters were performed with the aim of contributing new perspectives and methods to this important field.

I.2.B $\chi^{(5)}$ and six-wave mixing (SWM)

In some experiments presented in this thesis, we drive SWM transitions, which arise due to the fifth order nonlinearity, i.e. the term coupled to the $\chi^{(5)}$ susceptibility. The method implemented in driving SWM is similar to the one used to drive the FWM transitions, i.e. a dark-state resonance is embedded in the transition pathway so that the weak nonlinear process can be driven resonantly and without absorptive losses. The difference is that now six optical fields are mixed instead of only four, thus increasing the number of resources (driving beams) required and the experimental complexities of additional phase-matching and beam alignment.

In studies where nonlinear optics is performed at high optical intensities, $\chi^{(5)}$ is often found useful in the generation of stable high-dimensional solitons[138, 147]. The reason is that its sign is opposite to that of $\chi^{(3)}$, and it acts as a source of saturable nonlinearity, preventing collapse of a self-focusing beam which happens in a purely Kerr medium with $\chi^{(3)}$.

I.2.C Coexisting multi-wave-mixing (MWM) processes

Due to the many available energy levels and transitions in a multi-level atom, the same atomic cloud can be used to drive multiple MWM processes simultaneously, for instance coexisting FWM processes, or coexisting FWM and SWM processes. These various processes typically

share some driving beams. In such coexisting systems, interesting mechanisms such as competition for energy, transfer of energy, varying gain thresholds at various atomic densities, correlations and anti-correlations in the signal amplitudes, have been measured[47-51, 61-63]. Besides energy dynamics, the phase-coherence between such processes is also an intriguing feature.

In general, when a $\chi^{(5)}$ process is driven, lower-order $\chi^{(3)}$ subsystems are also driven. Since the lower order term is much stronger than the higher order term, for lower-intensity driving beams, the driven FWM signal remains very strong compared to the SWM signal. In order to observe the SWM signal, we implement methods where we can spatially isolate the signals and tune their transition amplitudes individually such that the FWM signal can be made equal to, or even weaker, than the SWM signal. In this process, while the relative amplitude of the two signals can be tuned via the strengths of the driving beams, the relative phase between the signals can also be tuned via the phase of the driving beams. We experimentally demonstrate that these coexisting signals are phase-coherent, which is a consequence of the underlying atomic coherence and the coherence of the driving laser fields.

Such amplitude and phase control between coexisting nonlinearities is an invitation for new interferometric methods, which we discuss in the next section.

I.3 Phase control

In the previous sections, it was seen that the phase of the FWM and SWM signals depend on the phases of the input waves that are mixed in the nonlinear wave-mixing process. This property has two main implications. The first is that by using precision control for the relative phases of the input beams, the phase of the atom-radiated field can be precisely controlled. The second is that by measuring phase changes in the signal field, any unknown phase changes in one of the

input driving beams can be inferred. The first implication is useful in the generation of high-resolution phase-modulated signals using all-optical methods. The second implication is the use of the atomic nonlinearity as a phase-sensitive interferometer for the input beams. Both of these features will be studied in chapters 4, 5 and 6.

In Ch. 4, we describe a method of external all-optical phase control for the Fourier-domain waveform shaping of the atom-radiated field[59]. Here, a spectral-domain phase-evolution of the signal field is achieved by implementing precision control of the relative path length between the two frequency-swept driving beams.

When multiple nonlinear transitions are driven simultaneously using shared atomic levels and beams, it is possible to couple the nonlinearities so that they interfere. Phase control between the driving beams become even more important when the atom-radiated signal fields arising from the nonlinearities are phase-matched and spatially overlapped. Phase-control between coexisting $\chi^{(3)}$ and $\chi^{(5)}$ processes will be the subject of Ch. 5 and 6. In Ch. 5, using precision phase-control and interferometry, the phase-coherence between two nonlinearities of different orders is demonstrated[58]. Spatial as well as temporal interferences are measured between the overlapped FWM and SWM signals, and the temporal fringe period yields the resonant frequency of the $5D_{5/2}$-$5P_{3/2}$ atomic transition in ^{85}Rb. In Ch. 6, the capacity of coupled nonlinearities to measure multiple interferometers simultaneously is demonstrated[65].

In Ch. 7, we experimentally demonstrate the fusion of two in-phase optical fields having ultra-weak intensities. In order to steer the initially spatially separate weak beams towards each other, we utilize quantum coherence effects induced by a strong coupling beam in a three-level atomic medium. Once the weak fields are steered into the common all-optical waveguide, they show phase-dependent outcomes. In the case of fusion, the output intensity can be all-optically

tuned via the intensity of the coupling beam. When the fields are out-of-phase, they do not deflect like self-guided solitons do, but are instead confined tightly to the waveguide's center, while the waveguide's center itself remains dark.

I.4 Spectral, temporal and spatial waveforms

In the various experiments discussed in the subsequent chapters, we will describe ideas, methods and measurements in three different domains: spectral, temporal and spatial. In this section, we will categorize the chapters with their associated domains. We note that while the setups of each experiment require carefully controlled parameters in all of the domains, such as appropriate spatial phase-matching, correct frequency detunings and temporally synchronized processes and measurements, the following categorization is mostly for the domain in which the final results are measured.

We also note that most of the results presented in this thesis have already been published in peer-reviewed journals. As a result, the experimental results, figures and most of the descriptions of the methods presented in these chapters will be similar to the published articles. Below, we will also include references to the published articles corresponding to the results of the chapters.

Chapters 2, 3 and 4 deal with spectral waveforms and the phase-control of such waveforms for the EIT window and FWM spectra in a mixed multi-level atomic system[34, 64, 59].

In Ch. 5, we use phase-control of FWM and SWM in the temporal and spatial domains, obtaining a spatial-temporal interferogram[58].

In Ch. 6, we design a method of two-phase interferometry by shaping the spectral waveform of coexisting FWM and SWM signals[65].

In Ch. 7, a phase-dependent fusion between two weak optical fields is investigated in the spatial domain. The work presented in this chapter will be submitted for publication shortly.

While the temporal and spatial evolutions of fields involved in nonlinear optical processes show interesting and important phenomena, we note that most of the measurements in this thesis are conducted in the spectral domain. We study, as well as manipulate, the spectral bandwidths of these processes to understand and develop useful features and novel applications. A possible future extension of these discussed works will be to investigate quantum correlations between multiple spectral modes of two coexisting parametrically amplified fields, in conjunction to their already demonstrated spatially multi-mode correlations[54-56], thus vastly increasing the dimensionality for quantum information processing and communicating.

II. Dark-state phase manipulation in EIT

II.1. Introduction

In the introductory section, we introduced electromagnetically induced transparency (EIT) in a purely three-level atomic medium. In realistic atoms, each of the three driven energy levels can have various sublevels and degeneracies, giving rise to complex features in the spectral waveform of the EIT window. By "EIT window", we are referring to the spectral structure of the transparency that arises in the transmission of the probe beam as its frequency is being scanned across an absorbing line in the presence of a coupling beam whose frequency is held fixed at a neighboring dipole transition. Even though the probe beam's absorption line is spectrally broad (~GHz) in a Doppler-broadened atomic ensemble, a careful alignment of the coupling beam can result in an EIT window that is Doppler-free (~MHz). In a lambda-type configuration, it is possible to find combinations of energy levels and light polarizations that result in the ideal three-level system to a very good approximation, apart from the ac-Stark shift induced by closely lying hf sub-levels in the intermediate state[22]. In this case, the EIT window consists of a single peak. The reason is that the two ground states being probed are the only two hyperfine (hf) levels of that fine structure, and there are no other closely lying hf levels in the vicinity.

However, in a ladder-type configuration in which the upper excited state is one of the fine structures of the 5D state, there are many hf levels that lie very close in energy separation. Because the spectral separations between these levels are comparable to their linewidths, it is not possible to get a truly three-level resonance in the ladder-type configuration. Instead, we have many three-level systems lying close to each other and contributing to the resulting transparency of the probe beam. When the probe beam's frequency is scanned across the absorption transition,

the sum-frequency with the coupling beam now comes into two-photon resonance (TPR) with multiple EIT transitions. We thus observe multiple peaks, unlike the single peak in the lambda-type configuration. The number of peaks depends on the number of hf levels in the upper excited state that have allowed transitions satisfying the selection rules.

We have observed that the EIT window in the transmission of the probe beam shows very dramatic changes depending on the probe beam's ellipticity. At some polarizations, the multiple transparency peaks arising due to the many hf levels of the 5D state became highly resolvable. More importantly, for another particular value of the polarization, the transparency peaks switched to enhanced absorption peaks and the position of the multi-transparency peaks switched to different spectral locations. In this chapter, we will present the experimental results as well as a theoretical model based on the interference between dark-states to explain this intriguing phenomenon.

II.2. Motivation

Most studies in EIT use combinations of linearly and/ or circularly polarized fields interacting with three or four energy levels in the atomic media[16-22]. While some studies have extended considerations to the multi-Zeeman sublevels present in realistic atoms[96-100], relatively fewer studies have considered the response of such multi-level systems in the presence of elliptically-polarized light fields[101-103]. In such studies, typically the modulations of the EIT profiles are explained by considering the asymmetry in the numbers of EIT subsystems and strengths corresponding to different beam polarizations. These studies considered the intensity distribution of the field amongst its polarization components, but not the relative phase between these

components. Also, in doing so, all the Zeeman sublevels had to be considered; for the system we are considering, that amounts to 36 magnetic sublevels.

We have measured the EIT spectral lineshape for all the polarization states for the probe beam in the ladder-type atomic configuration in a rubidium atomic vapor (Fig. 1a). In doing so, we have observed resonances that switch from dark (EIT) to bright (electromagnetically induced absorption, or EIA[104,105]), depending on the phase difference between the two circularly-polarized components of the probe beam corresponding to different elliptical polarization states. We describe this behavior as arising due to the interference between multiple dark states switching from constructive to destructive, altering the atomic populations in the dark states. An analysis based on the aforementioned asymmetry in EIT subsystems is incapable of explaining such behavior because there exist cases where the beam intensities, and hence the EIT subsystem structures, are identical, but the overall transmission profiles differ drastically. Thus, it is crucial to account for the quantum interference effects induced by the phase in the beams. Furthermore, even though our system consists of a total of thirty-six participating magnetic sublevels (Fig. 1b), we can qualitatively discuss the phase-dependent switching behavior simply by considering the inverted-Y configuration which involves only four magnetic sublevels (Fig. 1c). Our theoretical model treating the quantum interference amongst the polarization-coupled dark states in such a four-level inverted-Y atomic system agrees with the experimental observations. Such a treatment has also allowed for a more transparent understanding of the system's behavior.

We have observed that the phase-dependent switching behavior also varies with frequency, which could make the system useful for selective switching between multiple frequency channels. In a system consisting of closely lying hf levels, this feature results in multiple transparency windows all of which display a switching as we tune the relative phase

between the probe beam's polarization components. By using appropriate combinations of phases and frequencies, one could create conditions such as AND and OR gates which could find applications in optical communication and quantum information processing. The fact that this phase-controlled switching can be achieved without changing the power of any of the beams could also prove beneficial in studies where it is undesirable to completely shut off a beam in order to switch a medium from dark to bright, as is routinely done in light storage and switching experiments[24-29].

II.3. Theoretical model

II.3.A. Atomic system

Our theoretical model consists of a four-level inverted-Y configuration as shown in Fig. 1(c). The two ground states |1> and |2> are the degenerate Zeeman sublevels corresponding to the magnetic quantum numbers $m_F = -1$ and $m_F = +1$, respectively, of a ground state hyperfine level. The states |3> and |4> are the $m_{F'} = 0$ and $m_{F''} = 0$ Zeeman sublevels, respectively, of different excited states and belong to hyperfine levels between which the electric dipole transitions shown in the figure are allowed. Note that this four-level system is a sub-system of the larger thirty-six-level system shown in Fig. 1(b), which displays all the magnetic sublevels in the three-level ladder-type configuration of fine-structures that is driven by the two optical fields (Fig. 1(a)).

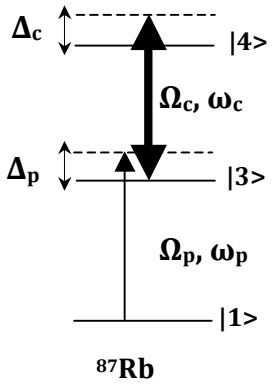
Δc
|4>
Ωc, ωc
Δp
|3>
Ωp, ωp
|1>
87Rb

Fig. 1(a)

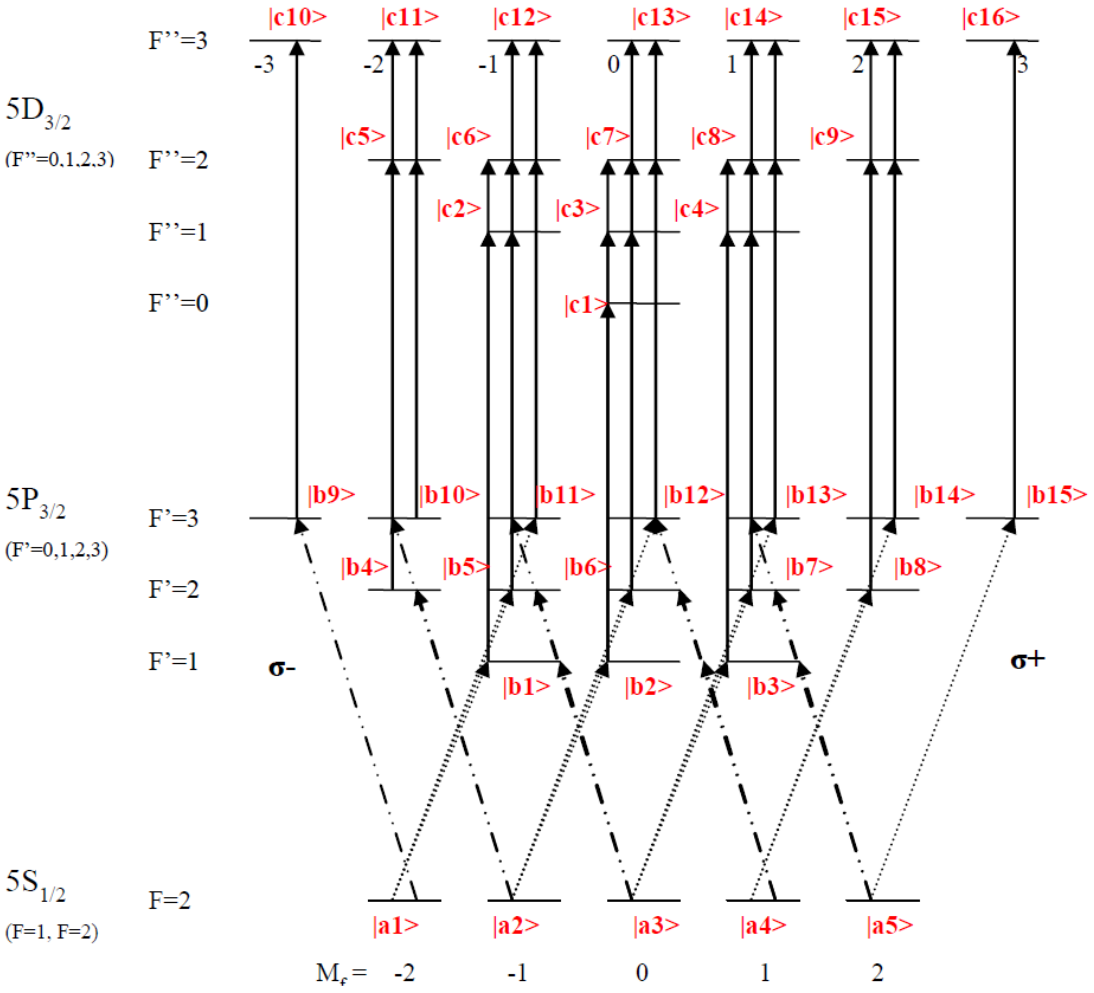
|c10>
|c11>
|c12>
|c13>
|c14>
|c15>
|c16>
F''=3
-3
-2
-1
0
1
2
3
5D3/2
(F"=0.1.2.3)
F''=2
|c5>
|c6>
|c7>
|c8>
|c9>
|c2>
|c3>
|c4>
F''=1
F''=0
|c1>
5P3/2
(F'=0,1,2,3)
F'=3
|b9>
|b10>
|b11>
|b12>
|b13>
|b14>
|b15>
|b4>
|b5>
|b6>
|b7>
|b8>
F'=2
F'=1
σ-
|b1>
|b2>
|b3>
σ+
5S1/2
(F=1, F=2)
F=2
|a1>
|a2>
|a3>
|a4>
|a5>
Mf = -2
-1
0
1
2

Fig. 1b

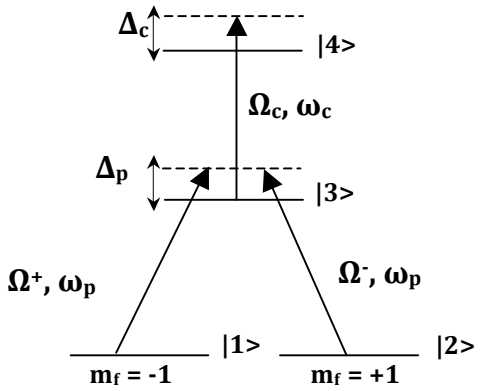

Fig. 1(c)

Fig. 1. (a) Typical three-level ladder-type configuration used for EIT. (b) In realistic atoms used in an experiment, such as ^{87}Rb, each of the three levels consist of a myriad of hyperfine and Zeeman sublevels, and need to be accounted for when the driving beams are not linearly polarized. (c) The simplified four-level inverted-Y configuration that we use in our theoretical model, which is sufficient for qualitatively explaining the experimental results.

II.3.B. Elliptically polarized probe beam

A single elliptically-polarized probe beam with frequency ω_p is used to create electric dipole transitions between |1> and |3> and between |2> and |3> at the same time. The polarization of the probe beam can be controlled by using a quarter-wave plate (QWP). An initial vertically polarized probe beam with intensity I_p and electric field amplitude $E_0 = \sqrt{\frac{I_p}{2n\varepsilon_0 c}}$ becomes

elliptically polarized after passing through the QWP that has been rotated by an angle θ. In the circularly-polarized basis, the polarized probe beam can be decomposed into $\boldsymbol{E_p = E^+\hat{\sigma}^+ + E^-\hat{\sigma}^-}$, where $\mathbf{E}^+ = \frac{E_0}{\sqrt{2}}(cos\theta + sin\theta)e^{i\theta}$ and $\mathbf{E}^- = \frac{E_0}{\sqrt{2}}(cos\theta - sin\theta)e^{-i\theta}$. Here, $\hat{\boldsymbol{\sigma}}^+$ and $\hat{\boldsymbol{\sigma}}^-$ are the unit vectors of the right-hand circularly- (RHC) and left-hand circularly- (LHC) polarized basis, respectively. Besides changing the strengths of the electric field components, we notice that the QWP also introduces a phase difference of φ = 2θ between them (Fig. 2).

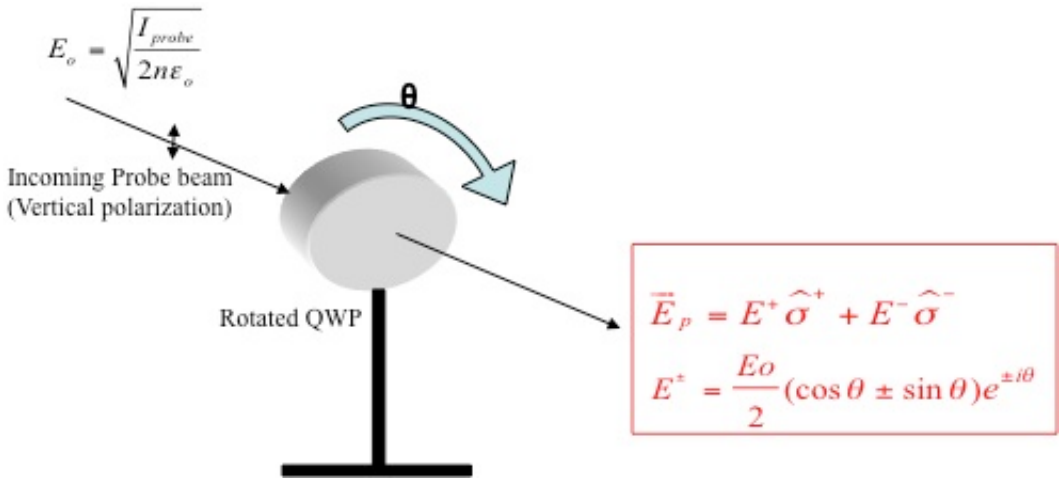

Fig. 2(a)

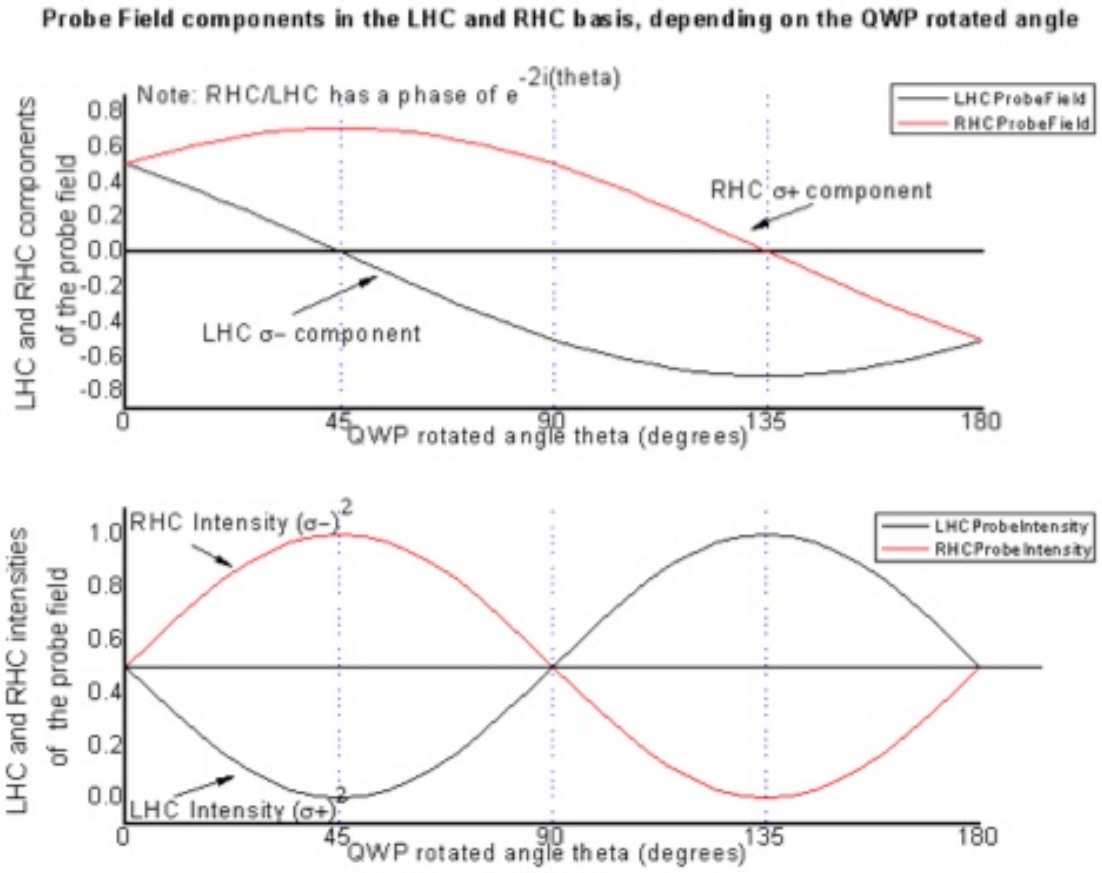

Fig. 2(b)

Fig. 2. (a) Decomposition of the probe field into its circularly polarized components after it has passed through a quarter wave plate (QWP). (b) Pictorial depiction of the field strengths (top graph), as well as the intensities (bottom graph), of the two circularly polarized components of the probe field after it has passed through a QWP rotated by an angle θ. Note that the black "LHC" and the red "RHC" traces correspond to the left- and right- hand-circular polarization components, respectively.

II.3.C Dark-state analysis

Let the dipole moments between |1> and |3> be μ_{13} and |2> and |3> be μ_{23}, and $\mu_{13}= \mu_{23} = \mu_0$. Then, the Rabi frequencies become $\Omega^+ = -\frac{\mu_0 \boldsymbol{E}^+}{\hbar} = \Omega_p(cos\theta + sin\theta)e^{i\theta}$ and $\Omega^- = -\frac{\mu_0 \boldsymbol{E}^-}{\hbar} = \Omega_p(cos\theta - sin\theta)e^{-i\theta}$, where $\Omega_p = -\frac{\mu_0 E_0}{\hbar\sqrt{2}}$. Electric dipole transition between the states |3> and |4> is coupled by a linearly-polarized coupling beam with frequency ω_c and Rabi frequency $\Omega_c = -\frac{\mu_{34}.E_c}{\hbar}$, where μ_{34} is the dipole moment between |3> and |4> and $E_c = \sqrt{\frac{I_c}{2n\varepsilon_0 c}}$ is the electric field strength of the coupling beam with intensity I_c. The frequency detunings are $\Delta_p = \omega_p - \omega_{31} = \omega_p - \omega_{32}$ and $\Delta_c = \omega_c - \omega_{43}$, where $\omega_{31=}\frac{E_3-E_1}{\hbar}$, $\omega_{32=}\frac{E_3-E_2}{\hbar}$ and $\omega_{43=}\frac{E_4-E_3}{\hbar}$ are the transition frequencies between the energy levels |3> and |1>, |3> and |2> ,and |4> and |3>, respectively. We also assume that the coupling beam is much stronger than the probe beam, i.e. $\Omega_p << \Omega_c$.

Had our system consisted of only the levels |1>, |3> and |4> and the beams Ω^+ and Ω_c with $\Omega_c >> \Omega^+$, then we would have expected to observe the usual EIT behavior associated with a ladder-type system[17] with vanishing absorption at the two-photon resonant condition of $\Delta_p + \Delta_c = 0$. We are now interested in understanding how the beam Ω^- that has a controllable phase difference of $\varphi = 2\theta$ with respect to Ω^+ will modify the EIT profile. When $\theta = 0$, we have $\varphi = 0$ and $\boldsymbol{E}^+ = \boldsymbol{E}^-$, i.e. the probe beam is linearly polarized. When $\theta = \frac{\pi}{4}$ we have $\boldsymbol{E}^-= 0$, i.e., the probe beam is RHC polarized. Here, we expect optical pumping to populate the |2> level, so $\Omega^+$and Ω_c lead to no EIT phenomenon. When $0 < \theta < \frac{\pi}{4}$, we have $0 < \varphi < \frac{\pi}{2}$ and when $\frac{\pi}{4} < \theta < \frac{\pi}{2}$, we have $\frac{\pi}{2} < \varphi < \pi$. We will specifically look for quantum interference phenomena that might switch from constructive to destructive while crossing $\varphi = \frac{\pi}{2}$. As an example, we will

consider the pair of phases $\varphi = \frac{\pi}{2} + \frac{\pi}{6}$ and $\frac{\pi}{2} - \frac{\pi}{6}$. We also note that in these two cases, the probe beam's intensity distribution among its $\hat{\boldsymbol{\sigma}}^{+}$and $\hat{\boldsymbol{\sigma}}^{-}$components are the same (which correspond to QWP rotations of $\theta = \frac{\pi}{3}$ and $\frac{\pi}{6}$). The only difference between the two cases is then the phase between the two probe beam components.

The Hamiltonian of the system shown in Fig. 1 can be written as the matrix

$$\mathrm{H} = -\hbar \begin{pmatrix} 0 & 0 & \left(\frac{\Omega^{+}}{2}\right)^{*} & 0 \\ 0 & 0 & \left(\frac{\Omega^{-}}{2}\right)^{*} & 0 \\ \frac{\Omega^{+}}{2} & \frac{\Omega^{-}}{2} & \Delta_p & \left(\frac{\Omega_c}{2}\right)^{*} \\ 0 & 0 & \frac{\Omega_c}{2} & \Delta_p + \Delta_c \end{pmatrix} . \qquad (1)$$

Under the resonant conditions of $\Delta_p + \Delta_c = 0$ and $\Delta_p = 0$, we identify three dark states, or non-coupled states, that are decoupled from the state |3>:

$$|NC1> = \frac{\Omega_c}{\sqrt{|\Omega^{+}|^2+|\Omega_c|^2}}|1> - \frac{\Omega^{+}}{\sqrt{|\Omega^{+}|^2+|\Omega_c|^2}}|4> \cong |1> - \frac{\Omega^{+}}{\Omega_c}|4>, \qquad (2a)$$

$$|NC2> = \frac{\Omega_c}{\sqrt{|\Omega^{-}|^2+|\Omega_c|^2}}|2> - \frac{\Omega^{-}}{\sqrt{|\Omega^{-}|^2+|\Omega_c|^2}}|4> \cong |2> - \frac{\Omega^{-}}{\Omega_c}|4>, \qquad (2b)$$

$$|NC3> = \frac{\Omega^{-}}{\sqrt{|\Omega^{+}|^2+|\Omega^{-}|^2}}|1> - \frac{\Omega^{+}}{\sqrt{|\Omega^{+}|^2+|\Omega^{-}|^2}}|2> = \frac{\Omega^{-}}{\Omega_p}|1> - \frac{\Omega^{+}}{\Omega_p}|2>. \qquad (2c)$$

In Eq. 2a and Eq. 2b, we have kept terms only to the first order in $\frac{\Omega_p}{\Omega_c}$. Quantum mechanically, two paths that result in the same end product will interfere. The total dark state amplitude is then given by

$$|NC> = |NC1> + |NC2> + |NC3>,$$

$$\text{i.e., } |NC> = \left(1 + \frac{\Omega^-}{\Omega_p}\right)|1> + \ (1 - \frac{\Omega^+}{\Omega_p})|2> \ - \frac{1}{\Omega_c}(\Omega^+ + \Omega^-)|4>. \qquad (3)$$

We want to see how the populations of the atoms in the dark states will vary as the three non-coupled states interfere with each other. That is, we would like to find $|\langle NC(\theta, \varphi)|\psi\rangle|^2$, where

$$|\psi> = c_1|1> + c_2|2> + c_3|3> + c_4|4> \qquad (4)$$

is the wavefunction of the atom in its bare-state basis. From Eq.3 and Eq.4, we get

$$|\langle NC(\theta, \varphi)|\psi\rangle|^2 = \left|1 + \frac{\Omega^-}{\Omega_p}\right|^2 \rho_{11} + \left|1 - \frac{\Omega^+}{\Omega_p}\right|^2 \rho_{22} + \left|\frac{\Omega^+}{\Omega_c} + \frac{\Omega^-}{\Omega_c}\right|^2 \rho_{44}$$

$$+2Re\{\left(1 + \frac{\Omega^-}{\Omega_p}\right)\left(1 - \frac{\Omega^+}{\Omega_p}\right)^* \rho_{21} - \frac{1}{\Omega_c}(\Omega^+ + \Omega^-)^*[\left(1 + \frac{\Omega^-}{\Omega_p}\right)\rho_{41} + \left(1 - \frac{\Omega^+}{\Omega_p}\right)\rho_{42}]\} \quad (5)$$

where $\rho_{nm} = c_m{}^* c_n$ are the elements of the density-matrix operator $\hat{\rho}$.

To find the density-matrix elements, we use the equations of motion for ρ_{nm}, i.e.

$$\dot{\rho}_{nm} = \frac{-i}{\hbar}[\mathrm{H}, \rho]_{nm}, \qquad (6)$$

which yield the following equations:

$$\dot{\rho}_{21} = -\gamma_{21}\rho_{21} - \frac{i}{2}\Omega^{+}\rho_{23} + \frac{i}{2}(\Omega^{-})^{*}\rho_{31}, \tag{7a}$$

$$\dot{\rho}_{31} = -(\gamma_{31} - i\Delta p)\rho_{31} + \frac{i}{2}\Omega^{+}(\rho_{11} - \rho_{33}) + \frac{i}{2}\Omega^{-}\rho_{21} + \frac{i}{2}(\Omega_c)^{*}\rho_{41}, \tag{7b}$$

$$\dot{\rho}_{32} = -(\gamma_{32} - i\Delta p)\rho_{32} + \frac{i}{2}\Omega^{-}(\rho_{22} - \rho_{33}) + \frac{i}{2}\Omega^{+}\rho_{12} + \frac{i}{2}(\Omega_c)^{*}\rho_{42}, \tag{7c}$$

$$\dot{\rho}_{41} = -[\gamma_{41} - i(\Delta p + \Delta c)]\rho_{41} + \frac{i}{2}\Omega_c\rho_{31} - \frac{i}{2}\Omega^{+}\rho_{43}, \tag{7d}$$

$$\dot{\rho}_{42} = -[\gamma_{42} - i(\Delta p + \Delta c)]\rho_{42} + \frac{i}{2}\Omega_c\rho_{32} - \frac{i}{2}\Omega^{-}\rho_{43}, \tag{7e}$$

$$\dot{\rho}_{43} = -(\gamma_{43} - i\Delta c)\rho_{43} + \frac{i}{2}\Omega_c(\rho_{33} - \rho_{44}) - \frac{i}{2}(\Omega^{+})^{*}\rho_{41} - \frac{i}{2}(\Omega^{-})^{*}\rho_{42}. \tag{7f}$$

In Eq.7, we have also introduced the decay rates γ_{ij} between the levels $|i>$ and $|j>$. Neglecting collisional broadening, we have $\gamma_{ij} = \frac{1}{2}(\Gamma_i + \Gamma_j)$, where Γ_i is the natural decay rate of the level $|i>$.

In the steady state when $\dot{\rho}_{nm} = 0$, we make the assumptions $\rho_{33} = \rho_{44} = 0$ under the weak probe field approximation[17], which means $\rho_{11} + \rho_{22} = 1$. This assumption is valid since in the limit $\Omega_c \gg \Omega_p$, most of the atoms are populated in the ground state levels[12]. Furthermore, we use $\rho_{11} = \frac{1}{2}(\cos\theta - \sin\theta)^2$ and $\rho_{22} = \frac{1}{2}(\cos\theta + \sin\theta)^2$. To justify these population distributions, we can consider two cases. First, when $\theta = 0$, the probe beam is linearly polarized and its intensity is equally distributed amongst its $\hat{\boldsymbol{\sigma}}^{+}$and $\hat{\boldsymbol{\sigma}}^{-}$components. When the coupling fields are absent, we expect the two ground state levels to be equally populated, i.e. $\rho_{11} = \rho_{22} = \frac{1}{2}$. This population distribution would then be maintained when the probe beam is linearly polarized. Second, when the QWP is set to $\theta = \frac{\pi}{4}$, the probe beam is $\hat{\boldsymbol{\sigma}}^{+}$polarized. In this case, due to the optical pumping effect, $\rho_{11} = 0$ and $\rho_{22} = 1$. For other values of θ, $\rho_{11}$and ρ_{22}depend

on the relative intensities of the $\hat{\boldsymbol{\sigma}}^{+}$and $\hat{\boldsymbol{\sigma}}^{-}$ components of the probe beam. Taking $\Omega_p << \Omega_c$, we then have

$$\rho_{31} = \frac{\Omega^{+}}{2i[-(\gamma_{31}-i\Delta p)-\frac{|\Omega_c|^2}{4\{\gamma_{41}-i(\Delta p+\Delta c)\}}}.[\frac{1}{2}(\cos\theta-\sin\theta)^2], \tag{8a}$$

$$\rho_{32} = \frac{\Omega^{-}}{2i[-(\gamma_{32}-i\Delta p)-\frac{|\Omega_c|^2}{4\{\gamma_{42}-i(\Delta p+\Delta c)\}}}.[\frac{1}{2}(\cos\theta+\sin\theta)^2], \tag{8b}$$

$$\rho_{21} = \frac{i}{2\gamma_{21}}\{(\Omega^{-})^{*}\rho_{31}-\Omega^{+}\rho_{32}{}^{*}\}, \tag{8c}$$

$$\rho_{41} = \frac{i\Omega_c}{2(\gamma_{41}-i(\Delta p+\Delta c))}\rho_{31}, \tag{8d}$$

$$\rho_{42} = \frac{i\Omega_c}{2(\gamma_{42}-i(\Delta p+\Delta c))}\rho_{32}, \tag{8e}$$

$$\rho_{43} \cong 0. \tag{8f}$$

II.3.D. Theoretical results

We are now ready to evaluate $|\langle NC(\theta,\varphi)|\psi\rangle|^2$, i.e. the populations of the atoms in the dark states . As mentioned earlier, two special phases, $\varphi = \frac{\pi}{2}+\frac{\pi}{6}$ and $\frac{\pi}{2}-\frac{\pi}{6}$, will be considered. Figure 3 shows the dark-state population (DSP) for these two states of the probe beam

polarizations as a function of the probe beam's frequency detuning. The DSP for the case of the linearly-polarized probe beam, i.e. $\varphi = 0$, is also shown in the figure for reference. For all the theoretical figures, we have used the following values for the parameters in Eq. 5 and Eq. 8:

$\Omega_p = 0.8{\times}2\pi\ MHz, \Omega_c = 10{\times}2\pi\ MHz, \gamma_{31} = \gamma_{32} = 6{\times}2\pi\ MHz,$

$\gamma_{41} = \gamma_{42} = 1{\times}2\pi\ MHz, \gamma_{21} = 0.05{\times}2\pi\ MHz$, and $\Delta c = 0$.

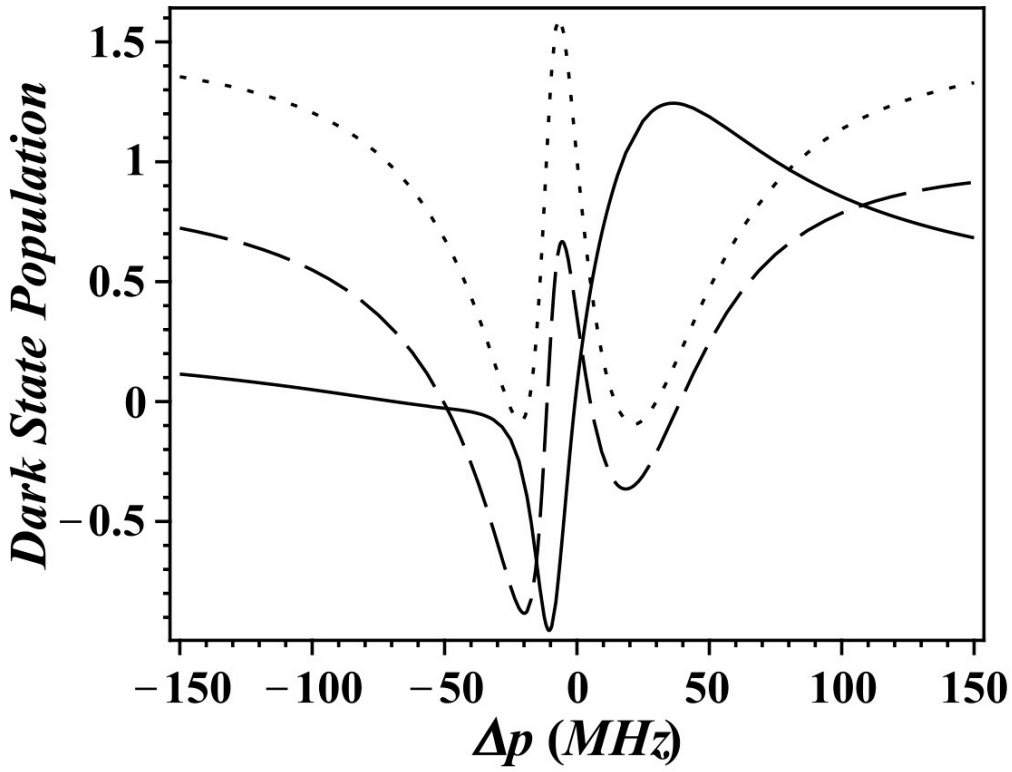

Fig. 3. Variations of the dark-state population over probe beam detuning, corresponding to three different phases (dotted: $= 0$; dashed: $\varphi = \frac{\pi}{2} + \frac{\pi}{6}$; solid: $\varphi = \frac{\pi}{2} - \frac{\pi}{6}$). Negative values signify the transition of a dark state to an enhanced absorption state.

Since the dark states do not absorb the incident fields, the DSP profiles shown in Fig. 3 resemble the intensity profiles of the transmitted probe beam for the corresponding phases. In the figure, negative values of DSP signify a transition of a dark (EIT) state to an enhanced absorbing (EIA) state. We see that near $\Delta_p = 0$, the regular EIT peak corresponding to the linearly-polarized probe beam gets modulated as the phase is altered to $\frac{\pi}{2} + \frac{\pi}{6}$ or $\frac{\pi}{2} - \frac{\pi}{6}$. For the first phase, the overall DSP profile decreases. For the latter phase, the region becomes absorbing on one side of $\Delta_p = 0$ and transparent on the other side. We reiterate that in these two cases, the beam powers are identical. Depending on whether the phase is greater than or less than $\frac{\pi}{2}$, the interference between the various non-coupled states involved in the Hamiltonian (Eq. 1) changes from constructive to destructive. This behavior is characterized by the interference between the coherence terms ρ_{41}, ρ_{42} and ρ_{21} in Eq. 5. When this interference is destructive, a dark (EIT) region switches to a bright or enhanced absorbing (EIA) region.

In polarization-sensitive EIT experiments, the sub-Doppler EIT resonances corresponding to the hyperfine levels near the excited state |4> become increasingly resolvable[72,73,96]. Due to their proximity to one another, the modulation in one window affects that of the other. In order to describe the overall behavior of the atomic system, it is necessary to include the contributions due to each of these closely-lying hyperfine levels. In Fig. 4, we have included contributions due to three resonances arising from such excited-state hyperfine levels. We have also accounted for Doppler-broadening effects typical in such hot atomic systems[17].

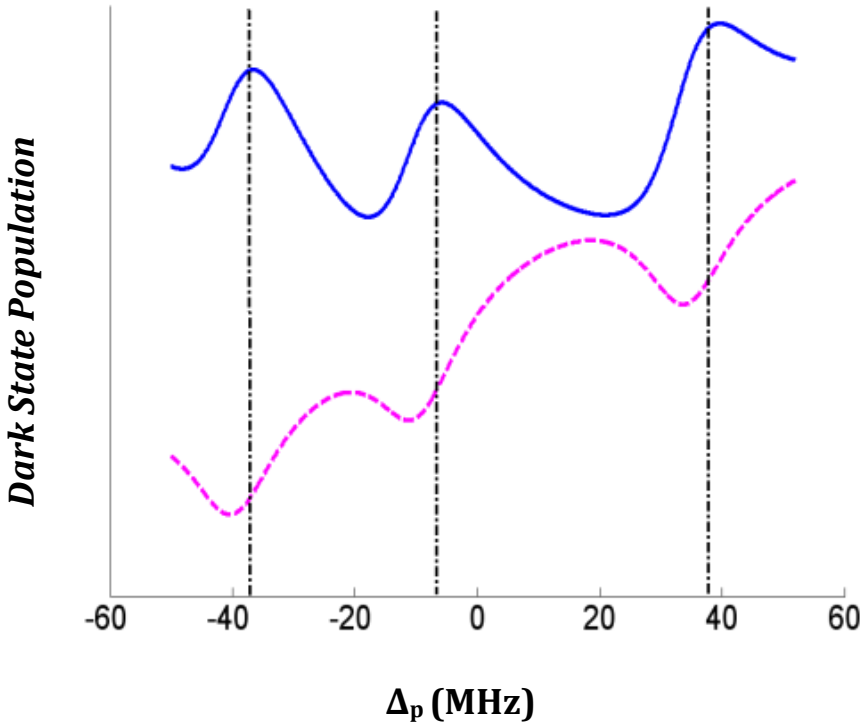

Fig. 4. Theoretical profiles of the dark-state populations when there are three closely lying hf levels in the upper excited state. The two traces are obtained for different phases between the probe beam components (dashed : $\varphi = \frac{\pi}{2} + \frac{\pi}{6}$; solid: $\varphi = \frac{\pi}{2} - \frac{\pi}{6}$).

II.4. Experimental observations

II.4.A. Experimental setup

The switching of multiple transparency windows due to phase-coupled dark states has been experimentally observed in hot ^{87}Rb atomic vapor. In Fig. 1(c), the two ground states |1> and |2> correspond to the degenerate Zeeman sublevels with magnetic quantum numbers $m_F = -1$ and $m_F = +1$, respectively, of the $5s_{1/2}$ F = 2 hyperfine level. The state |3> is the $m_{F'} = 0$ Zeeman sublevel of the $5p_{3/2}$ F' = 3 hyperfine level, while the state |4> is the $m_{F''} = 0$ Zeeman sublevel of the $5d_{3/2}$ F'' = 2 hyperfine level.

The experimental setup is shown in Fig. 5. A horizontally-polarized coupling beam with wavelength $\lambda_c = 776\, nm$ and power 40 mW is directed into a rubidium atomic vapor cell maintained at a temperature of 60 °C. The vapor cell is wrapped in a μ-metal shield to reduce the effect of magnetic fields due to the earth and the surrounding electronic equipment, in order to minimize the shifts of the Zeeman sublevels within each hyperfine level. There is a region inside the atomic vapor cell where a probe beam, which is scanned around the wavelength of $\lambda_p = 780\, nm$ and has a power of 7 mW, overlaps with the counter-propagating coupling beam at a small angle. Before entering the vapor cell, the probe beam passes through a half-wave plate (HWP) followed by a QWP. The HWP makes the probe beam vertically polarized. The QWP is rotated by an angle θ to control the polarization of the incoming vertically-polarized probe beam. After passing through the QWP, components of the probe beam in the $\hat{\boldsymbol{\sigma}}^+$ and $\hat{\boldsymbol{\sigma}}^-$ basis become $\mathbf{E}^+ = \frac{E_0}{\sqrt{2}}(cos\theta + sin\theta)e^{i\theta}$ and $\mathbf{E}^- = \frac{E_0}{\sqrt{2}}(cos\theta - sin\theta)e^{-i\theta}$, respectively. The transmitted probe beam is measured by detector D1.

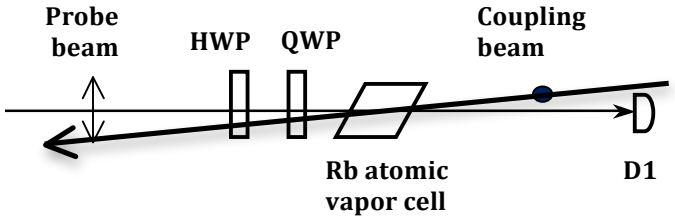

Fig. 5. Experimental setup. HWP: half-wave plate; QWP: quarter-wave plate. Coupling beam is horizontally polarized and the incident probe beam is vertically polarized.

II.4.B. Experimental results

The transmitted profile of the probe beam includes the usual Doppler-broadened D2 absorption lines for ^{87}Rb, corresponding to the lower transitions in Fig.1. Due to the strong counter-propagating coupling beam which drives the upper transition in Fig.1, we observe three sub-Doppler EIT regions within the broad absorption dip. These three EIT regions correspond to the F" = 3, 2 and 1 hyperfine levels of the $5D_{3/2}$ level[18,19]. As the QWP was rotated by an angle θ introducing a phase of φ = 2θ between the $\hat{\boldsymbol{\sigma}}^{+}$ and $\hat{\boldsymbol{\sigma}}^{-}$ components of the probe beam, we observed that the EIT regions display varying behaviors. These variations are shown in Fig. 6.

In the vicinity of the resonance $\Delta_p + \Delta_c = 0$, the EIT profiles shown in Fig. 6 corresponding to the phases $\varphi = \frac{\pi}{2} + \alpha_i$ and $\varphi = \frac{\pi}{2} - \alpha_i$, for $\alpha_1 = \frac{\pi}{3}$ and $\alpha_2 = \frac{\pi}{6}$, appear to be reflections about the absorption profile in that region when Ω_c=0. (The two profiles (a) and (g) are the same because in both cases, the probe beam is linearly polarized.) In the theoretical model, we expect a vanishing EIT behavior for a $\hat{\boldsymbol{\sigma}}^{+}$probe beam. The profile shown in Fig. 6 (d) shows some EIT behavior because when we consider all the Zeeman sublevels in the relevant

^{87}Rb hyperfine levels, there exists a transition that couples the optically-pumped ground state Zeeman sublevel (m_F= +2) due to the $\hat{\sigma}^+$probe beam to the excited states (via F' = 3, $m_{F'}$ = +3). The inverted-Y type system shown in Fig. 1 (c) is not intended to treat cascade-type branches that involve the magnetic sublevels $m_{F'} = \pm 3$ of the $5p_{3/2}$ level. These branches are the only ones that are active in the cases of circularly-polarized probe beams, and the phase-induced interference phenomena that we are treating are absent in this case.

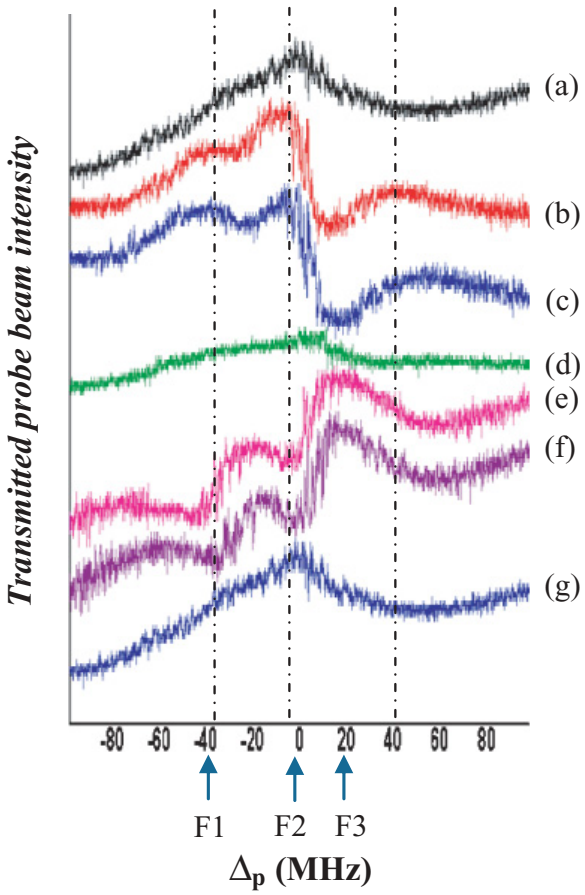

Fig. 6. Experimental observation of the dark-to-bright switching at three resonances (dashed lines) when φ is at (a) 0 ; (b) $\frac{\pi}{2} - \frac{\pi}{3}$; (c) $\frac{\pi}{2} - \frac{\pi}{6}$; (d) $\frac{\pi}{2}$; (e) $\frac{\pi}{2} + \frac{\pi}{6}$; (f) $\frac{\pi}{2} + \frac{\pi}{3}$; (g) π. Profiles have been shifted along the vertical axis for better visualization. F1, F2 and F3 denote positions for considering conditions of AND and OR operations.

While numerous hyperfine levels and Zeeman sublevels are involved in the actual experiment, we have qualitatively identified the cause of the dark-to-bright switching to be the interference between the non-coupled states in a four-level inverted-Y system. Our theoretical results for the dark state populations shown in Fig. 4 are in close agreement with the corresponding experimental observations for the probe beam transmission, i.e. the profiles Figs. 6 (c) and (e). Several inverted-Y subsystems exist in the actual atom-field Hamiltonian because the fields create electric dipole transitions from m_F = -2, -1, 0, 1, 2 of $5S_{1/2}$, F = 2 to $5P_{3/2}$, F'= 1, 2, 3 and $5D_{3/2}$, F" = 0, 1, 2, 3. Figure 1 shows only one of those subsystems, and its treatment seems to be sufficient to understand the qualitative behavior of the multiple dark states in such atomic systems. By applying the above model to all the occurring inverted-Y subsystems and adding the results together with appropriate weight factors (due to different Clebsch-Gordan coefficients) to get the total DSP distribution, we could further improve the relative heights of the three resonances.

In Fig. 6, we see that for a given phase, the atomic medium can be transparent ("on") or enhanced-absorbing ("off") at various frequency bands. As the phase is varied, the behaviors at these bands switch simultaneously. This allows for the possibility of handling switching conditions such as AND and OR that might find applications in optical communication and quantum computation. For instance, by switching between the systems shown in Figs. 6 (c) and (e), we could implement an AND type condition for signals at frequencies F1 and F2, or an OR type condition for signals at frequencies F1 and F3. The fact that all the field strengths and intensities remain identical during the switching process might also be of practical importance.

II.5. Conclusion

By using only two fields and an atomic medium, we have identified an adiabatic process that allows us to control the transparency of the medium at multiple frequencies simultaneously. We achieved this by altering a single parameter, i.e. the phase difference between the two circularly-polarized components of one of the fields. Such fields correspond to different elliptical polarization states, and are generated by using a quarter-wave plate. We explained the process by treating the quantum interference between multiple dark states, and our model agrees with the experimental observations. Even though a realistic atom comprises of thirty-six magnetic sub-levels, by using the dark-state analysis, we were able to explain the qualitative features by using a simple model comprising of four magnetic sub-levels. This demonstrated multiple dark/ bright state switching at various spectral positions could find applications in optical communication and quantum information processing.

III. FWM between the excited states of a ladder-type system

III.1. Introduction

In the previous chapter, we discussed EIT in a ladder-type configuration comprising of the 5S, 5P and 5D states. In this chapter, we will discuss the generation of resonantly enhanced FWM radiation between the hyperfine structures of the 5D and 5P states in the ladder-type atomic configuration. In contrast to previous FWM studies where the FWM radiation is generated between the first excited state and the ground state, the radiation presented here is between two excited states and several new properties are observed. The spectral-domain properties of the radiation are characterized, and the underlying mechanisms discussed.

First, we will give a very general description of FWM processes enhanced by atomic coherence and EIT, and discuss the motivations and advantages of this enhancement method. We will describe some systems that are popular in the literature. This discussion will give this thesis a measure of self-sufficiency, since all subsequent chapters will utilize EIT-enhanced MWM processes. Second, we will focus on the specific atomic system that is being studied in this particular experiment. Here, we will present the experimentally observed spectra, and qualitatively discuss the underlying mechanisms responsible for the observed effects. We will discuss why multi-photon transitions in this atomic system reveal more complex spectral features compared to traditional FWM studies between a ground state and an excited state. Finally, we will end the chapter with some concluding remarks.

III.2. General overview of FWM enhancement using atomic coherence and EIT

Traditionally, nonlinear optical phenomena were observed at large optical intensities. In fact, the term "nonlinear" in nonlinear optics describes the dependence of such phenomena on terms vary polynomially in the electric field of the radiation. Large optical intensities were required because the higher order terms of the material medium's susceptibilities are typically orders of magnitude weaker than the lower-order terms. Moreover, when driving the higher order terms of the nonlinear polarization, the lower orders are also driven, in particular the first order term that gives rise to absorption. To drive the weak nonlinearities while at the same time overcome these absorptive losses, fields with very high intensities were used, typically short pulses. The absorptive losses thus give rise to inefficiencies in the process of searching for nonlinear effects. Furthermore, the large intensity gives rise to power-broadening effects. High-intensity pulses, which are temporally short and spectrally broad, can also drive many spurious transitions. All of these features can give rise to large background scattering noises. In summary, nonlinear optical processes relying on large driving beam powers can be inefficient as well as have bad signal-to-noise ratios. In order to minimize absorptive losses, many studies also use off-resonance driving beams; but nonlinearities also become weaker away from resonance, thus further raising the demands on the intensity of the optical field driving the process. Nonetheless, these methods are still of great importance in phenomena that utilize intense pulses, such as in solitons and pulse transmission in fibers.

The use of atomic coherence in multi-level atoms to drive nonlinear optical processes circumvents the aforementioned drawbacks. First, EIT, which is a two-photon coherent phenomenon arising in three-level atomic systems, annihilates absorption even at resonance. The lack of absorptive losses at resonance has several consequences. First, a lower driving beam

intensity is now required to overcome the threshold for nonlinear gain since absorption is not depleting the input. Second, the nonlinear transitions can be driven resonantly without absorptive losses and scattering noise, thus allowing for the maximum possible efficiency of generation as well as good signal-to-noise (SNR) ratio. Third, at EIT, not only is the resonant medium transparent to the driving beam but also transparent to the nonlinearly generated signal fields, thus enhancing efficiency and SNR. Fourth, since now weak fields can be used to drive the atomic coherences, cw beams with small intensities and very narrow spectral bandwidths can be used. These beams cause minimal power-broadening, and do not drive unwanted atomic transitions at other frequencies. Finally, resonantly driven atomic coherences have amplitudes that are much larger than the off-resonant amplitudes, and are very effective source terms in Maxwell's equation giving rise to bright coherent signal radiations. These atomic coherences can be controlled with great precision. The coherence of these nonlinearly generated signals, in particular their phase control, will be a feature discussed in great detail in the subsequent chapters.

In the FWM experiments discussed in the thesis, including in this chapter, a three-photon resonance drives atomic coherence in Rb vapor, which then acts as a source of radiation of the fourth field in "completing" the FWM process/ transition. The parameters of the fourth field are constrained by the conservation of energy, momentum and angular momentum in the FWM process and can thus be precisely controlled by tuning the parameters of the three driving beams. The trick then is to embed, within the three-photon driven resonance, an EIT transition, thereby allowing the FWM process to be resonantly driven by weak (typically a few milliwatts) driving beams.

Resonantly enhanced multi-wave mixing processes have been investigated in many multi-level atomic configurations. In each configuration, different beam geometries and phase-matching conditions have been identified in order to utilize Doppler-free EIT resonances even in the presence of high-density atomic vapors having Doppler broadening; consequently, these atomic coherence enhanced FWM radiations can also have Doppler-free narrow spectral linewidths, in addition to a very narrow spatial bandwidth (unidirectionality). Typically, the FWM radiations have been generated between the ground state of the atom and the first excited state. One of the most popularly studied processes has been the generation of Stokes and anti-Stokes signals in a double-lambda atomic configuration. Here, a strong coupling beam and a weak probe beam form a lambda-type EIT configuration, driving a strong atomic coherence between the two ground state hyperfine levels. The difference frequency of these two beams matches the spectral separation of these two energy levels. A third driving beam, which could be an additional beam or the same coupling beam used twice, then couples one of the ground states to another excited state, which can be real or virtual. This third field mixes with the spin coherence between the ground states, and generates a Stokes or anti-Stokes field, depending upon whether it's frequency is smaller or larger than the driving field. In this process, this fourth field is amplified from an initially vacuum mode, and the weak probe beam in the initial EIT configuration is also amplified. Classical correlations as well as quantum correlations and entanglement have been verified between the noise fluctuations of these two amplified signals.

FWM process has been investigated in the ladder-type configuration too. In this case, the two-photon EIT resonance is driven at the sum-frequency of the probe and coupling beams, and the atomic coherence is driven between the 5S and the 5D states, with the 5P level serving as the intermediate level. When a third beam driving the transition between 5D and 5P is then impinged

upon the two-photon spin excitation, the resulting mixing radiates the FWM signal between the 5P and 5S states. FWM between the ground state and first excited state of the ladder-type configuration has been investigated, as well as in relation to other coexisting MWM processes in which the ladder-type system is a sub-system of a larger system such as the inverted-Y or Y-type systems.

III.3. Overview of the current experiment

In the aforementioned studies, the FWM signals were generated at the transition frequency between the 5P and the 5S states of Rb. In this current chapter, we describe a study in which FWM radiation is generated at the transition between the 5D and 5P excited states (Fig. 1a), and study it in the frequency domain. Atomic coherence and EIT mechanism are implemented, allowing the amplification to occur using low-power CW beams. We have investigated the spectral response of the generated waveform to the various contributing parameters, such as the spectroscopic properties (and multi-level structures) of the atomic energy levels, the vicinity of the laser frequencies to the various atomic resonances, and the powers of the driving beams. We consider their contributions to the properties of the generated radiations (such as the efficiency, line shape and linewidth) and discuss the optimum conditions suitable for this process. The generated radiation, containing high-resolution narrow-linewidth spectroscopic information, is background-free. These features can make this process desirable over other spectroscopic methods relying on two-photon fluorescence where the signals are typically very weak since the photons are scattered in all spatial directions and in any given detection direction, the background noise can be of comparable intensity with the signal. An energy level configuration similar to the current work was studied in the time domain in Ref. 106. Analytical solutions to

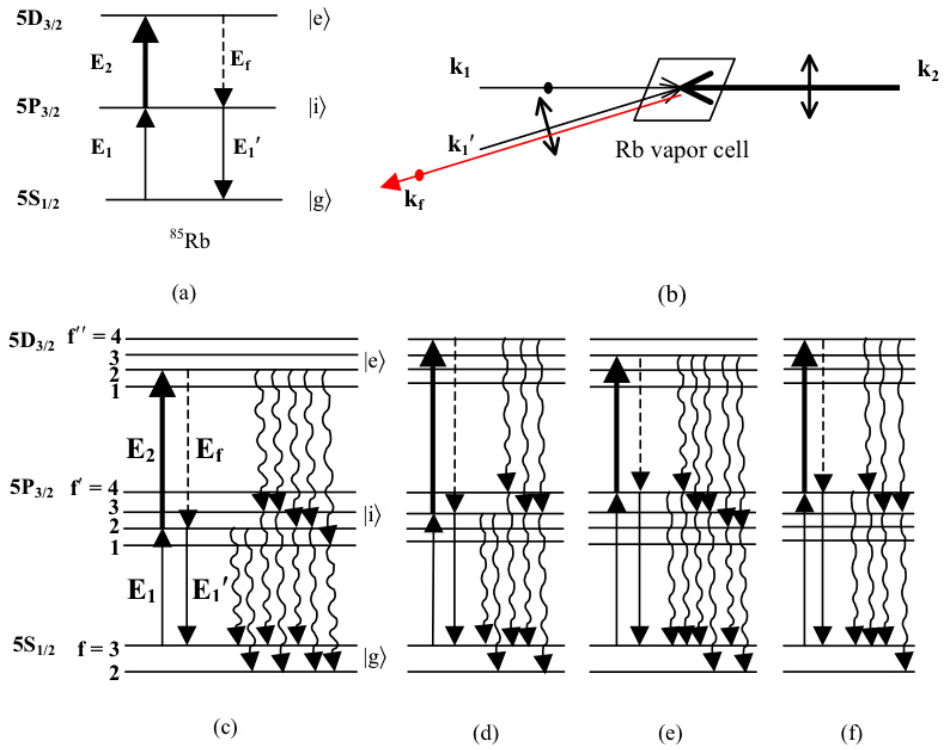

Fig. 1. (a) Simplified three-level ladder-type configuration in ^{85}Rb that is coherently driven in the FWM process; |g>, |i> and |e> stand for the ground, intermediate and excited states, respectively. $\mathbf{E_1}$, $\mathbf{E_1'}$ and $\mathbf{E_2}$ are external driving beams from laser sources, while $\mathbf{E_f}$ is the atom-radiated FWM signal that is parametrically amplified from the vacuum mode. (b) Schematic of the experimental configuration showing the directions and polarizations of the four fields. (c)-(f) Realistic energy level diagram showing the hyperfine (hf) levels of each driven state, as well as the incoherent decay channels (wavy arrows) between various combinations of driven hf levels: [f, f′, f′′] = (c) [3, 2, 2], (d) [3, 3, 4], (e) [3, 4, 3], and (f) [3, 4, 4]. The single-resonance decay channels are drawn first, followed by the double-resonance decay channels. The number of

single-resonance and double-resonance optical pumping channels is different in the various cases. The spacings between the energy levels are not drawn to scale.

the system were derived in Ref. [107] with approximations such as very weak driving beams and small hyperfine coupling, both of which are different from our current experimental conditions.

In Fig. 1a, we have only shown the closed three-level atomic system consisting of the fine structures being driven by the laser beams. In reality, each of these structures consists of a myriad of hyperfine (hf) levels due to coupling with the nuclear magnetic moment, most of which can radiatively decay to energy levels not being driven in the FWM process, making this a mixed system (i.e. consisting of closed as well as open sub-systems.) How open a driven sub-system is depends on the selection rules for the associated hf levels. The hf levels f, f′ and f′′ of the ground, intermediate and excited states, respectively, as well as the various decay channels associated with four different three-level subsystems, are shown in Fig. 1 (c-f). In each diagram, the decay channels of the single-photon transition are drawn first, followed by the decay channels due to the two-photon process. From these examples, it can be seen that some FWM subsystems have more decay channels than the others, and that various channels exist via which the atomic population gets optically pumped into the undriven ground state f = 2. The single-photon transition f = 3 → f′ = 4 is closed, whereas f = 3 → f′= 2, 3 can also radiatively decay to f = 2. A peculiar feature of the ladder-type configuration consisting of multiple sublevels is the so-called double resonance optical pumping (DROP) effect[108]. Beacause of DROP, even when the single-photon transition is closed, the two-photon process opens various optical pumping channels as shown in Fig. 1 (e-f). The 5D state also has decay channels via the 6P state, which are not shown in Fig. 1.

Furthermore, due to the close proximity of the hf energies in the 5D and 5P states, many subsystems are simultaneously resonant for a given pair of driving beam frequencies. The hf levels further consist of varying numbers of Zeeman sublevels with different transition strengths. As will be shown below, the multi-level nature as well as the fact that most of the driven subsystems can radiatively decay and lose population to the environment have important consequences to the Fourier-domain waveforms of the atom-radiated coherent FWM signal including the line shape and efficiency at various spectral positions, giving rise to a rich array of spectra. Accurately reproducing the line shapes analytically or numerically thus involves the bookkeeping of all the subsystem parameters, and is beyond the scope of this current experimental work. The intention of this current work is to illuminate the experimentally observed properties of this interesting FWM system and to qualitatively assess the underlying causes of the most important features.

III.4. Experimental method

The energy level configuration and the experimental geometry are shown in Fig. 1. The probe beam $\mathbf{E_1}$ (frequency ω_1, wavelength λ_1, wave vector $\mathbf{k_1}$) is generated by a CW diode laser DL. The wavelength λ_1 is scanned around 780 nm in order to probe the Doppler-broadened spectral bandwidth of the ^{85}Rb isotope's D_2 transition. The vapor cell is 5 cm long, and is magnetically shielded and heated to 60^{o} C. The transmitted probe beam intensity is monitored by a photodiode PD. A strong beam $\mathbf{E_2}$ (frequency ω_2, wavelength λ_2, wave vector $\mathbf{k_2}$) from a CW Ti-Sapphire laser is aligned to counterpropagate with $\mathbf{E_1}$. The wavelength of $\mathbf{E_2}$ is fixed but can be tuned around 776.158 nm, the wavelength of the upper transition in the cascade scheme. When both

one-photon resonance and two-photon resonance (TPR) are satisfied, the coupling beam renders the atomic medium transparent for the probe beam by virtue of EIT. Even though the D_2 absorption line is Doppler broadened in the hot atomic medium, the two-beam counterpropagating geometry allows the two-photon EIT process to be basically Doppler-free for the cascade configuration[17]. When the probe beam's frequency detuning is larger than the Doppler-broadened linewidth of the D2 transition, the single photon absorption is vanishingly small. Here, when the strong coupling beam is present satisfying TPR, we no longer have EIT. Instead, a direct two-photon transition is driven between |g> and |e> resulting in a two-photon absorption (TPA) peak. This Doppler-free TPA resonance has a much narrower linewidth than the Doppler-broadened D2 line's absorption linewidth, and the TPA depth can be tuned via the coupling beam's intensity. For intermediate frequency detunings lying between the EIT and TPA regimes, both stepwise (via |i>) and direct transitions from |g> to |e> are driven. At these frequency detunings, we observe a convolution of EIT and TPA in the transmission of the probe beam. The analytical solution showing the evolution of the TPR from EIT to TPA as the intermediate frequency detuning is increased can be found in Ref. 17.

The output of the diode laser DL is split to create a third beam $\mathbf{E_1}'$ (frequency ω_1, wavelength λ_1, wave vector $\mathbf{k_1}'$) that intersects with $\mathbf{E_1}$ and $\mathbf{E_2}$ inside the vapor cell at a small angle of θ (typically 0.4^o) with $\mathbf{k_1}$. The polarizations and powers of the beams can be altered independently. The third-order nonlinearity of the atomic medium, made efficient by the induced resonant coherences, leads to the generation of a new FWM radiation $\mathbf{E_f} \propto \chi^{(3)}\mathbf{E_1}'\mathbf{E_2}\mathbf{E_1}$ which counterpropagates with $\mathbf{E_1}'$ (due to conservation of linear momentum satisfying $\mathbf{k_f} = \mathbf{k_2} + \mathbf{k_1} - \mathbf{k_1}'$) but has the frequency of $\mathbf{E_2}$ (due to conservation of energy satisfying $\omega_f = \omega_2 + \omega_1 - \omega_1'$). In the EIT regime, the FWM process is enhanced because the transitions can be driven near the

atomic resonances, while dissipation from |i> as well as |e> are vanishingly small. This allows the $\chi^{(3)}$ nonlinear optical process to be driven and measured at low intensities. In the TPA regime, the dissipation from |i> is small due to the large intermediate frequency detuning. Here, when only $\mathbf{E_1}$ and $\mathbf{E_2}$ are present but $\mathbf{E_1'}$ is absent, the TPR coherence between |g> and |e> radiatively decays causing incoherent fluorescence scattering. The presence of $\mathbf{E_1'}$ stimulates coherent FWM radiation in the phase-matched direction. As will be shown below, the spectral linewidth of the FWM radiation is similar to the TPA linewidth, governed basically by the linewidth of the |e> state.

By appropriate choices of the polarizations of the driving beams, the polarization of the FWM signal $\mathbf{E_f}$ is made to be orthogonal to that of $\mathbf{E_1'}$. This allows for an effective isolation of the weak signal $\mathbf{E_f}$ using a polarization beam splitter, and is monitored with an avalanche photodiode APD. The voltage measurements of PD and APD are monitored simultaneously using a multi-channel oscilloscope, along with a reference Fabry-Perot cavity signal used for frequency calibration of the scanned DL output.

III.5. Experimental observations and discussions

Figure 2 shows the line-shapes of the generated FWM signal at various frequency detunings of the intermediate resonance, Δ_1, where $\Delta_1 = \omega_1 - \omega_{ig}$, with ω_{ig} being the transition frequency between the ground state and the first excited state. The Doppler-broadened absorption profile of the probe beam is also shown in the figure for reference, and gives information about the spectral position of the intermediate resonance used in the two-photon and FWM processes. Here, the absorption and FWM signals correspond to the f = 3 ground state of the ^{85}Rb isotope. We note

that while the intermediate-state detuning is different in each signal, all of them are two-photon-resonant (TPR); that is, the signal occurs only when $\Delta_1 + \Delta_2 = 0$, where $\Delta_2 = \omega_2 - \omega_{ei}$ and ω_{ei} is the transition frequency between the two excited states in the cascade configuration. As a result, even though the absorption profile is Doppler-broadened for the heated atomic ensemble, the generated FWM radiation has a line-shape that is Doppler-free. For convenience, the cases $\Delta_1 < 0$, $\Delta_1 = 0$ and $\Delta_1 > 0$ will be referred to as "red-detuned", "zero-detuned" and "blue-detuned", respectively.

In obtaining the four signals shown in Fig. 2, the only experimental parameter being varied is the value of ω_2, which causes TPR to occur at different values of Δ_1 as ω_1 is being scanned. Except for their spectral positions, occurring at 500 MHz intervals, all the other experimental conditions, such as the vapor cell temperature (60 °C), beam powers (P_1 = 7.4 mW, P_1' = 11.6 mW and P_2 = 40 mW) and beam geometry ($\theta = 0.4°$), are identical. The importance of the intermediate frequency detuning is evident in the line shape, linewidth and efficiency of the FWM process. Far from intermediate state resonance, the signal has a narrow linewidth. As the condition $\Delta_1 = 0$ is approached, the signal's linewidth becomes broader and the line shape becomes significantly convoluted. In the region slightly red-detuned from center, the FWM signal intensity also sharply decreases, experiencing a local minima.

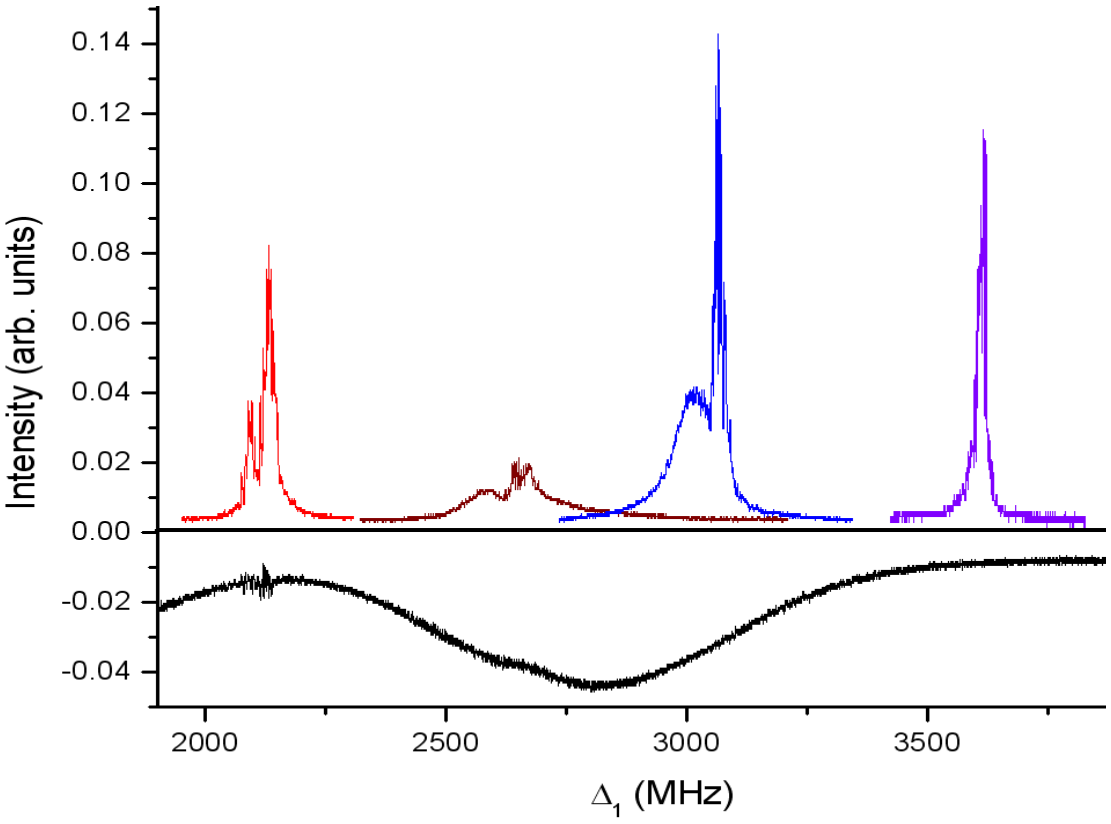

Fig.2. FWM signal line shape, linewidth and efficiency at four different intermediate frequency detunings, placed at intervals of 500 MHz. All other experimental parameters are constant in the four cases. The Doppler-broadened absorption linewidth of the corresponding ground state (hf = 3 of ^{85}Rb, $5S_{1/2}$) is also shown for reference.

FWM signals occurring at 100 MHz intervals are presented in Fig. 3a, showing the frequency-detuning dependent trends in more detail. All other experimental parameters are the same as those used in Fig. 2. At each spectral position, the signal is a convolution of a sharp "right" peak and a broad "left" peak. Each pair of dots connected by a line corresponds to the maximum intensities of the sharp and broad peaks occurring within a signal at a given detuning. Below, we will discuss the dependence of the FWM signal's (1) linewidth, (2) line shape and (3) efficiency upon the driving beam parameters as well as upon the internal structure of the atoms, and also (4) consider the dual role of the driving beam $\mathbf{E_1'}$.

III.5.A. Linewidth variations

Towards the center of the Doppler-broadened linewidth, as the condition $\Delta_1 = 0$ is approached, power-related effects, such as power broadening and AT splitting of the atomic energy levels, become dominant[15]. These effects are also revealed in the broadening and splitting of the FWM signal in the zero-detuned region. For large powers of $\mathbf{E_1}$ and $\mathbf{E_1'}$, when $\Delta_1 = 0$ is satisfied, the signal occurs at the AT-satellites[20] of the energy levels. There is a decrease in signal intensity in the spectral region occurring between the power-broadened AT satellites; that is, the signal maximum is displaced around $\Delta_1+\Delta_2 = 0$. When $|\Delta_1| >> 0$ as in the edges of the Doppler-broadened absorption linewidth and outside it, the EIT evolves into a two-photon-absorption (TPA)[17] having a narrow linewidth since power broadening is substantially reduced. Here the signal occurs within the linewidth of the TPA resonance and the signal maxima occurs at $\Delta_1+\Delta_2 = 0$. In particular, the power- broadening or splitting of the intermediate level is minimal in this two-photon resonant condition, and the linewidth of the FWM signal is mainly limited by the

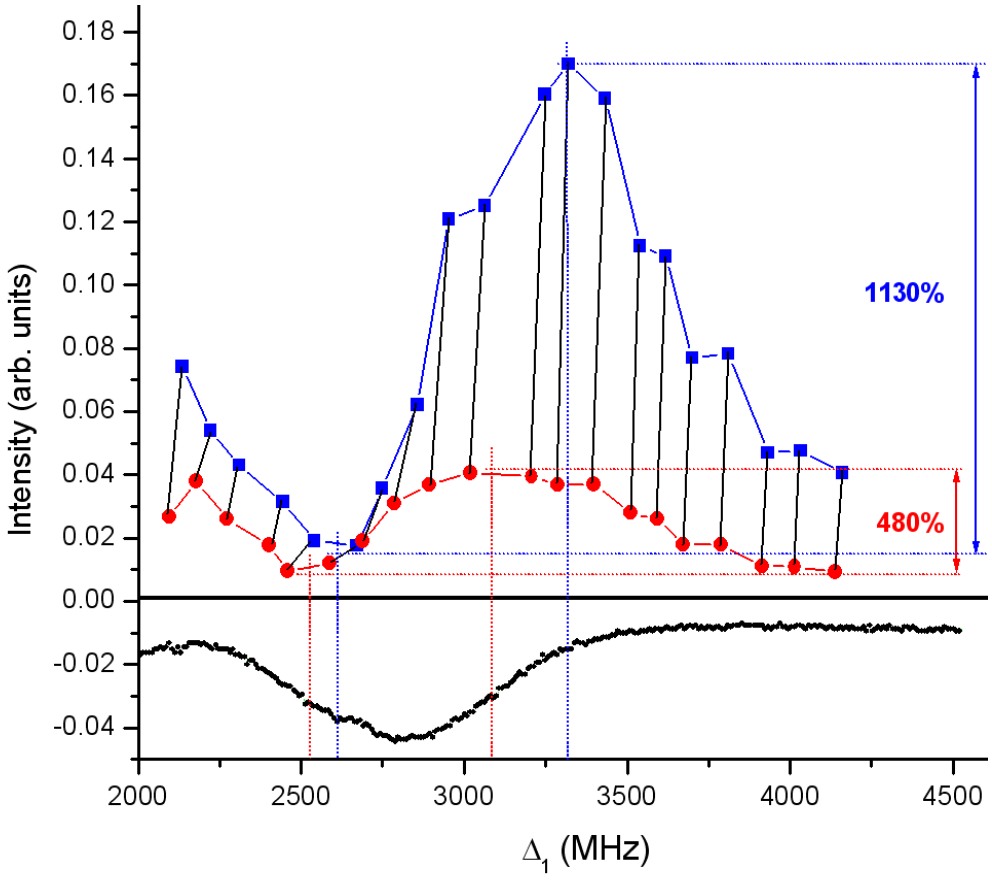
0.18
0.16
0.14
0.12
0.10
0.08
0.06
0.04
0.02
0.00
-0.02
-0.04
Intensity (arb. units)
2000
2500
3000
3500
4000
4500
Δ1 (MHz)
1130%
480%

(a)

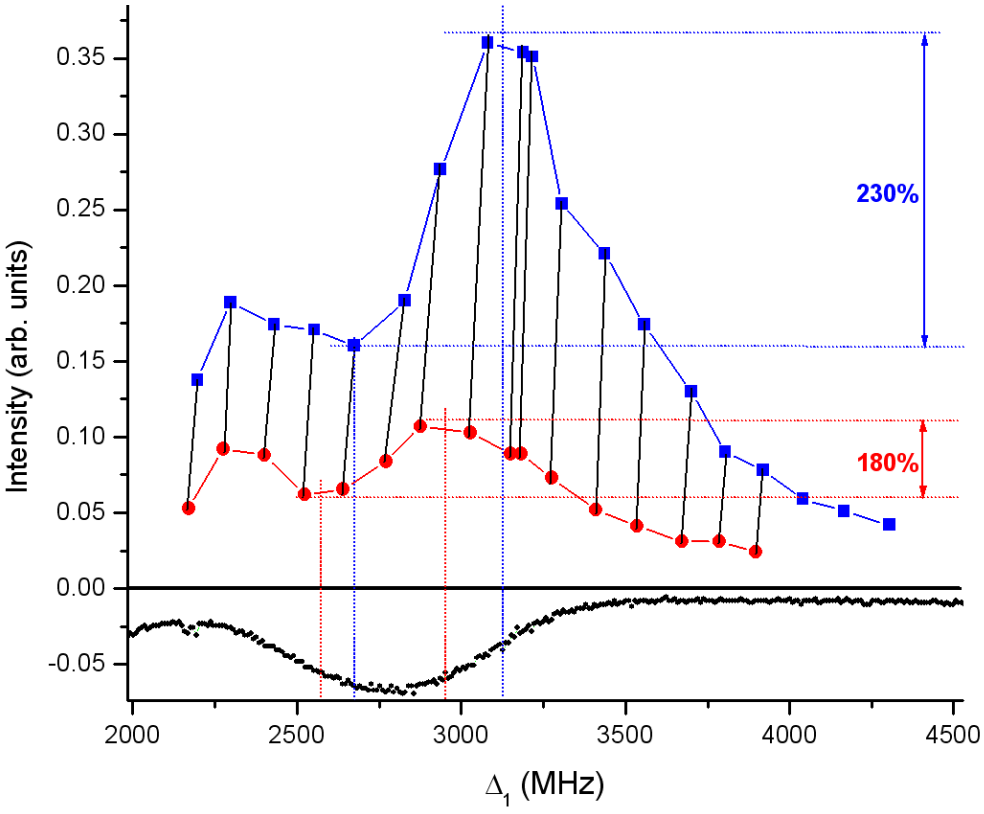

(b)

Fig. 3. TPR FWM signals corresponding to different values of Δ_1, separated by100 MHz each. The energy levels driven are $|g\rangle = 5S_{1/2,}$ hf =3, $|i\rangle = 5P_{3/2}$ and $|e\rangle = 5D_{3/2}$. At each value of the frequency detuning, the FWM signal is a convolution of a sharp, strong peak and a broad, weak peak, the maximum intensities of which are denoted by a blue square and a red dot, respectively. Each of the two signal peak trends are connected by lines to aid the eye. The two peak

values corresponding to a given convolution at a given frequency detuning are connected by a solid black line. The horizontal (vertical) dotted lines identify the intensities (intermediate frequency detunings) of the maximas and minimas of the signal convolution's two peaks. (a) P_1 = 7.4 mW, P_1' = 11.6 mW, P_2 = 38 mW (b) P_1 = 3 mW, P_1' = 4 mW, P_2 = 55 mW. Note the change of scale in the intensity axes.

linewidth of the upper-excited state. At intermediate detunings $|\Delta_1| > 0$, the probe beam experiences a convolution of EIT and TPA effects, and the generated FWM signal also displays the contributions due to these two mechanisms. Here, both direct two-photon transition from |g> to |e>, as well as stepwise transitions via |i> exist; the direct two-photon transition's linewidth is narrower as it depends on the relatively long-lived 5D state (natural linewidth 0.97 MHz), whereas the stepwise transition is broader because it also depends on the 5P state (natural linewidth 6 MHz).

III.5.B. Line shape asymmetries

In order to understand the asymmetries in the spectral line-shape of the generated FWM radiation, one needs to consider the multi-level structure of the atoms as shown in Fig. 1 (c-f). For different values of ω_2, different hf levels of the intermediate state are closest to satisfy TPR and contribute to the FWM process most effectively. The hf levels of the upper excited state are sufficiently close and lie within the power-broadened linewidth of the intermediate level, and all contribute to the TPR, whereas the intermediate state hf levels are further apart and dispersed

within the Doppler-broadened absorption window. The hf levels have varying multiplicities and disparate transition strengths; it is these spectroscopic characteristics of the atomic energy levels that contribute to the sharp asymmetries in the signal line-shape.

The TPR effects involving $f' = 4$ has the biggest contribution to the convoluted FWM line-shape, due to its large multiplicity and larger Clebsch-Gordon coefficients. More importantly, as shown in Fig. 1, the FWM pathways involving $f' = 4$ have the fewest decay channels. This is why the signal generation (Fig. 2 and Fig. 3) is strongest in the blue-detuned region of the Doppler width, as this is where the $f' = 4$ level lies. This is also why the sharp peak lies towards the right edge of each signal convolution for the chosen spin levels in this configuration. The effects of the branching ratios of the energy levels in the ladder-type system have been analyzed by Noh and Moon[109], showing signal convolutions due to the presence of closed and open subsystems.

To make these facts more evident, we have also generated signals by using other spin-levels having different constraints. First, in Fig. 4 (a-b), we change $|g\rangle$ to the other ground state hf level 2, while using the same $|i\rangle$ and $|e\rangle$ fine structures as used for Fig. 3. Here, we observe that the position of the sharp peak within the signal convolution occurs at the red-detuned side. Also, the position within the Doppler width where signal intensity is at a maximum, is in the red-detuned region. These changes occur because here, it is the transition $f = 2 \rightarrow f' = 1$ that is closed. Next, we use the same $|g\rangle$ and $|i\rangle$ as that used in Fig. 3, but change the upper excited state $|e\rangle$ to the other fine structure of 5D, i.e. $5D_{5/2}$ (Fig. 4 (c-d)). Here, similar to Fig. 3, the maximum signal intensity occurs in the blue-detuned region of the Doppler-width since the transition $f = 3 \rightarrow f' = 4$ is closed. However, in this case, the maximum peak within the signal convolution occurs in the red-detuned side. This change occurs because the energies of the hf levels in $5D_{5/2}$ are inverted;

that is, in this fine structure, the hf levels with higher values have lower energies[110]. This causes the contribution to the FWM signal from the higher f″ levels, which have allowed transitions from f′ = 4 of |i> as well as larger Zeeman multiplicities, to shift to the lower-energy side of the signal convolution. This is in contrast to Fig. 3, where |e> corresponded to $5D_{3/2}$ in which the hf levels are not inverted. The stronger FWM signal intensity observed when |e> is $5D_{5/2}$ may be attributed to it having fewer decay channels; while $5D_{3/2}$ can decay to both J = 3/2 and 1/2 of the 5P and 6P levels, the $5D_{5/2}$ fine structure can decay only to J = 3/2, due to selection rules. From Fig. 3 and 4, it is clear that the FWM efficiency is largest at frequency detunings where the single-resonance and double-resonance optical pumping effects are the weakest.

III.5.C. Variations in the FWM signal efficiency

At high beam powers for the lower transitions, saturation effects begin to occur, reducing the FWM efficiency. The associated power-broadening effects also contribute to the reduction of the maximum signal intensity. The minima in the signal intensity towards the red-detuned region deserves some attention. The decrease is the largest when the powers of $\mathbf{E_1}$ and $\mathbf{E_1'}$ are large. For instance, as shown in Fig. 3a for the conditions of P_1 = 7.4 mW, P_1' = 11.6 mW, P_2 = 38 mW, the percent decrease is 1030% (480%) for the strong (weak) peak of the FWM signal convolution. When the beam powers are changed to P_1 = 3 mW and P_1' = 4 mW, the percent decrease is only 230% (180%) for the strong (weak) peak (Fig. 3b). These values remained constant as P_2 was changed from 20 mW to 60 mW. We note that the hf levels 2 and 3 of the intermediate state lie in the red detuned region of the Doppler-broadened linewidth, as can be observed from saturation absorbtion spectroscopy. At high powers of $\mathbf{E_1}$ and $\mathbf{E_1'}$, these hf levels are power-

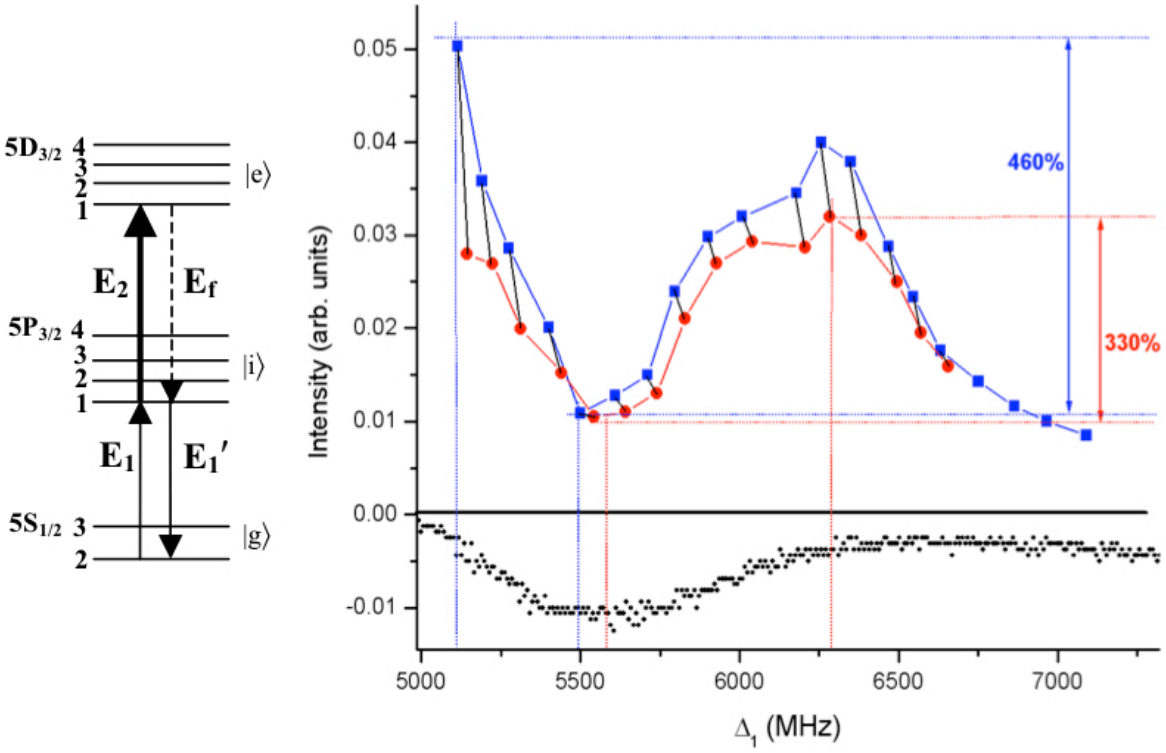
5D3/2 4
3
2
1
|e⟩
E2
Ef
5P3/2 4
3
2
1
|i⟩
E1
E1′
5S1/2 3
2
|g⟩
Intensity (arb. units)
0.05
0.04
0.03
0.02
0.01
0.00
-0.01
460%
330%
5000
5500
6000
6500
7000
Δ1 (MHz)

(a) **(b)**

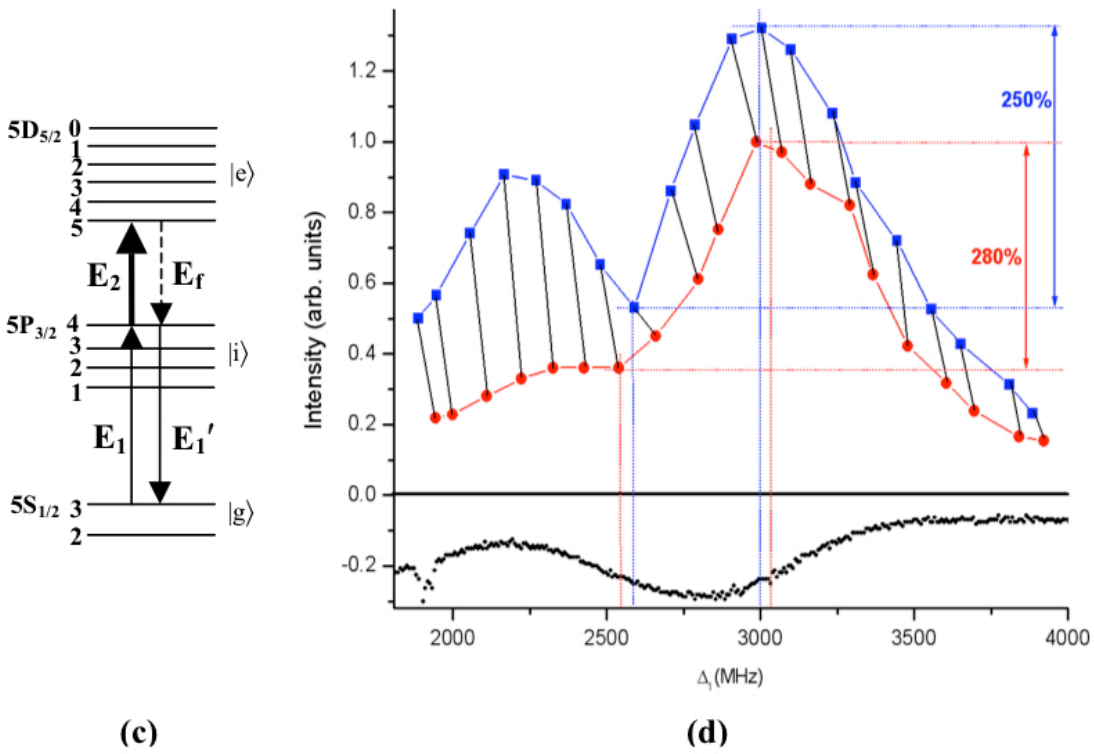

Fig. 4. (The meanings of the dots, squares and lines in (b) and (d) are the same as in Fig. 3.) The beam powers are P_1 = 7.4 mW, P_1' = 11.6 mW, P_2 = 38 mW. (a) and (b) The ground state used is hf = 2 of ^{85}Rb, $5S_{1/2}$, with |i> = $5P_{3/2}$ and |e> = $5D_{3/2}$. (c) and (d) The ground state hf = 3 of ^{85}Rb, $5S_{1/2}$ is used with |i> = $5P_{3/2}$, but with |e> = $5D_{5/2}$ and ω_2 = 775.978 nm, where the hf levels are inverted. Note the change of scale in the intensity axes. In (a) and (c), the FWM transitions with the least number of decay channels are shown.

broadened and there is a significant overlap between them. When Δ_1 lies in this overlapped region, the contributions of these hf levels to the total two-photon transition amplitude becomes comparable in strength but with opposite signs. The sign of the individual phases has contributions from the signs of the dispersions due to the opposite detunings. Such destructive interference due to multiple intermediate states[111-113] causes the total transition amplitude to decrease, suppressing the FWM efficiency. Moreover, in the high intensity regime of the ground-state coupling beams driving to f' = 2 or 3, the atomic population gets optically pumped out of the system to the f = 2 ground state as shown in Fig. 1 (c-d), leading to reduced signal generation.

III.5.D. Dual role of the driving beam $\mathbf{E_1'}$

Finally, we note the dual role of the coupling beam $\mathbf{E_1'}$ in this configuration. As a stimulant to the FWM process, it gains a photon whenever a photon is generated in the FWM signal, as shown in Fig. 1a. However, because it has access to the ground state population, $\mathbf{E_1'}$ also contributes to the depletion of the ground state population into incoherent channels, which becomes especially important at large beam powers. Also, because both $\mathbf{E_1}$ and $\mathbf{E_1'}$ have access to the ground state population, the coherences induced by these two beams between |g> and |i> are both significant. A mismatch between the strengths of these two coherences is detrimental to the FWM efficiency[43,46]. As a result, increasing P_1' indefinitely does not help the FWM efficiency. In fact, increasing the strength of the coherence due to $\mathbf{E_1'}$ beyond the

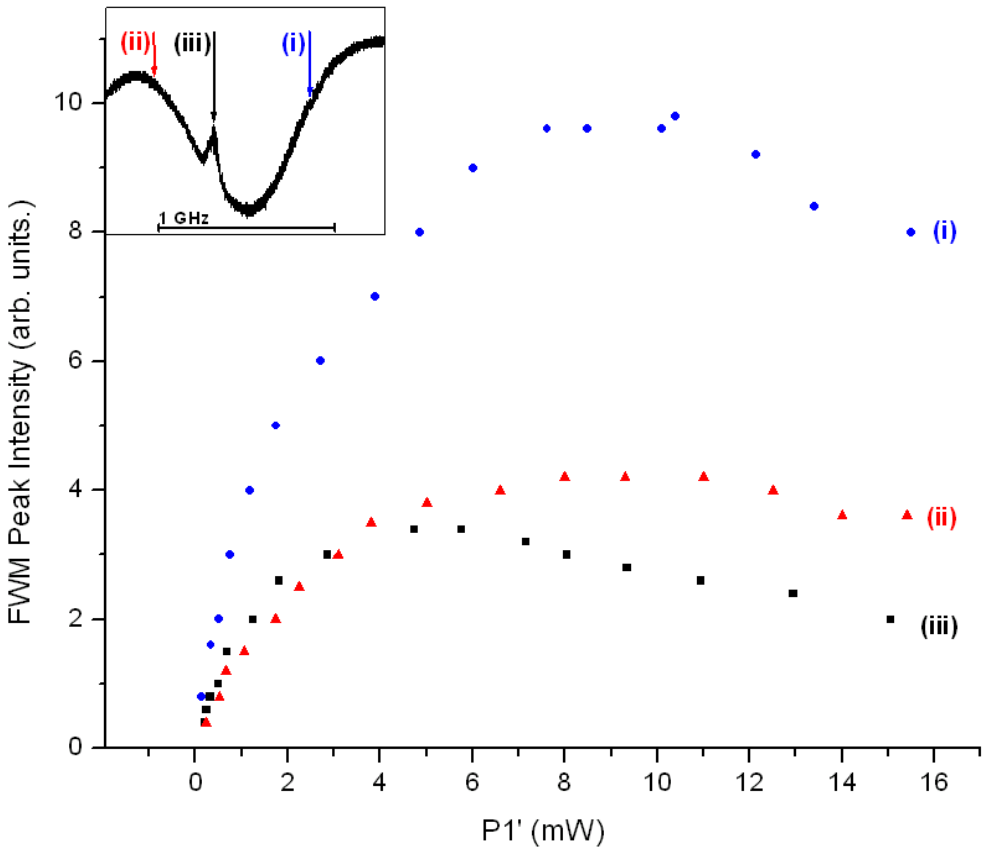

Fig. 6. Dependence of the FWM signal strength on the power P_1' at three different values of Δ_1 within the Doppler-broadened D_2 absorption linewidth. The powers of the other two beams are held fixed at $P_1 = 3$ mW and $P_2 = 22$ mW. The three chosen values of Δ_1, also shown in the inset, correspond to where (i) signal maxima occurs at the blue detuned region (blue dots), (ii) signal maxima occurs at the red detuned region (red triangles), and (iii) signal minima occurs towards the center-red detuned region (black squares). The EIT peak visible in the inset corresponds to case (iii). The three signal trends are connected by lines to aid the eye.

coherence due to $\mathbf{E_1}$ begins to extinguish the FWM intensity. The rates of initial growth and subsequent extinction of the FWM radiation with increasing P_1' is different at different values of Δ_1, and is shown in Fig. 6. This behavior distinguishes this FWM process from the traditional cascade FWM configuration in which the signal is generated in the lower transition with two coupling beams in the upper transition and one probe beam in the lower transition. There, as the coupling beam intensity is increased, the FWM intensity grows until it reaches a maximum value where it remains constant, and signal extinction does not occur.

III.5. Summary

The vacuum mode between the upper excited states in a ladder-type configuration is parametrically amplified using atomic coherence mechanisms to enhance the third-order nonlinear response, and studied in the frequency domain. The generated radiation is background free, and its Doppler-free spectral waveform contains high-resolution information about the spectroscopic properties of the atomic energy levels. The line-shape, linewidth and intensity of the generated FWM radiation are determined by various factors such as the beam powers and associated power-broadening effects, the multilevel nature of the atoms and selection rules, the frequency detunings, the destructive interference effects due to contributions by multiple intermediate states, and the dual role of one of the coupling beams. The new radiation could find use in FWM-based applications, and the method can be used to improve procedures using two-photon fluorescence that typically have weak signals and large background noises.

IV. Interferometric control of spectral profiles of parametrically-amplified waves

IV.1. Introduction

In the previous two chapters, we demonstrated the spectral features of EIT as well as FWM radiation in the ladder-type configuration. It was seen that the spectral waveforms of the FWM signals have asymmetries due to the disparate transition amplitudes, multiplicities and decay channels of the nearly-overlapping energy levels. Effects related to the powers of the driving fields, such as power–broadening and Autler-Townes splitting of the energy levels, also have significant contributions to the generated signal waveforms. As a reminder, some examples of such asymmetries relevant for this chapter are shown in Fig. 1. In applications utilizing the full spectral bandwidth of these signals, for instance in multimode (multiplexed) communication or imaging, it will be advantageous to be able to control the spectral profiles externally, instead of relying solely on the waveform imparted by the atomic parameters.

In this chapter, we demonstrate a new method that allows external all-optical control over the waveforms of such EIT-assisted parametrically-amplified radiations. The method lies in modulating the phase of the generated signal across its bandwidth. The phase modulation can be measured by mixing the signal with a degenerate local oscillator (LO). The intensity profile of the resultant waveform can be tailored by controlling the frequency detunings and the rate of phase evolution between the driving beams. As will be demonstrated below, such external control paves the way for phenomena such as linewidth-narrowing, line shape symmetrization and spectral bandwidth-switching. We envisage that such control will be necessary in future applications that implement FWM radiations, such as optical communication and information processing. EIT-assisted FWM processes have already demonstrated to be efficient sources for

squeezed radiation and correlated photons, with demonstrated capacities for tunable entanglement, photonic memory and spatially multimode quantum applications. Such multimode applications can also be extended to the frequency domain, utilizing the spectral bandwidths of the signals. Thus it would be advantageous to have external all-optical control over their spectral waveforms. The phase sensitivity of the background-free FWM signal will also be an avenue for metrology and other interferometric applications. In these applications, the quantum properties inherent in the radiations that are parametrically amplified from the vacuum mode might make using them advantageous over using traditional radiation sources.

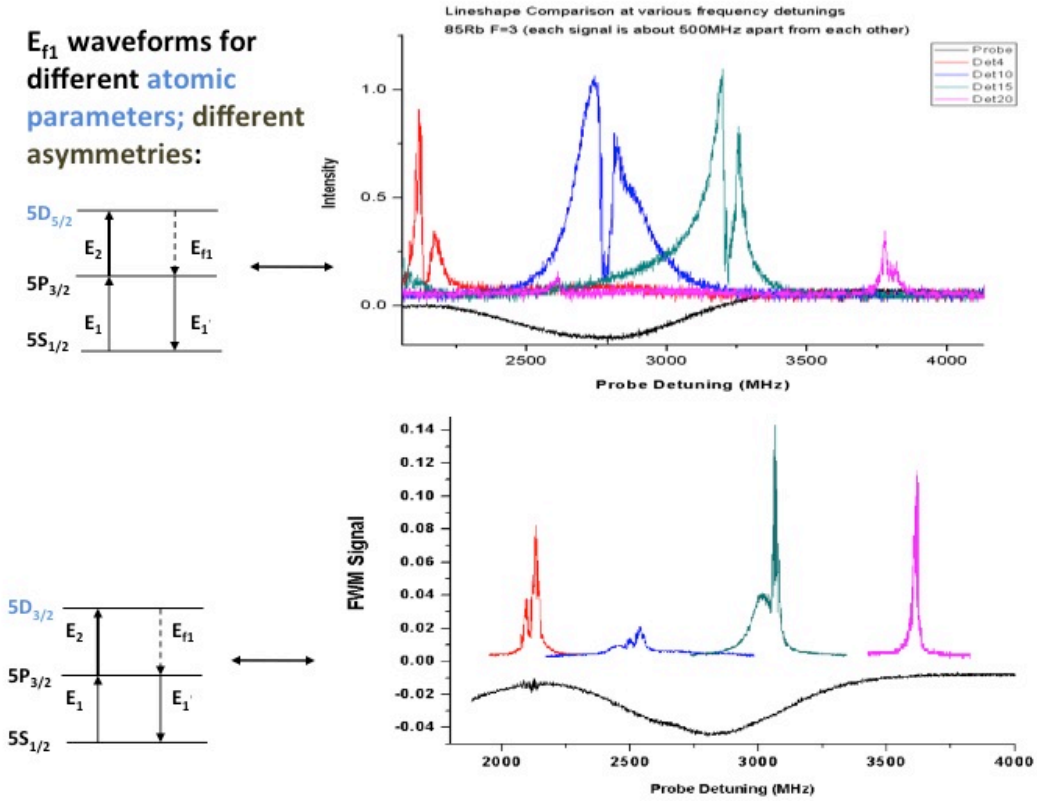

Fig. 1. Examples of FWM spectra at various intermediate frequencies in two ladder-type systems. Line shape asymmetries arise due to the different multiplicities and spectroscopic natures of the hyperfine levels that are involved while driving the three fine structures.

IV.2. Experimental method

The method utilizes the sensitivity of the FWM signal's phase to the driving beam's phases in the closed atomic contour being driven in the parametric amplification process. By making the phase difference between the driving beams evolve as their frequency is scanned, we impart the phase evolution to the generated signal across its bandwidth. For the waveform control being considered here, the phase difference between the driving beams has to evolve in the frequency domain, and a time-domain phase evolution will not suffice.

The signal is obtained by a FWM process that parametrically amplifies the vacuum mode between the two excited states in three-level ladder-type configuration in rubidium vapor (Fig. 1). The atomic system driven in this experiment is similar to the one in Chapter 3, but several modifications are made to the beams and to the detection method: the beam polarizations are altered so that the frequency-degenerate beams now have linear polarizations lying in the same plane for interference; phase control has been added to a beam pair in a gross- and fine-tunable unbalanced arm Mach-Zehnder configuration; and the detection method now involves a local oscillator mixed with the FWM signal.

The two beams $\mathbf{E_1} = A_1 e^{-i(\omega_1 t - \mathbf{k_1} z + \phi_1)}$ and $\mathbf{E_1}' = A_1' e^{-i(\omega_1 t - \mathbf{k_1'} z + \phi_1')}$, generated from the same diode laser DL_1 (wavelength $\lambda_1 = 2\pi/|\mathbf{k_1}| = 2\pi/|\mathbf{k_1}'| = 780$ nm, frequency $\omega_1 = 2\pi\nu_1$), cross at a small angle ($\theta = 0.4°$) inside the magnetically shielded vapor cell at a temperature of 60 °C (Fig. 1b). Here, A_i and $|\mathbf{k_i}| = 2\pi/\lambda_i$ are the amplitude and wave vector or the field $\mathbf{E_i}$, respectively. A function generator scans ν_1 across the Doppler-broadened width of the lower transition of the cascade configuration at a rate of $R \approx 1$GHz / ms, resulting in a continuous-wave (cw)-output (linewidth 1 MHz) with a slowly varying frequency $\Delta\nu_1(t) = Rt$. The path length difference $L = L_1' - L_1$, where L_1' (L_1) is the distance $\mathbf{E_1}'$ ($\mathbf{E_1}$) traverses between DL_1 and the

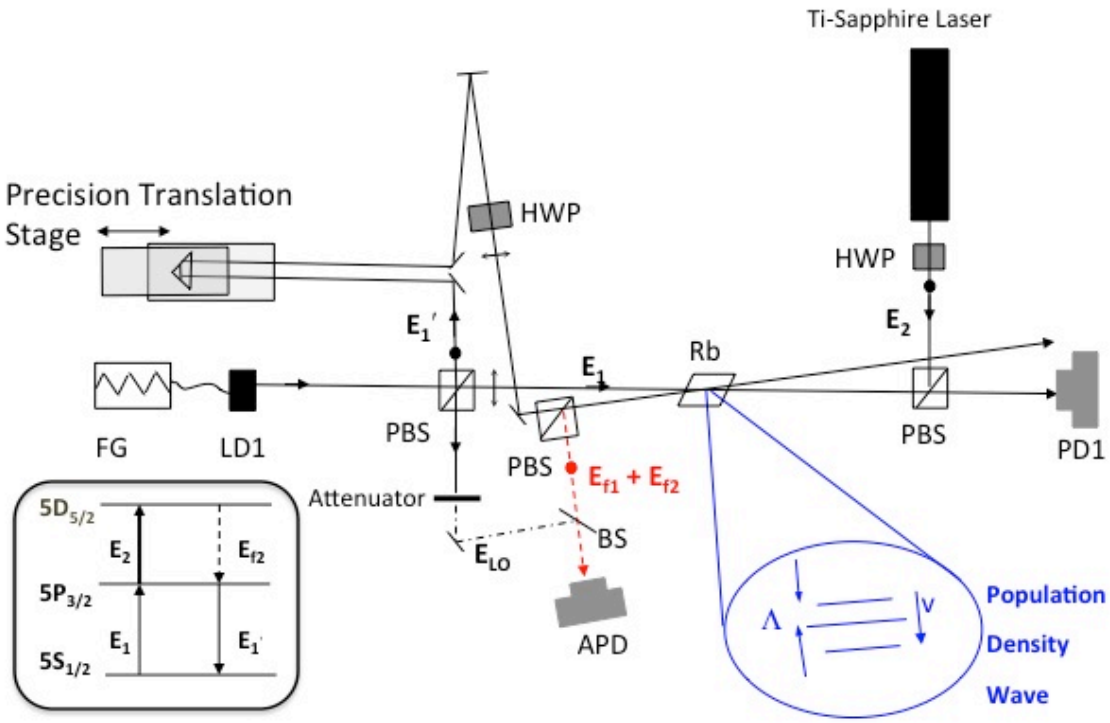

Fig. 2. Atomic configuration (inset) and experimental setup. FG = function generator, LD_1 = laser diode 1, (P)BS = (polarization) beam splitter cube, HWP = half-wave-plate, PD_1 = photodiode 1 (detects the transmitted $\mathbf{E_1}$), APD = avalanche photodiode (detects $\mathbf{E_f} + \mathbf{E_{LO}}$). The population density wave is discussed in the text.

beam-crossing region, can be altered with nanometer precision using a translation stage. A strong pumping beam $\mathbf{E_2} = A_2 e^{-i(\omega_2 t - \mathbf{k_2} z + \phi_2)}$ is generated from a Ti: Sapphire laser source (wavelength $\lambda_2 = 2\pi/|\mathbf{k_2}| = 775.978$ nm, frequency $\omega_2 = 2\pi\nu_2$) and aligned to overlap and counter-propagate with $\mathbf{E_1}$ inside the vapor cell. The cw-beam $\mathbf{E_2}$ has a fixed wavelength (linewidth 0.75 MHz) corresponding to the upper transition of the ladder-type configuration. The Gaussian beam areas are approximately 1.1 sq. mm. ($\mathbf{E_1}$ and $\mathbf{E_1'}$) and 1.45 sq. mm. ($\mathbf{E_2}$) in the interaction region. $\mathbf{E_1}$ and $\mathbf{E_1'}$ have the same linear polarization, which is orthogonal to the polarization of $\mathbf{E_2}$. The

new radiation generated in the FWM process, $\mathbf{E_f} = A_f e^{-i(\omega_f t - \mathbf{k_f} z + \phi_f)} \propto \chi^{(3)}(\mathbf{E_1'})^* \mathbf{E_2} \mathbf{E_1}$, has frequency $\omega_f = \omega_2 + \omega_1 - \omega_1' = \omega_2$, wave vector $\mathbf{k_f} = \mathbf{k_2} + \mathbf{k_1} - \mathbf{k_1'} = -\mathbf{k_1'}$, phase $\Phi_f = \Phi_2 + \Phi_1 - \Phi_1'$, and polarization similar to that of $\mathbf{E_2}$. The third-order of the nonlinear susceptibility, $\chi^{(3)}$, comprises of all the detuning factors and dipole moment strengths. Depending on the two-photon detuning, the FWM gain has two different scattering mechanisms, which we will describe first before discussing the phase-modulation process.

When the two counter-propagating beams $\mathbf{E_1}$ and $\mathbf{E_2}$ satisfy the two-photon resonance (TPR) condition between the ground state and the upper-excited state of the cascade configuration, an EIT coherence is established whose linewidth is basically Doppler-free even though the absorption width of the lower transition is Doppler-broadened. At EIT coherence, absorption of the fields is suppressed even with all the atoms in the ground state, while the nonlinearity that gives rise to FWM is enhanced. $\mathbf{E_1'}$ induces stimulated emission in the phase-matched direction $\mathbf{k_f}$, resulting in the FWM signal $\mathbf{E_{f1}}$. The waveform of this signal is governed not only by the TPR features including power-broadening and Autler-Townes splitting, but also by the various closely lying hf sublevels of the excited state that lie within the EIT linewidth. Since the hf levels have different multiplicities and transition strengths, their contributions to the generated signal vary in strength, inducing asymmetries in the generated waveform (Fig. 1 and 6(a)). The powers of the driving beams P_1, P_1' and P_2 are optimized to maximize $\mathbf{E_{f1}}$'s peak strength. Depending on the frequency detunings, these power values can be quite different.

The two beams $\mathbf{E_1}$ and $\mathbf{E_1'}$ form a spatial intensity grating with a spatial period of $\Lambda = \lambda_1/\sin(\theta/2)$. Simultaneously scanning the frequencies of the near-infrared (~ 384 THz) beams by a few gigahertz has a negligible effect on Λ. Outside the EIT linewidth, the intensity grating will result in a population-density grating[114] which, as the frequency is scanned, is hosted by different

atomic velocity classes within the Doppler-broadened absorption bandwidth. Part of the upper coupling beam scatters off this spatial grating in the phase-matched direction. Since TPR is not satisfied in this case, the scattering is very inefficient and a local oscillator (LO) is needed to observe this scattered field. To distinguish it from the TPR-enhanced radiation $\mathbf{E_{f1}}$, in which case all the atoms are in the ground state and no population-density grating is formed but the signal is enhanced due to EIT coherence, we call this signal $\mathbf{E_{f2}}$.

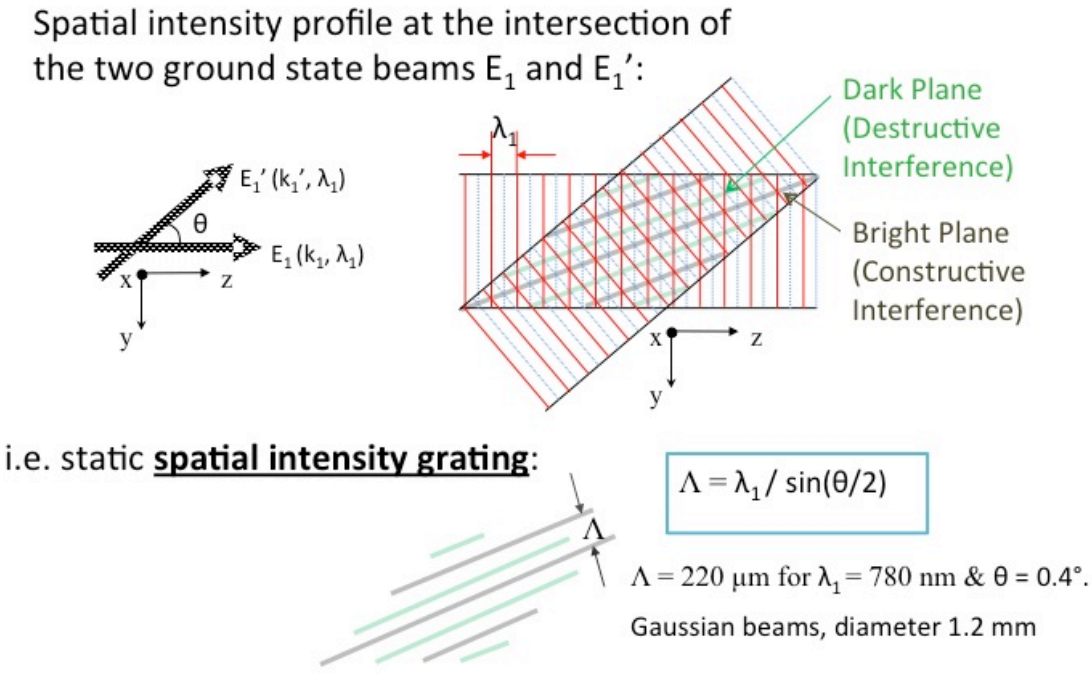

Fig. 3. Pictorial representation of the static spatial intensity grating due to the two optical fields, and the values of the physical parameters in this experiment.

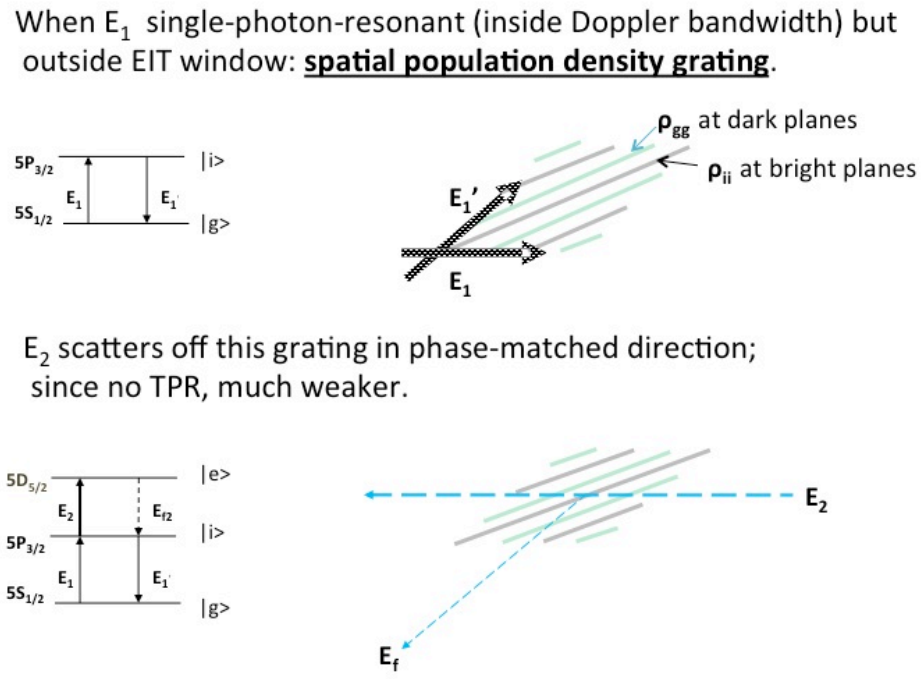

Fig. 4. Population density grating that occurs when the optical intensity grating is formed in a volume of resonant atoms, and the grating-scattered FWM signal.

In order to add phase modulation to the spectral waveform of the FWM signal, we make the phase difference between the grating beams $\mathbf{E_1'}$ and $\mathbf{E_1}$, $\Delta\Phi_1$, evolve as their frequency ν_1 is swept. We achieve this control by setting a Mach-Zehnder interferometer with unbalanced arms for the frequency-swept beams, so that $\Delta\Phi_1 = 2\pi c^{-1} (L\Delta\nu_1)$. The spectral period in which $\Delta\Phi_1$ evolves by 2π is $\Gamma(\text{Hz}) = cL^{-1}$. This phase information $\Delta\Phi_1(\nu_1)$ propagates to the FWM signal phase, yielding $\Phi_f(\nu_1) = \Phi_2 + \Phi_1 - \Phi_1' = \Phi_2 - \Delta\Phi_1(\nu_1)$. The modulated phase of the scattered wave $\mathbf{E_{f2}}$ is measured by homodyning with a LO field $\mathbf{E_{LO}} = A_{LO} e^{-i(\omega_f t - \mathbf{k_f} z + \phi_{LO})}$, which is obtained by attenuating the unscattered field $\mathbf{E_2}$ (Fig. 2b). We note that while $\Phi_f(\nu_1)$ evolves linearly with ν_1, the phase difference between E_2 and the derived E_{LO}, $\Phi_0 = \Phi_2 - \Phi_{LO}$, does not evolve and is a constant across ν_1. The resulting signal intensity $I \propto |\mathbf{E_f} + \mathbf{E_{LO}}|^2 = A_f^2 + A_{LO}^2 +$

$2A_fA_{LO}\cos(\Phi_0 - \Delta\Phi_1(\nu_1))$ thus contains fringes as ν_1 is scanned across the signal's bandwidth, the properties of which can be controlled via L and the frequency detunings. Depending on the frequency detunings, the modulations are seen in $\mathbf{E_f} = \mathbf{E_{f1}}$ or $\mathbf{E_f} = \mathbf{E_{f2}}$.

In the grating picture, a phase-evolution between $\mathbf{E_1}'$ and $\mathbf{E_1}$ results in a moving grating, which in turn implies the conversion of the static population-density grating into a population-density wave (PDW). The PDW has a speed $\mathbf{v} = \Lambda\Omega = (\lambda_1/\sin(\theta/2))(c^{-1}RL)$, with wavelength $\Lambda=\lambda_1/\sin(\theta/2)$ and frequency $\Omega = c^{-1}RL$. The scattered FWM signal, which initially had a frequency ω_f when the grating was static, is now frequency-shifted by Ω and the new frequency is $\omega_f \pm \Omega$, where the sign depends on the signs of R and L. Thus, when mixing this signal with a LO at frequency ω_f, a beat-signal is observed at frequency Ω. Using the relation $\Delta\nu_1(t) = Rt$, we see that in the time period Ω^{-1}, the frequency has scanned the spectral width $\Delta\nu_1(\Omega^{-1}) = R\Omega^{-1} = R\,(c^{-1}RL)^{-1} = cL^{-1}$. This value is precisely the spectral period $\Gamma(\text{Hz}) = cL^{-1}$ of the precious paragraph, thus showing the equivalence of this time-domain heterodyne picture with that spectral-domain homodyne picture.

- Fourier-domain evolution:
  $\Delta\Phi = 2\pi c^{-1}(L\Delta\nu_1 + \nu_1\Delta L) = 2\pi c^{-1}(L\Delta\nu_1)$
- Spectral period : $\Gamma\,(\text{Hz}) = cL^{-1}$
- Frequency scan : $\Delta\nu_1(t) = Rt$
- Temporal period : $\Omega^{-1} = cR^{-1}L^{-1}$
- **Population Density Wave :**

  $v = \Lambda\Omega = (\lambda_1/\sin(\theta/2))(c^{-1}RL)$

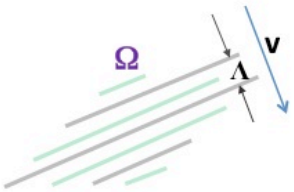

Fig. 5. Pictorial description of the population density wave (PDW), and the equations for the various parameters.

IV.3. Experimental results

The top trace in Fig. 6 (measured by the APD) shows the spectral regions supporting $\mathbf{E_{f1}}$ (Fig. 6a) and $\mathbf{E_{f2}}$ (Fig. 6b) as ν_1 is scanned across the Doppler-broadened bandwidth with L = 3.2 m. The input beam powers are P_1= 2.8 mW, P_1'= 9.6 mW and P_2 = 25 mW. The transmission of $\mathbf{E_1}$ after passing through the vapor cell, as measured by PD_1, is also shown for reference (lower blue trace), showing the TPR's spectral position. It is clear that while $\mathbf{E_{f1}}$ is limited within the linewidth of the Doppler-free TPR, $\mathbf{E_{f2}}$ is hosted by the entire Doppler-broadened absorption bandwidth with an amplitude that becomes weaker with increasing separation from the TPR. The peaks repeat as ν_1 scans a frequency interval of $\Gamma = cL^{-1}$ = 0.094 GHz, which is the spectral

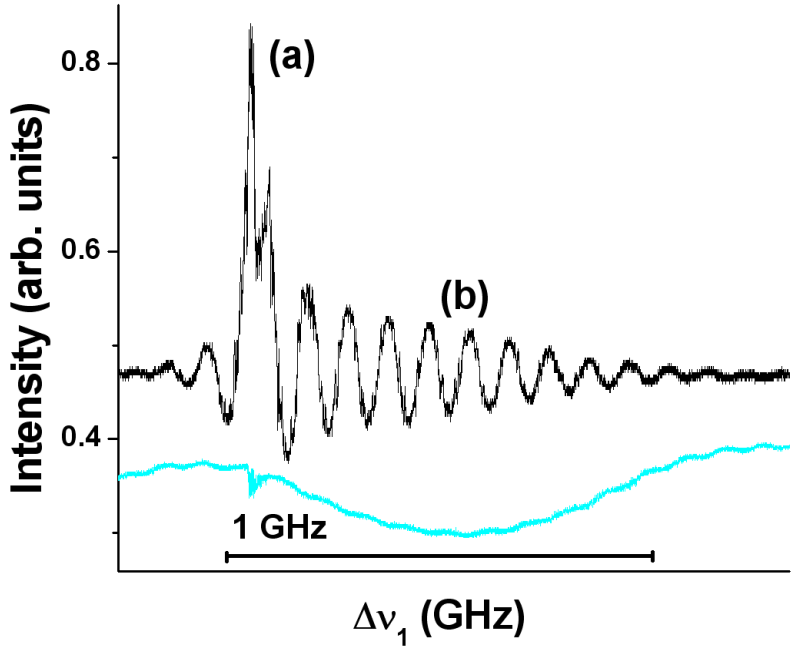

Fig. 6. The top and bottom (blue) traces correspond to measurements by the APD and PD_1, respectively. Here, L=3.2 m (Γ=0.094GHz). **(a)** At TPR, a Doppler-free FWM signal $\mathbf{E_{f1}}$ is observed. **(b)** Outside TPR, $\mathbf{E_{f2}}$ is hosted by the Doppler-broadened bandwidth.

period of $\Delta\Phi_1$. (Equivalently, in the time domain, the beat signal has a temporal period of $\Omega^{-1} = cR^{-1}L^{-1} = 0.12$ ms, resulting from the frequency-shift imparted by the PDW with $\Lambda = 220$ μm, $\Omega = 8.2$ kHz, and v = 1.64 m/s).

We can cause a spectral translation of the $\mathbf{E_f}$ peaks by fine-tuning the relative phase offset between the ground state beams; for instance, changing L by $\lambda_1/2$ causes a π phase-shift in $\Delta\Phi_1$, translating the peaks by $\Gamma/2$. A π phase-shift in $\Delta\Phi_1$ can also be incurred by a half-wave retarder placed in the path of $\mathbf{E_1}$ or $\mathbf{E_1'}$. Such a phase-induced shift of signal peaks gives rise to different phenomena for different values of Γ, as will be shown below.

IV.3.A. Linewidth narrowing

As a first example, we consider a case where a spectral translation of the phase alters the linewidth of the resultant signal, as shown in Fig. 7. Here, Γ has been increased by reducing L to 1.73 m (from 3.2m as used in Fig. 6). The Doppler-free EIT window in the Doppler-broadened absorption profile of $\mathbf{E_1}$ (lower trace) shows the spectral position of the TPR that is used for $\mathbf{E_{f1}}$ generation in both the APD traces (a) and (b). All the other experimental parameters, including the beam powers ($P_1 = 8$ mW, $P_1' = 8.5$ mW and $P_2 = 46.5$ mW), frequency detunings, cell temperature and beam geometry are the same in traces (a) and (b); the only difference is a π-phase shift of $\Delta\Phi_1$, which is achieved by a change in L by 400 nm ≈ $\lambda_1/2$. In this particular example, a spectral translation of $\Delta\Phi_1$ by $\Gamma/2$ alters the spectral positions of the constructive and destructive interferences, causing the linewidth of $\mathbf{E_{f1}}$ in (a) to decrease by a factor of 2.5 in (b). The result can be compared to intra-cavity linewidth-narrowing processes [117, 118], except here, the narrowing is achieved in a cavity-less configuration.

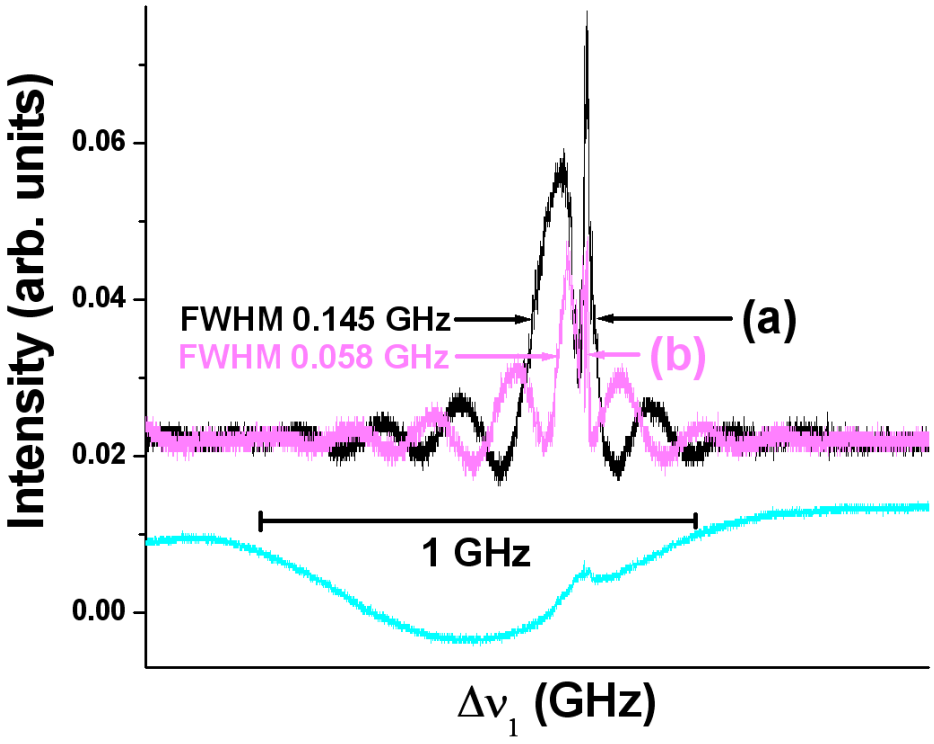

Fig. 7. The top and bottom (blue) traces correspond to measurements by the APD and PD_1, respectively. Here, L=1.73m (Γ=0.173 GHz). A π-phase shift of $\Delta\Phi_1$ causes Φ_f to spectrally translate, causing the linewidth of $\mathbf{E_{fl}}$ in **(a)** to decrease, in this particular example, by a factor of 2.5 in (**b).**

IV.3.B. Line shape symmetrization

As a second example, we illustrate the phenomena of line shape symmetrization (Fig. 8). When the TPR is placed at the blue-detuned edge of the Doppler-broadened absorption profile, the signal $\mathbf{E_{fl}}$ is highly asymmetric (Fig. 8((i))). The asymmetry arises due to the closely-lying

hyperfine levels in the $5D_{5/2}$ state partaking in the FWM process, each of which have different multiplicities and transition strength amplitudes. The stronger gain at smaller detuning occurs because of the inversion of the hyperfine levels in this upper excited state. Here, controlling the spectral phase offset of $\mathbf{E_f}$ with respect to $\mathbf{E_{LO}}$ can be used to symmetrize the resultant lineshape (Fig. 8((ii)). The path length difference has been reduced to L = 0.1 m, where Γ is comparable to the Doppler-broadened-absorption bandwidth.

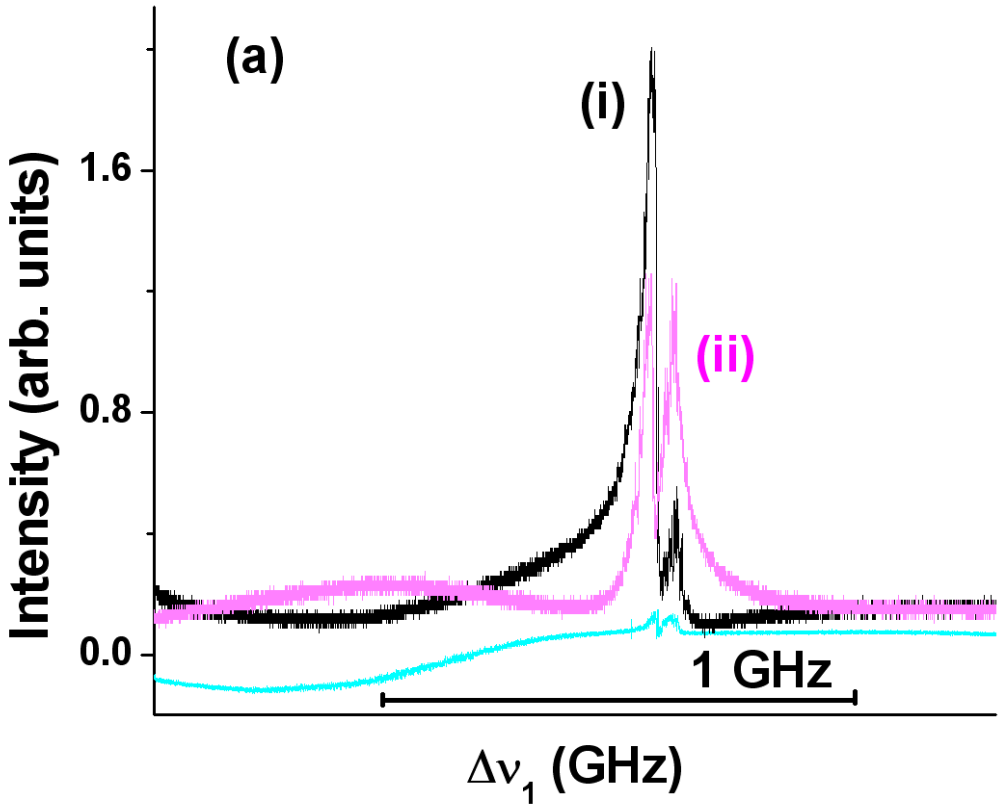

Fig. 8. The top and bottom (blue) traces correspond to measurements by the APD and PD_1, respectively. Here, L=0.1 m (Γ=3 GHz). The TPR is placed at the blue-detuned edge of the Doppler-broadened absorption profile. Here, a π-phase shift of $\Delta\Phi_1$ causes the highly asymmetric $\mathbf{E_{f1}}$ signal in (i) to be symmetric in (ii).

IV.3.C. Spectral bandwidth switching

At certain frequency detunings, this phenomenon becomes even more drastic. In Fig. 9 the TPR is placed at the center of the Doppler-broadened absorption profile (lower trace), as is shown by the EIT window's spectral position. The signal linewidth is much broader here due to power-broadening of the intermediate energy level. Here, we observe a phase-induced switching of the resultant signal from one spectral bandwidth (i) to another (ii). A π-phase shift in $\Delta\Phi_1$ shifts the position of the signal centroid in the frequency domain by 160 MHz. Such a high-resolution phase-sensitive optical switch integrating $\chi^{(3)}$ nonlinearities can be useful in optical and quantum communication and computation, and complements the sensitive switching of intensity from one spatial channel to another as was demonstrated in Ref. 115. The novelty of the current method is that the switching is achieved in the spectral domain, and without any alterations to the input beam intensities, directions or frequency detunings; the visibility contrast of nearly 1 is achieved solely via relative-phase control between the driving beams.

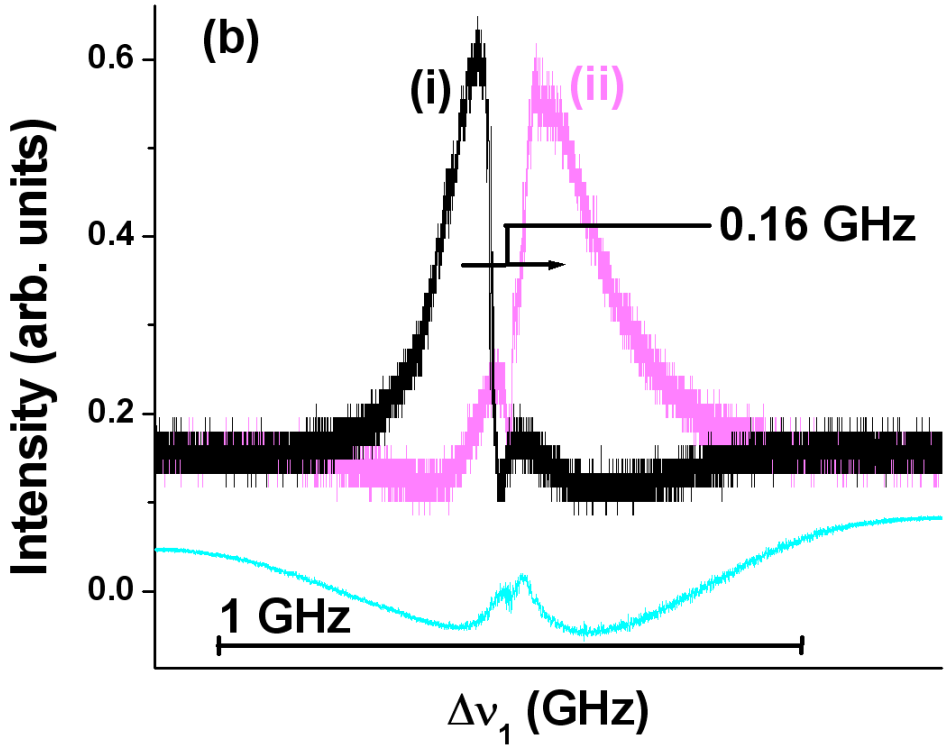

Fig. 9. The top and bottom (blue) traces correspond to measurements by the APD and PD_1, respectively. Here, L=0.1 m (Γ=3 GHz). The TPR is placed at the center of the Doppler-broadened absorption profile. Here, a π-phase shift in $\Delta\Phi_1$ shifts the position of the signal centroid in (i) by 160 MHz in (ii).

IV.4. Conclusions and outlook

In summary, we have experimentally demonstrated an all-optical phase-modulation of a parametrically-amplified waveform across its bandwidth. The interference between the FWM field and a degenerate LO enables a shaping of the resultant signal waveform, allowing for tasks

such as line shape symmetrization, linewidth-narrowing and bandwidth switching. Instead of pre-defining the phase to control the waveforms, we can also use the system to sense motion by incorporating target mirrors in the paths of the beams $\mathbf{E_1}$ and $\mathbf{E_1'}$. Slight motions can then be measured from the drastic changes in the interference pattern. Such motion sensitivity, and the fact that FWM is an ideal source of squeezed radiation reducing quantum noise in interferometric measurements[116], could make this method a powerful tool in metrological applications. One feature we have not mentioned in this thesis is that the spectral phase evolution is also very sensitive to the velocity of the translational stage, if it is moving, due to additional phase evolution. Depending on the sign of the velocity, the fringe density can either increase or decrease. Thus this method can be used to measure not only changes in path-length, but also the velocity of moving mirrors. Correspodingly, a controlled motion of the mirror can be used to change the fringe density by large amounts much quicker than it will be possible by varying L. This will be useful if the information content is to be encoded in the number of fringes that appear within the FWM signal's total gain bandwidth.

V. Spatial and temporal interferences between FWM and SWM

V.1. Introduction

In the previous two chapters, we discussed FWM in a ladder-type atomic system. In this chapter, we extend the study of multi-wave mixing processes in multi-level atoms to higher order nonlinearities. Specifically, we will use a four-level inverted-Y atomic system to drive a six-wave mixing (SWM) process, which has its origins in the fifth order term of the nonlinear polarization that is coupled to $\chi^{(5)}$. Here also, dark-state resonance will be used to enhance the multi-wave mixing process, thus allowing the measurement of the SWM signal using weak mW-level continuous-wave driving beams. Furthermore, in the same four-level atomic system, we will show the coexistence of this SWM process with another FWM process. By carefully aligning the beam geometries, we can choose to phase-match these two nonlinear processes so that the two atom-radiated signals occupy the same spatial mode, and can be measured in the same photodiode. Our experimental design also allows us to control the relative phase and amplitude between these two signals, and in fact we can even make the SWM signal stronger than the FWM signal. By making the two signals equal in strength and varying the relative phase between them, we can measure their interference via the resulting output intensity. Through the variation in visibility of the intensity in the spatial and temporal domains, we verified the coherence between these processes arising from different orders of the atomic nonlinearity. The temporal evolution of the fringes also allowed us to measure the resonant frequency of the $5D_{5/2}$-$5P_{3/2}$ transition in ^{85}Rb, the host atom.

In this chapter, first, we will describe the experimental method. We will describe the phase-matching geometries that allow us to control the output modes of the two signals and

make them overlapping. We will also carefully describe how we can control the relative phase and relative amplitude between these two signals, and discuss the detection scheme for measuring temporal and spatial interferences. We will then present the experimental results. We will show the spatial-temporal interferograms, and the use of the temporal phase evolution to measure the resonant frequency of the $5D_{5/2}$ -$5P_{3/2}$ in ^{85}Rb.

We note that this chapter deals with a single-phase measurement process. We later extended this system to allow the coexisting and phase-coherent nonlinearities to measure two phases simultaneously, which will be discussed in the next chapter.

V.2. Experimental setup

V.2.A. Atomic system and phase-matching beam geometry

Our atomic system and experimental arrangement are shown in Fig. 1. The atomic system consists of a four-level inverted-Y type configuration in ^{85}Rb atoms, comprising of the states $5S_{1/2}$ F = 2 ($|a\rangle$), $5S_{1/2}$ F = 3 ($|d\rangle$), $5P_{3/2}$ ($|b\rangle$) and $5D_{5/2}$ ($|c\rangle$). The atomic vapor cell, which is 5 cm long, is magnetically shielded and heated to 60° C. We coherently drive the third- and fifth-order nonlinearities in this atomic medium using 5 external driving beams $\mathbf{E_1}$, $\mathbf{E_2}$, $\mathbf{E_2'}$, $\mathbf{E_3}$ and $\mathbf{E_3'}$, where $\mathbf{E_i} = A_i e^{-i(\omega_i t - \mathbf{k_i} z + \Phi_i)}$, $\mathbf{A_i}$ are the field amplitudes, ω_i are the frequencies and $\mathbf{k_i}$ are the wavevectors. The pair of driving beams $\mathbf{E_2}$, $\mathbf{E_2'}$ originates from the same narrow-linewidth cw diode laser LS_2, and are thus phase-coherent. Similarly, the pair of driving beams $\mathbf{E_3}$, $\mathbf{E_3'}$ originates from the same narrow-linewidth cw Ti-Sapphire laser LS_3, and are thus phase-coherent. The probe beam $\mathbf{E_1}$ originates from yet another narrow-linewidth cw diode laser LS_1.

The beam frequencies ω_1, ω_2 and ω_3 are tuned to the atomic transition frequencies ω_{ba}, ω_{cb} and ω_{bd} with frequency detunings $\Delta\omega_1 = \omega_1 - \omega_{ba}$, $\Delta\omega_2 = \omega_2 - \omega_{cb}$ and $\Delta\omega_3 = \omega_3 - \omega_{bd}$, respectively, where $\omega_{ij} = (E_j - E_i)/\hbar$ with E_i the energy of the atomic level $|i\rangle$. ω_1 and ω_2 are held fixed, while ω_1 is swept across the Doppler-broadened spectral bandwidth of the $|b\rangle \rightarrow |a\rangle$ transition. Once the nonlinearities have been optimized, ω_1 is also changed from scanning mode to a fixed mode to study spatial and temporal phase coherence of the signal fields. The weak probe beam $\mathbf{E_1}$, travelling along the **z** direction, counter-propagates with the rest of the driving beams at small angles. Beam $\mathbf{E_2}$ travels along the –**z** direction. At any plane transverse to the probe beam's direction, the driving beams pass through the four corners of a square with $\mathbf{E_3'}$ furthest to $\mathbf{E_2}$. Each side of the square subtends an angle of 0.3° at the center of the vapor cell, where all beams intersect. The utility of this "square-box" configuration will be discussed more later. At the intersection region, the powers of the Gaussian beams $\mathbf{E_1}$, $\mathbf{E_2}$, $\mathbf{E_2'}$, $\mathbf{E_3}$, $\mathbf{E_3'}$ are approximately 3 mW, 40 mW, 4 mW, 67 mW, 67 mW respectively. A computer-controlled nanometer-precision translational stage is placed in the path of $\mathbf{E_2'}$ for phase modulation.

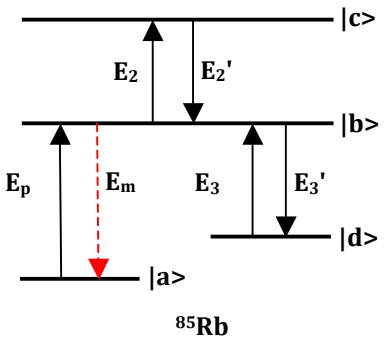

Fig. 1(a)

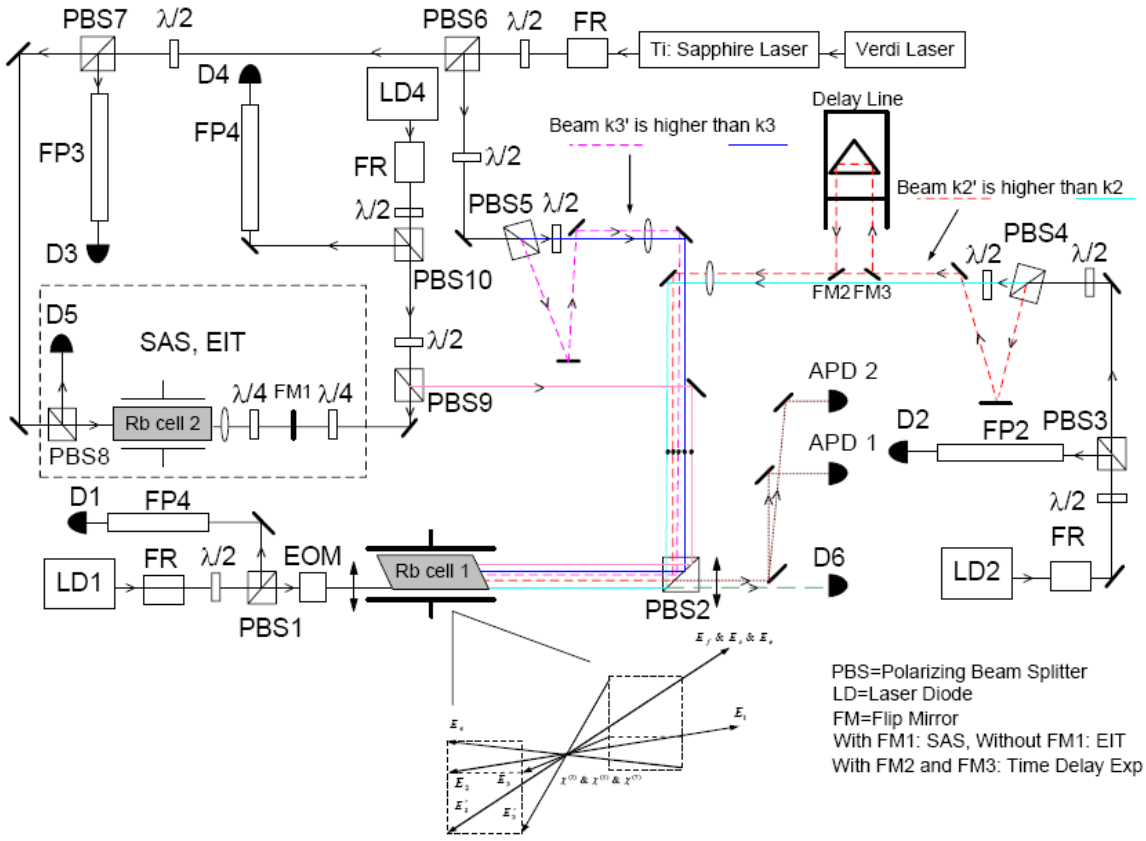

Fig. 1(b)

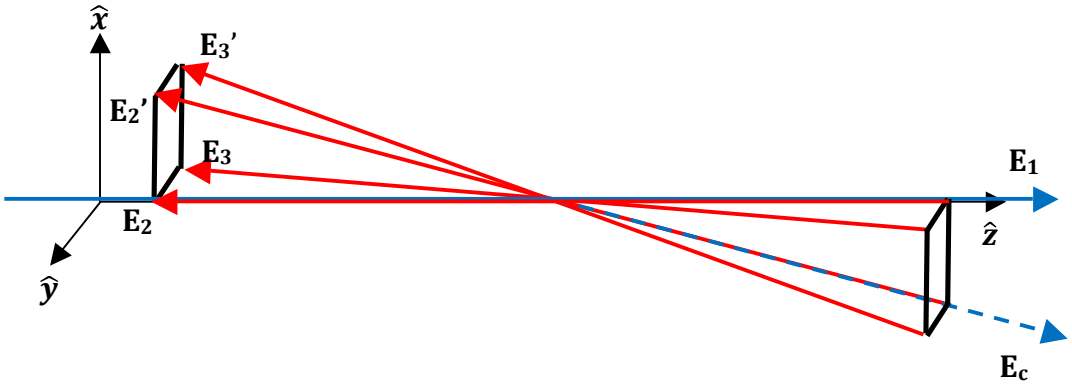

Fig. 1(c)

Fig. 1. (a) Atomic configuration and (b) top-view of the complete experimental setup. (c) Three-dimensional beam arrangement in the interaction region inside the vapor cell.

Due to this counter-propagating beam geometry, and the condition $\Omega_1 << \Omega_2$, the coupling beam $\mathbf{E_2}$ opens a Doppler-free EIT window for the probe beam $\mathbf{E_1}$ in the ladder-type subsystem (TPR frequency = $\omega_1 + \omega_2$). However, in the lambda-type subsystem (TPR frequency = $\omega_1 - \omega_3$), the counter-propagating geometry of the beam $\mathbf{E_3}$ does not satisfy the phase-matching condition necessary for a Doppler-free EIT window for $\mathbf{E_1}$. The single ladder-type EIT window for $\mathbf{E_1}$ due to $\mathbf{E_2}$ is used to enhance two nonlinear processes: one FWM, and one SWM.

The FWM signal is generated by mixing the field $\mathbf{E_2'}$ with the ladder-type EIT coherence in the three-level sub-system as shown in Fig. 2(a), giving rise to the signal field

$$\boldsymbol{E_f} = \mathrm{A_f e^{-i(\omega_f t - \mathbf{k_f} z + \Phi_i)}} \propto \chi^{(3)}(\boldsymbol{E_2}')^{*}\boldsymbol{E_2}\boldsymbol{E_1}.$$

Here, the third-order of the nonlinear susceptibility, $\chi^{(3)}$, is related to the density matrix element $\rho_{ba}{}^{(3)}$ for the perturbative chain $\rho_{aa}{}^{(0)} \overset{\omega_1}{\rightarrow} \rho_{ba}{}^{(1)} \overset{\omega_2}{\rightarrow} \rho_{ca}{}^{(2)} \overset{-\omega_2'}{\longrightarrow} \rho_{ba}{}^{(3)}$. It comprises of the frequency detuning factors, relaxation rates, dipole moment strengths, atomic density, and beam Rabi frequencies:

$$\chi^{(3)} = \frac{-i\mu_{ba}{}^{2}\mu_{cb}{}^{2}N}{\varepsilon_0\hbar^3 d_1 d_2\left(d_1 + \frac{(\Omega_3 + \Omega_3{}')^2}{d_3}\right)}.$$

μ_{ij} is the electric dipole moment of the transition $|i\rangle \rightarrow |j\rangle$, N is the atomic density, $d_1 = \Gamma_{10} + i\Delta_1$, $d_2 = \Gamma_{20} + i(\Delta_1 + \Delta_2)$ and $d_3 = \Gamma_{30} + i(\Delta_1 - \Delta_3)$, where Γ_{ij} is the relaxation rate for the $|i\rangle \rightarrow |j\rangle$ transition. Note that the dressing effects due to the presence of the strong fields $\mathbf{E_3}$ and $\mathbf{E_3'}$ are also included in the susceptibility. The resulting FWM signal field $\mathbf{E_f}$ has wave vector $\mathbf{k_f}$

= $\mathbf{k_1} + \mathbf{k_2} - \mathbf{k_2'}$ and frequency $\omega_f = \omega_1 + \omega_2 - \omega_2' = \omega_1$, and is measured at the avalanche photo-diode APD_1

In generating the SWM signal, which utilizes the same EIT window supporting the FWM process, the field $\mathbf{E_2'}$ is blocked (Fig. 2(b)). Instead, the field $\mathbf{E_2}$ is used twice, and the SWM pathway is completed by using $\mathbf{E_3}$ and $\mathbf{E_3'}$ to drive transitions between the energy levels |b> and |d>. The SWM signal field is

$$\boldsymbol{E_s} = \mathrm{A_s} e^{-\mathrm{i}(\omega_s t - \mathbf{k_s} z + \Phi_s)} \propto \chi^{(5)} \boldsymbol{E_3} (\boldsymbol{E_3}')^* (\boldsymbol{E_2})^* \boldsymbol{E_2} \boldsymbol{E_p}$$

where the fifth-order of the susptibility, $\chi^{(5)}$, is related to the density matrix element $\rho_{ba}{}^{(5)}$ for the perturbative chain $\rho_{aa}{}^{(0)} \overset{\omega_1}{\rightarrow} \rho_{ba}{}^{(1)} \overset{\omega_2}{\rightarrow} \rho_{ca}{}^{(2)} \overset{-\omega_2}{\longrightarrow} \rho_{ba}{}^{(3)} \overset{-\omega_3'}{\longrightarrow} \rho_{da}{}^{(4)} \overset{\omega_3}{\rightarrow} \rho_{ba}{}^{(5)}$, or the identical $\rho_{aa}{}^{(0)} \overset{\omega_1}{\rightarrow} \rho_{ba}{}^{(1)} \overset{-\omega_3'}{\longrightarrow} \rho_{da}{}^{(2)} \overset{\omega_3}{\rightarrow} \rho_{ba}{}^{(3)} \overset{\omega_2}{\rightarrow} \rho_{ca}{}^{(4)} \overset{-\omega_2}{\longrightarrow} \rho_{ba}{}^{(5)}$:

$$\chi^{(5)} = \frac{2i\mu_{ba}{}^2 \mu_{cb}{}^2 \mu_{bd}{}^2 N}{\varepsilon_0 \hbar^5 {d_1}^3 d_2 d_3}$$

The resulting SWM signal field $\mathbf{E_f}$ has wave vector $\mathbf{k_s} = \mathbf{k_1} + \mathbf{k_2} - \mathbf{k_2} + \mathbf{k_3} - \mathbf{k_3'} = \mathbf{k_1} + \mathbf{k_3} - \mathbf{k_3'}$ and frequency $\omega_s = \omega_1 + \omega_2 - \omega_2 + \omega_3 - \omega_3' = \omega_1$, and is measured at APD_2.

At the line-center of the Doppler- broadened transition from |a> to |b>, due to a large ground-state population, only these EIT-supported signals, and the weak resonant probe beam $\mathbf{E_1}$, experience negligible absorption, and all other signal fields have a vanishing transmission. For instance, in Fig. 2(b), there is another SWM channel corresponding to a blocked $\mathbf{E_2}$ and unblocked $\mathbf{E_2'}$ used twice. However, because $\boldsymbol{\Omega_2'} << \boldsymbol{\Omega_2}$, this SWM is negligible. We limit our

treatment only to the two dominant signal fields which spectrally coexist at the line center, denoted by $\mathbf{E_c} = \mathbf{E_f} + \mathbf{E_s}$.

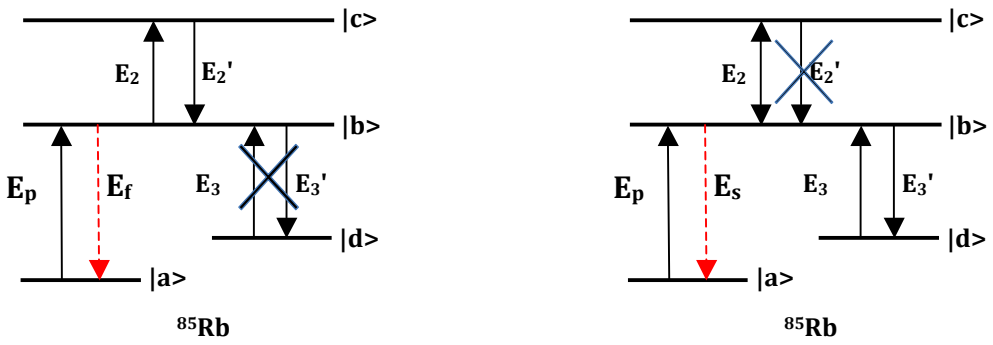

Fig. 2. The two sub-systems of the parent atomic configuration that are used to generate the (a) FWM signal and the (b) SWM signal, in the phase-matching directions that are discussed in the text. Each subsystem is attained when selected beams are blocked from the parent configuration, as shown by the thick X-marks. When none of the beams are blocked, both the sub-systems are driven simultaneously and we have coexisting FWM and SWM radiation.

We will now explain the rational for the chosen experimental geometry, and the various "knobs" that we have in this setup for controlling the relative direction, amplitude and phase between the two signal fields.

V.2.B. Controlling the relative direction between E_s and E_f

From our arrangement, it is clear that the generated FWM and SWM signals have the same frequency, $\omega_f = \omega_s = \omega_1$. Without the "square-box" geometry, however, their directions are not necessarily identical. Let θ_2 be the angle between beams $\mathbf{E_2}$ and $\mathbf{E_2'}$, whose wavelengths are λ_2 = 775.98 nm. Similarly, let θ_3 be the angle between beams $\mathbf{E_3}$ and $\mathbf{E_3'}$, whose wavelengths are λ_3 = 780.24 nm. The phase-matching conditions and the beam geometry implies that the FWM and SWM signals, whose wavelengths are $\lambda_f = \lambda_s = \lambda_1 =$ 780.23 nm, are radiated at angles very close to θ_2 and θ_3 from the direction of $\mathbf{E_1}$, respectively.

For the two signals $\mathbf{E_f}$ and $\mathbf{E_s}$ to have significant spatial overlap, the following two conditions have to be satisfied experimentally:

(i) $\theta_2 = \theta_3$

(ii) $(\boldsymbol{k_2} - \boldsymbol{k_2}') \parallel (\boldsymbol{k_3} - \boldsymbol{k_3}')$.

If these two conditions are not met, then the two nonlinear signals are spatially separated and can be measured using two different APD's. During such alignment, the study of these two signals can be performed individually and simultaneously, and features such as competition for beam energies and energy transfer between the two processes can be measured. We can also use this alignment to optimize the driving beam amplitudes and frequencies in order to attain the desired levels of signal enhancement for each nonlinear process.

The purpose of the current experiment is to test the phase-coherence between these two signals, for which it is desirable to make the two signals spatially overlapped so that the resulting interference pattern due to $\left|\boldsymbol{E_f} + \boldsymbol{E_s}\right|^2$ can be measured. To have the two signal fields radiate in the same direction, we need to satisfy the above two conditions. In the square box configuration, both conditions are satisfied, i.e. the two angles $\theta_2 = \theta_3 \equiv \theta$, and $\boldsymbol{k_2} - \boldsymbol{k_2}'$ is parallel to $\boldsymbol{k_3} - \boldsymbol{k_3}'$. Thus, the two signals are nearly overlapped, and can be measured at one site. We use a beam splitter and measure the resulting intensity using an APD and a charge-coupled device (CCD) camera simultaneously

In the square-box configuration, the net phase-mismatch between the two signals is $\Delta\boldsymbol{k} = \boldsymbol{k_f} - \boldsymbol{k_s} = (\boldsymbol{k_2} - \boldsymbol{k_2}') - (\boldsymbol{k_3} - \boldsymbol{k_3}')$. For the small value of θ_i that is used, we have the approximate relation $\left|\boldsymbol{k_i} - \boldsymbol{k_i}'\right| \approx k_i\theta_i$ for each $i = 2, 3$. Using $|\boldsymbol{k_2}| = \frac{2\pi}{\lambda_2}$ and $|\boldsymbol{k_3}| = \frac{2\pi}{\lambda_3}$, the net phase mismatch is then $\Delta k \approx \frac{2\pi|\lambda_2 - \lambda_3|\theta}{\lambda_2\lambda_3}$. Due to the near coincidence of the two wavelengths λ_2 and λ_3, and the small angle, the net phase mismatch is minimal. Nonetheless, due to the small, non-zero phase mismatch, we expect to measure a spatial interference pattern with a spatial period of $\frac{2\pi}{\Delta\boldsymbol{k}} \approx 3.3$ mm in a plane transverse to the signal propagation direction. In order to understand the non-zero phase-mismatch even when the two angles θ_2 and θ_3 are equal, it is helpful to imagine two (angularly) similar triangles with different side lengths (corresponding to wave-vector magnitudes). The difference in length of the shortest side of each triangle corresponds to the net phase mismatch, which is clearly nonzero for different-sized triangles even if they are angularly similar.

V.2.C. Controlling the relative amplitude between E_s and E_f

As we mentioned in the introductory chapter, the fifth-order of the nonlinear polarization is orders of magnitude weaker than the third-order nonlinearity. The special design of our setup allows us to tune the relative strength between the third-order and fifth-order transition amplitudes, so that the SWM signal can be made equal in strength, or even stronger, than the FWM signal. This feature of generating coexisting FWM and SWM signals in the same phase-matched direction and with equal amplitudes has allowed us to measure their interference fringes with good visibility and utilize their phase-coherence.

Our relative-amplitude control knob is the driving beam $\mathbf{E_2'}$. In order to understand this feature, we note that $\mathbf{E_2'}$ is involved only in the FWM transition pathway, and not in the SWM transition pathway. (The other two beams used to drive the FWM process, $\mathbf{E_1}$ and $\mathbf{E_2}$, are also shared by the SWM process.) Since only the FWM signal depends on the strength of $\mathbf{E_2'}$, we vary the power of this beam, P_2', to tune the FWM signal gain independently of the SWM signal gain. First, we block $\mathbf{E_2'}$ and tune the frequency detunings and powers of the remaining beams to maximize the SWM signal. Next, we block the driving beams $\mathbf{E_3}$ and $\mathbf{E_3'}$ to stop the SWM process, and turn on the beam $\mathbf{E_2'}$. At first, when this beam has a high power, the FWM signal strength is much stronger than the SWM signal strength. We then gradually decrease P_2' until the FWM signal intensity decreases and becomes of the same magnitude as the SWM signal. If we further reduce P_2', the FWM strength keeps getting weaker and we are in a regime where the SWM process is stronger than the coexisting FWM process.

While optimizing the values of the beam frequencies and powers, the probe beam $\mathbf{E_1}$'s frequency ω_1 is in the scanning mode. Once the FWM signal strength is optimized to be roughly

equal to the SWM strength and $\frac{A_s}{A_f} \approx 1$, the spectra of the two signals, and the common EIT window, look like the traces presented in Fig. 3. Once these conditions are found, ω_1 is held fixed at the spectral value where the signals have maximum gain, after which we proceed to test phase-coherence between the signals, as described in the next section.

V.2.D. Controlling the time delay between $\mathbf{E_2}$ and $\mathbf{E_2'}$

Once we find the conditions for $A_s = A_f \equiv A_c$ and stop scanning the probe frequency, we have two monochromatic signals having the same frequency impinging on the APD as well as on the CCD. This corresponds to a homodyne interferometry with two phase-matched nonlinear optical signals, and the resulting photocurrents depend on the relative phase difference between these two signals. In our setup, we hold the phase of the SWM signal fixed and scan the phase of the FWM with respect to the SWM signal's phase. So in as sense, the SWM acts like a LO to measure the beating with the FWM.

In order to vary this relative phase $\Delta\Phi$, we again note that the driving beam $\mathbf{E_2'}$ is involved only in the FWM process. The SWM process does not involve the field $\mathbf{E_2'}$; instead, it uses the field $\mathbf{E_2}$ twice, whose phase contributions cancel each other due to the term $(\mathbf{E_2}^*)\mathbf{E_2}$. Thus, only the phase of the FWM signal is dependent on the phase of $\mathbf{E_2'}$, as it involves the term $(\mathbf{E_2'}^*)\mathbf{E_2}$. By scanning the relative phase between $\mathbf{E_2'}$ and $\mathbf{E_2}$, we thus also modulate the phase of $\mathbf{E_f}$ with respect to $\mathbf{E_f}$, $\Delta\Phi$. We placed a computer-controlled nanometer-precision translation stage in the path of $\mathbf{E_2'}$, in order to vary the time-delay between the beams and $\mathbf{E_2}$ and $\mathbf{E_2'}$. A LabView program was made to automate the stage motion and data acquisition. As we scan the time delay between these two beams, we expect to see a temporal evolution of the resulting

intensity with a temporal period of $\frac{2\pi}{\omega_2}$. Since ω_2 is tuned to the resonant frequency ω_{cb} of the $5D_{5/2}$-$5P_{3/2}$ transition in ^{85}Rb, the expected temporal period is $\frac{2\pi}{\omega_{cb}} = 2.427$ fs.

V.3. Experimental results

As discussed in the experimental section, the probe beam is initially in the frequency-scanned mode for optimizing the spectra of the two signals. Here, the intermediate frequency detuning is indicated by the spectral position of the Doppler-free EIT window within the Doppler-broadened D2 absorption line. Since $\mathbf{E_f}$ and $\mathbf{E_s}$ are enhanced by this EIT window, these signals temporally and spectrally overlap. The two signals are optimized for equal field strengths. When both of the signals are phase-matched to overlap spatially, to measure the strength of an individual signal, we have to null the other signal (otherwise interference modulates the resultant signal.) To measure only the SWM signal, we block the driving beam $\mathbf{E_2'}$. To measure only the FWM signal, we block the beams $\mathbf{E_3}$ and $\mathbf{E_3'}$. In each case, if any one of the remaining beams is blocked, then the signal completely disappears, verifying that the generated signal is indeed due a SWM or a FWM process. An example showing the measured traces, for the condition where the SWM signal is slightly stronger than the FWM signal, is presented in Fig. 3.

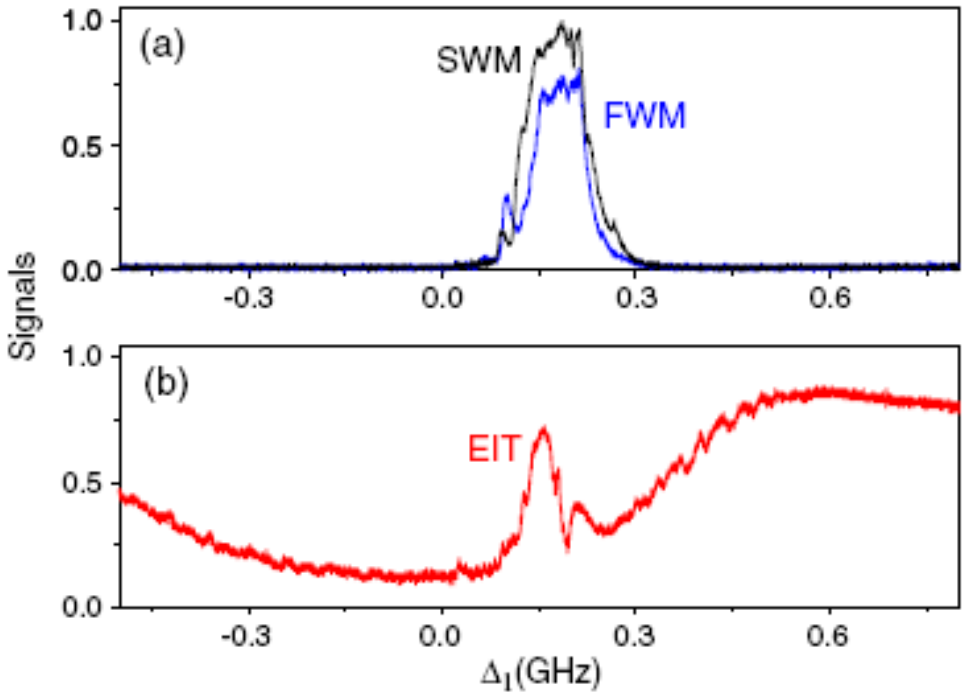

Fig. 3. An example of a measurement in which the SWM signal is slightly stronger than the FWM signal. These traces are taken when the probe beam's frequency is in the scanned mode. The overlap of the two signals with the common EIT window is evident.

V.3.A. Spatial and temporal interference between FWM and SWM

Once the signal strengths are optimized to be identical, the frequency of the probe beam is held fixed at the spectral value yielding the maximum gain. The interference of the resulting overlapped monochromatic signal fields, when both of them are present simultaneously, is then measured using a CCD camera. We observe a spatial interference pattern form in the overlapped region of the two Gaussian-profile signal fields. The concentric regions of dark- and bright-fringes can be described by the transverse coordinate r from the center. This spatial interference

pattern arises due to the non-zero spatial phase-mismatch that was discussed earlier. In order to observe the temporal interference, we scan the time delay τ between the two driving beams $\mathbf{E_2}$ and $\mathbf{E_2'}$. As τ is scanned, we observe the spatial interference pattern evolve. The measured three-dimensional spatial-temporal interferogram is shown in Fig. 4(a). Note that the dark and bright fringes along the radial coordinate evolve periodically as the temporal coordinate is scanned. The corresponding theoretical simulation is shown in Fig 4(b). The parameters used for the simulation are temporal frequency 2.427 fs^{-1} and spatial frequency 1.9 mm^{-1}. In Fig. 4(c), we show a two-dimensional cross-section taken at a fixed radial position r = 0. This figure shows the temporal evolution of the fringes, and the measured oscillation period is 2.588 fs. In Fig. 4(d), we show a two-dimensional cross-section taken at a fixed temporal instance $\tau = 0$. This shows the spatial variation of the intensity, corresponding to an oscillation with spatial period of 3.3 mm.

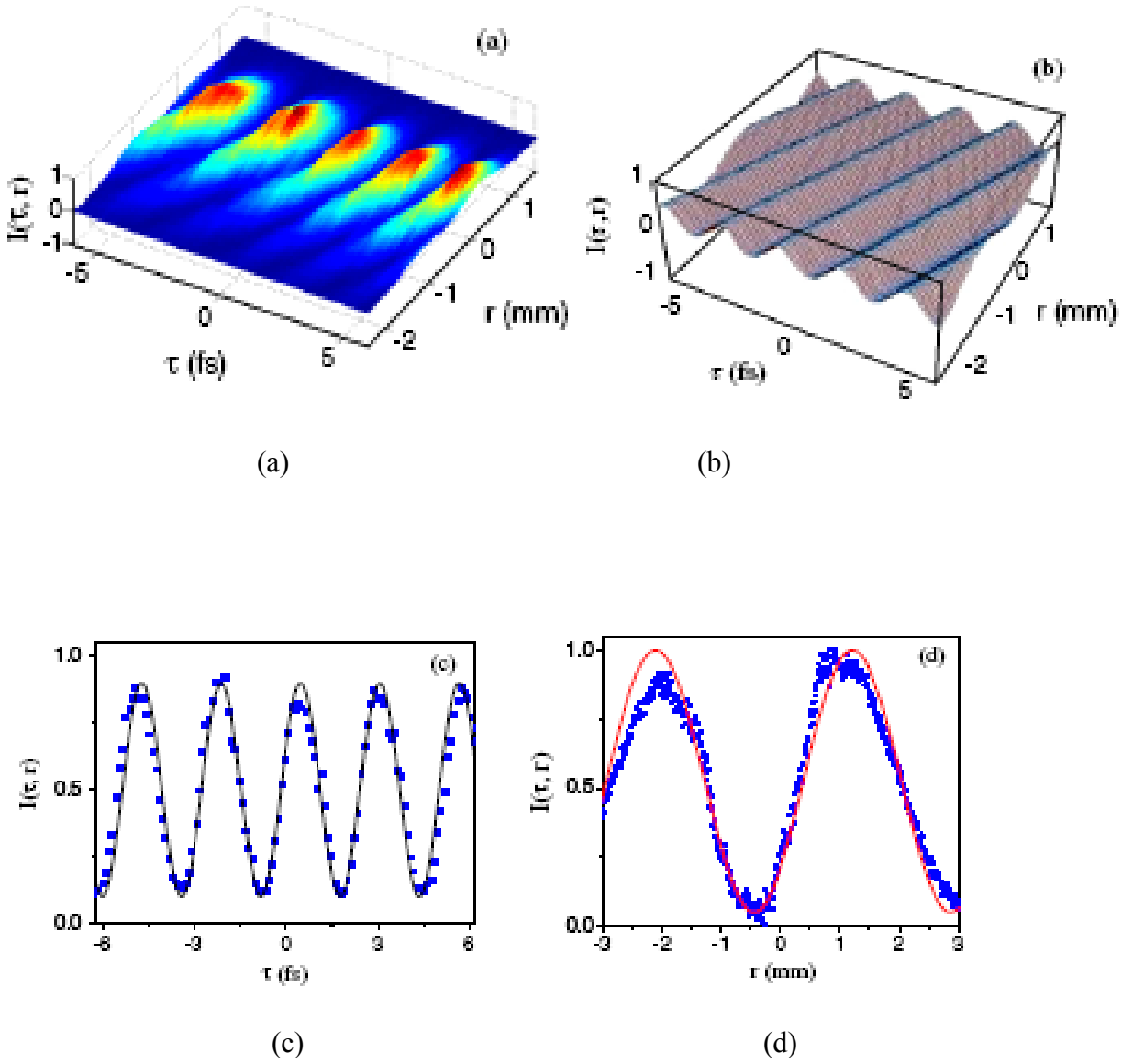

(a) (b)

(c) (d)

Fig. 4. (a) Experimentally measured and (b) theoretically simulated three-dimensional spatial-temporal interferograms for the overlapped FWM and SWM signals. Two-dimensional cross-section showing (c) temporal evolution of the intensity, measured at r=0 (d) radial evolution of the intensity, measured at τ=0. The square dots are measured points, and the solid curves are theoretical fits.

V.3.B. Measurement of transition frequency between $5D_{5/2}$-$5P_{3/2}$ in ^{85}Rb

As discussed earlier, the temporal evolution of the measured interferogram will allow us to measure the resonant frequency for the $5D_{5/2}$-$5P_{3/2}$ transition in ^{85}Rb. To measure this value, data was taken for a much longer temporal-delay duration (50 ps), a section of which is shown in Fig. 5(a). Again, the two-dimensional cross-section in the temporal plane, i.e. at a fixed transverse position of r = 0, is taken (Fig. 5(b)). A fit of these temporal fringes yields a temporal period of 2.588 fs. A Fourier-transformation of the data taken for the entire 50 ps interval is shown in Fig. 5(c), from which the fringe modulation frequency is determined to be 2.427 ± 0.004 fs^{-1}. This corresponds to the resonant frequency for the $5D_{5/2}$-$5P_{3/2}$ transition in ^{85}Rb, which we have measured using the interference between coexisting FWM and SWM signals, each of which involves the measured transition within their multi-transition pathways. We remind that in generating the observed interference signals, we have used driving beams coming from three different laser sources. These results clearly demonstrate the underlying atomic coherence responsible for each multi-wave mixing process, as well as the phase-coherence between two wave-mixing processes arising from different orders of the nonlinear polarization.

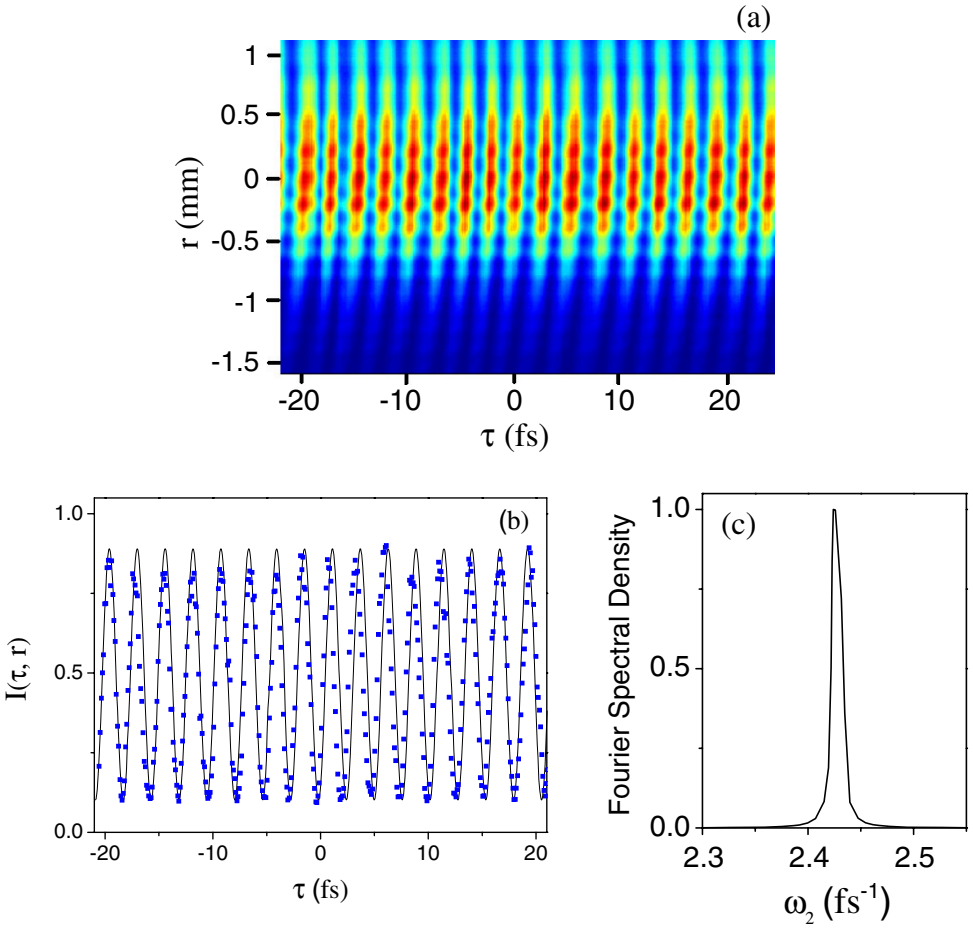

Fig. 5. Spatial-temporal interferogram measured for a much longer temporal duration (50 ps). (a) A small segment of the three-dimensional measurement, and (b) the corresponding two-dimensional cross-section in the temporal plane. (b) Fourier spectrum of the beat signal measured for the entire 50 ps duration.

V.4. Conclusion

Coexisting FWM and SWM pathways were driven in a four-level atomic system. A method to tune the relative directions, amplitudes and phases between the two radiated signals was described and experimentally demonstrated. When the amplitudes of the two signals were made equal and spatially overlapped, the measurement yielded a spatial interference pattern at a CCD camera. When the time-delay between two of the driving beams was then delayed, a temporal evolution of the interference pattern was observed. The parameters of the complete three-dimensional spatial-temporal interferogram were in close agreement with the values predicted by the values of the wave-vector mismatch between the two signals, as well as the resonant frequency of the atomic transition that was driven by the time-delayed beam pair. In summary, various intriguing features pertaining to phase-control of atomic coherence were demonstrated.

VI. Measurement of two independent phase-shifts using coupled parametric amplifiers

VI.1. Introduction

In most interferometric methods, the phase-difference between one pair of optical fields modulates the intensity of the resultant output field, and the output field contains one phase-difference information. Recently, much attention has been given in utilizing quantum and nonlinear optical processes to enhance various aspects of the measurement of this information, for instance in improving the resolution and precision. However, we find a lack of studies geared towards increasing the information capacity itself.

In this chapter, we utilize atomic nonlinearity to enhance an interferometer's information capacity. More specifically, we encode two independent phase-shifts in the measurable intensity of the interferometer's output field. The phases can be readily resolved simultaneously using a single intensity detector. We have achieved this by coupling the two phase informations to two different continuous-variable parameters in the spectral waveform of the output field. We achieve this by utilizing coexisting nonlinearities in a cloud of alkali atoms to simultaneously perform multiplicative as well as additive mixing of multiple optical fields. Besides being a novel conceptual feat, this added dimensionality of information could potentially improve the channel-capacity in optical communication. The work presented in this chapter is closely related to the results of chapters 4 and 5. In a sense, this work involves a synergy between the spectral phase evolution of chapter 4 and the phase-coherence between coexisting nonlinearities of chapter 5, delivering a novel interferometric feat in the process.

First, a discussion of interferometry, the motivation for the current work, and an overview of the new method are discussed. Next, details of the experimental setup and the theoretical description of the physical system and the predicted results are explained. The experimental observations of the two- phase measurement are presented next. Finally, we summarize the work and discuss the possible applications and outlook.

VI.2. Motivation and overview of the new method

VI.2.A Overview of interferometry

Interferometry has had a very rich history in science, both in fundamental research and practical applications[2,5]. The interference between two optical fields lies at the heart of many applications in metrology, including in the measurement of length. When the wavelengths of the two fields are identical, there are measurement schemes in which the identical wavelengths are static, as well as scanned with time. In the first scheme, the measurement is performed at a single position in frequency space. Changes in the optical path length in one arm will alter the output field intensity. Examples include the traditional Mach-Zehnder and Michelson interferometers, and some state-of-the-art applications using this scheme include the measurement of minute space dilations arising from general relativistic effects[119]. In this scheme, one can measure changes in the relative path length difference between the two arms of the interferometer, but not the absolute path length difference between them.

In the second scheme, which is a variant of the Mach-Zehnder interferometer, the wavelength of the two fields probing the interferometer's arms is scanned in time, and measurement is performed along a spectral line[120]. The reference arm's length is made different

from the test arm's length, so that the phase-difference between the two beams evolves linearly along the spectral range being scanned. As a result, the output intensity of the interferometer will consist of fringes in frequency space. Here, changes in the path length of the test arm will alter the phase of the fringes. In addition to the fringe phase, which measures changes in the relative path length difference between the two arms of the interferometer, the fringe period (i.e. the spectral separation between two fringe maxima) measures the absolute path length difference between these two arms. This scheme has been popularly labeled "absolute distance interferometry" and has been utilized, for instance, in ATLAS, the largest particle detector of the Large Hadron Collider (LHC) project at CERN[120].

In the schemes described above, the optical fields undergo only linear transformations, namely that of propagation along the interferometer's arms, and transmission, reflection and additive mixing at beam splitters, before being measured by an intensity detector. There also exist interferometric schemes that use nonlinearities and multiplicative wave-mixing elements in order to process the field phases. Nonlinear wave-mixing processes such as two-photon absorption[123] and four-wave mixing[122-125] as well as closed-loop atomic interferometers[74-76] have been considered, and features such as the interference between multiple quantum transition amplitudes, squeezing and the parametric amplification within the interferometer have been utilized for enhancing sensitivity, resolution and visibility. Quantum interferometry is an active field of research, and exotic states of light are being tested as interferometric probes[126-128].

All of the schemes described above involve a single-phase measurement; that is, from the output field, one can extract information about changes occurring in the phase difference between one pair of optical fields. To our knowledge, there is no interferometer that can measure more than one phase difference in a single measurement. By a single measurement, we mean a

measurement performed in a single spatial window (i.e. one detector) within a single temporal window (i.e. simultaneously).

VI.2.B. Overview of the current contribution

In this chapter, we demonstrate a novel scheme showing the possibility of two-phase interferometry. The scheme is capable of processing the phase-differences of two independent pairs of optical fields in parallel and encoding them in separate continuous-variable parameters (phase and brightness) of a single output signal field that can be directly decoupled in a single intensity measurement. The key lies in merging ideas from both of the schemes described above; i.e. we shape the output signal's spectral bandwidth into fringes so that the fringe phase measures changes in one interferometer, while the fringe intensity measures changes in a second interferometer. The use of such capacity is twofold. First, it can be used to measure the phase-difference information of multiple interferometers in a single measurement. Second, it can be used to generate signals with increased phase-sensitive information encoded per channel.

In order to encode four optical field phases (i.e. two phase differences) in the intensity of one output field in a readily distinguishable way, we mix the fields in a nonlinear medium capable of effective phase-sensitive parametric amplification. We couple the two field pairs probing the two interferometers to two coexisting and coupled quantum nonlinear pathways in an atomic medium, the details of which will be described in the experimental section below. The individual amplifiers, which act as multiplicative wave mixers, are additively coupled via identical phase-matching so that their relative phase alters the resultant signal intensity even without using an external local oscillator; this relative phase is sensitive to one of the interferometers. The second interferometer causes identical spectral-domain fringes in both of

the amplifier's responses, and its phase shift is measured by a spectral translation of these fringes. Dark-state resonances are included in the parametric amplifiers in order to resonantly enhance the multi-photon transition amplitudes with suppressed losses for both driving and generated fields, as well as to attain low background noise and high resolution. The motivations for embedding dark-state resonances in the nonlinear transitions have already been discussed in the previous chapters of this thesis. We will first describe the experimental scheme and derive the equations, after which we will discuss the observations and results.

VI.3. Experimental setup

Our experimental scheme is shown in Fig. 1. The atomic configuration used for generating the coexisting and phase-matched nonlinearities is the same as the one used in the previous chapter. However, more phase manipulation will be added, several new terms and concepts are introduced, and some notations have been modified to match this work. For these reasons, and for self-consistency of this chapter, we will describe all the essential terms and concepts briefly here, even if they had been introduced in the previous two chapters. As a result, certain parts of this section will be repetitions of the previous two chapters, but these will be necessary since this work is, in a sense, a synergy of those two.

We coherently drive the third- and fifth-order nonlinearities in an inverted-Y energy level configuration in rubidium atomic vapour, which is magnetically shielded and heated to 75° C. The driven nonlinearities are coupled by sharing common atomic transitions and driving beams ($\mathbf{E}_i$, $\mathbf{E}_i'$; i = 1, 2, 3) to radiate four-wave mixing (FWM) and six-wave mixing (SWM) signals in the same phase-matched mode (direction $\mathbf{k}_m$, frequency ω_m). An APD placed in the

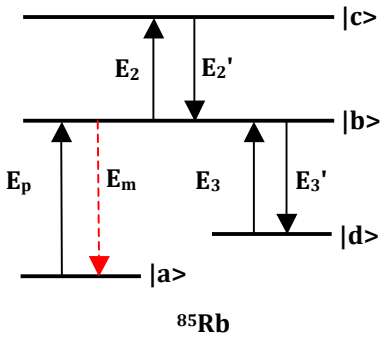

(a) Atomic configuration

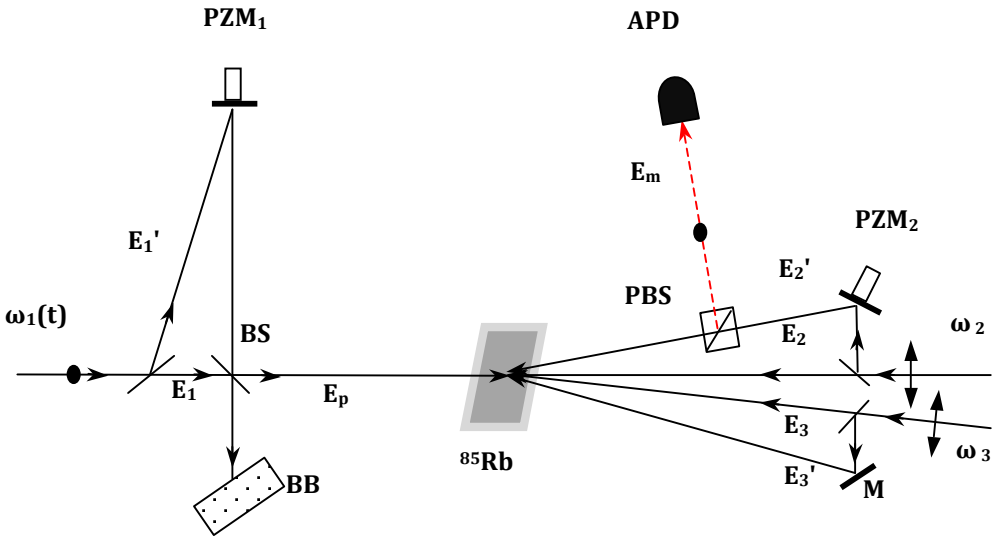

(b) Experimental setup

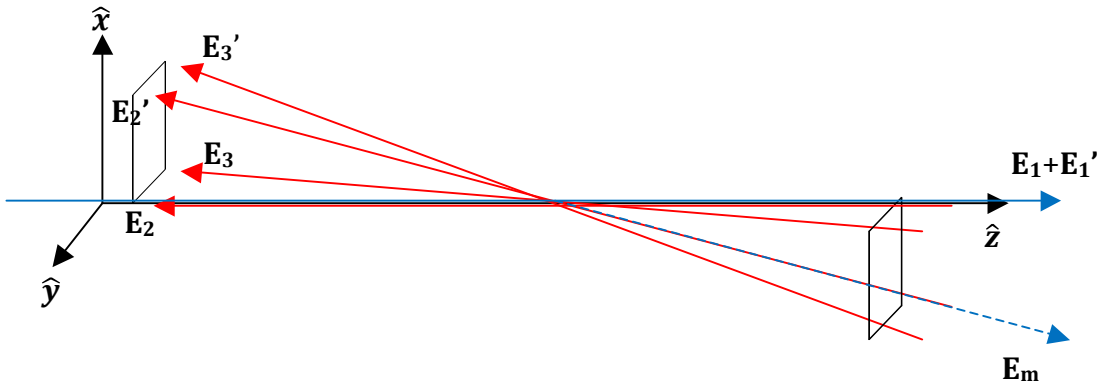

(c) Three-dimensional geometry of beam alignment inside the vapor cell

Figure 1. **Atomic configuration and experimental setup. (a)** Here, |a> and |d> are the hyperfine levels 2 and 3 of the $5S_{1/2}$ ground state, respectively; |b> and |c> correspond to the excited states $5P_{3/2}$ and $5D_{5/2}$, respectively. **(b)** (BS = 50/50 beam splitter, PBS = polarization beam splitter cube, BB = beam block, PZM = piezo-actuated mirror, M = rigid mirror, APD = avalanche photodiode). Here all the beams are shown in the same plane to visually "unfold" the MZ interferometers. **(c)** In the actual setup, $\mathbf{E_2'}$ and $\mathbf{E_3'}$ lie in a plane that crosses the plane containing $\mathbf{E_p}$, $\mathbf{E_2}$ and $\mathbf{E_3}$ inside the rubidium vapour cell. $\mathbf{E_m}$ comprises of all the atom-radiated signal fields that are phase-matched to reach the APD, and counterpropagates with $\mathbf{E_2'}$.

phase-matched direction measures the intensity of the resultant multi-wave-mixing signals. The pair of driving beams $\mathbf{E_i} = A_i e^{-i(\omega_i t - \mathbf{k_i} z + \Phi_i)}$ and $\mathbf{E_i}' = A_i' e^{-i(\omega_i t - \mathbf{k_i}' z + \Phi_i')}$ originate from the same narrow-linewidth continuous wave (cw) laser source LS_i (i =1, 2, 3), and are thus phase-coherent. A_i and A_i' are the field amplitudes. The beam frequencies ω_2 and ω_3 are held fixed at the atomic transition frequencies ω_{cb} and ω_{db}, respectively, while the frequency ω_1 is swept across the Doppler-broadened spectral bandwidth of the ω_{ba} transition with frequency detuning $\Delta\omega_1 = \omega_1 - \omega_{ba}$ (where $\omega_{jk} = (E_k - E_j)/\hbar$ with E_k the energy of the atomic level $|k\rangle$). The weak probe beam $\mathbf{E_p} = \mathbf{E_1} + \mathbf{E_1}'$, travelling along the **z** direction, counter-propagates with the rest of the driving beams at small angles. Beam $\mathbf{E_2}$ travels along the –**z** direction. At any plane transverse to the probe beam's direction, the driving beams pass through the four corners of a square with $\mathbf{E_3}'$ furthest to $\mathbf{E_2}$. Each side of the square subtends an angle of 0.35° at the center of the vapor cell, where all beams intersect. At the intersection region, the powers and diameters of the Gaussian beams $\mathbf{E_1}$, $\mathbf{E_1}'$, $\mathbf{E_2}$, $\mathbf{E_2}'$, $\mathbf{E_3}$, $\mathbf{E_3}'$ are approximately 3 mW, 3 mW, 30 mW, 4 mW, 65 mW, 65 mW and 0.5 mm, 0.6 mm, 1.3 mm, 1.4 mm, 0.7 mm, 0.6 mm, respectively.

As discussed in the previous chapter, the ladder-type EIT coherence enhances the FWM signal $\mathbf{E_f}$ (phase-matching wave-vector $\mathbf{k_f} = \mathbf{k_1} + \mathbf{k_2} - \mathbf{k_2}' \equiv \mathbf{k_m}$ and frequency $\omega_f = \omega_1 + \omega_2 - \omega_2' = \omega_1$) and SWM signal $\mathbf{E_s}$ (phase-matching wave-vector $\mathbf{k_s} = \mathbf{k_1} + \mathbf{k_2} - \mathbf{k_2} + \mathbf{k_3} - \mathbf{k_3}' \equiv \mathbf{k_m}$ and frequency $\omega_s = \omega_1 + \omega_2 - \omega_2 + \omega_3 - \omega_3' = \omega_1$). At the line-center of the Doppler- broadened transition from $|a\rangle$ to $|b\rangle$, due to a large ground-state population, only these EIT-supported signals experience negligible absorption, and all other signal fields have a vanishing transmission. In most of what follows, we limit our treatment to these two signal fields which spectrally coexist at the line center, denoted by $\mathbf{E_c} = \mathbf{E_f} + \mathbf{E_s}$.

Before interacting with the atomic medium, the driving beams are made to probe three Mach-Zehnder interferometers MZ_1, MZ_2, and MZ_3. The optical path length difference ΔL_i between the two arms of MZ_i, and the resulting phase difference $\Delta\Phi_i$, is probed by the pair of beams $\mathbf{E_i}$, $\mathbf{E_i'}$ (i = 1, 2, 3). ΔL_3 is held fixed, whereas $\Delta\Phi_1$ and $\Delta\Phi_2$ are the variables to be measured, or alternately, the parameters that can be controllably designed to phase-modulate the phase-matched signals resulting in $\mathbf{E_c}$. Here, we discuss the measurement process.

In order to measure the two phases $\Delta\Phi_1$ and $\Delta\Phi_2$ in a single spatial-temporal reading of the signal field's intensity $|\mathbf{E_c}|^2$, we decouple the effects of the two phases to two different continuous-variable (CV) parameters in the spectral waveform of the measurable signal intensity: the phase and amplitude of the intensity fringes, respectively. The fringes are generated in the spectral domain by modifying MZ_1 into a frequency-swept interferometer with unbalanced arms. The resultant probe beam then becomes

$$\mathbf{E_p} = \frac{\mathbf{E_1}+\mathbf{E_1'}}{\sqrt{2}} = \frac{A_1}{\sqrt{2}} e^{-i(\omega_1 t - \mathbf{k_1} z)}\left[1 + e^{-i\Delta\Phi_1(\omega_1, \Delta L_1)}\right],$$

where $A_1 = A_1'$ are the field amplitudes and

$$\Delta\Phi_1(\omega_1, \Delta L_1) = \Gamma^{-1}\omega_1 + k_1 \Delta L_1.$$

We have defined Γ (2πHz) = c ΔL_1^{-1} to be the spectral period in which $\Delta\Phi_1$ evolves by 2π. For a fixed but finite Γ, this setup causes the phase difference $\Delta\Phi_1$ to evolve linearly in the spectral domain as the probe beam frequency ω_1 is swept across the atomic resonance linewidth. When

$\Delta L_1 \approx 10^7 \lambda_1$, a small change in the position of the mirror PZ_1 (typically a fraction of λ_1) has a negligible effect on Γ, and basically modulates only the second term of $\Delta\Phi_1(\omega_1, \Delta L_1)$.

As will be shown below, this phase-information encoded in the output of MZ_1 propagates through several orders of quantum nonlinear pathways in the phase-coherently driven medium, and is reproduced in both the FWM and SWM signals amplified by the coupled $\chi^{(3)}$ and $\chi^{(5)}$ processes. First, we focus on the FWM signal field $\boldsymbol{E_f} = \eta_f \chi^{(3)} (\boldsymbol{E_2}')^* \boldsymbol{E_2} \boldsymbol{E_p}$, where the product of the third-order susceptibility was described in the previous chapter. The phase differences in the two interferometers MZ_1 and MZ_2 are encoded in the field envelope of this signal:

$$\boldsymbol{E_f} = A_f \mathrm{e}^{-\mathrm{i}(\omega_f t - k_f z)} \mathrm{e}^{-\mathrm{i}\Delta\Phi_2(\Delta L_2)} \left[1 + e^{-i\Delta\Phi_1(\omega_1, \Delta L_1)}\right],$$

where

$$A_f = \eta_f \chi^{(3)} \frac{A_2' A_2 A_1}{\sqrt{2}}$$

is a real amplitude. Note that we have replaced $(A_2')^*$ by A_2', as the amplitude of the beam is held fixed and does not oscillate, and we also assume no depletion for the strong driving beam. Next, in the SWM channel, which utilizes the same EIT window supporting the FWM process, the field $\mathbf{E_2'}$ is blocked. Instead, the field $\mathbf{E_2}$ is used twice, and the SWM pathway is completed by using $\mathbf{E_3}$ and $\mathbf{E_3'}$ to drive transitions between the energy levels |b> and |d>. The SWM signal field is

$$\boldsymbol{E_s} = \eta_s \chi^{(5)} \boldsymbol{E_3} (\boldsymbol{E_3}')^* (\boldsymbol{E_2})^* \boldsymbol{E_2} \boldsymbol{E_p} = A_s \mathrm{e}^{-\mathrm{i}(\omega_s t - k_s z)} \mathrm{e}^{-\mathrm{i}\Delta\Phi_3(\Delta L_3)} \left[1 + e^{-i\Delta\Phi_1(\omega_1, \Delta L_1)}\right],$$

where

$$A_s = \eta_s \chi^{(5)} \frac{A_3\, A_3'(A_2)^2 A_1}{\sqrt{2}}$$

is a real amplitude. The phase of $\mathbf{E_2}$ has no contribution to the field in this pathway.

VI.4. Two-phase measurement results

VI.4.A. Theoretical derivation and expected results

When $\mathbf{E_f}$ (or $\mathbf{E_s}$) is observed individually, the phase $\Delta\Phi_2(\Delta L_2)$ (or $\Delta\Phi_3(\Delta L_3)$) arising from MZ_2 (or MZ_3) does not have an observable effect on the intensity. However, it is obvious that the phase $\Delta\Phi_1(\Delta L_1, \omega_1)$ arising from MZ_1 will cause identical oscillations in the intensities of the FWM and SWM signals across their spectral bandwidths, even without the use of an additional LO. When the two EIT-coupled spectrally coexisting signals are also phase-matched ($\mathbf{k_f} = \mathbf{k_s} = \mathbf{k_m}$) and polarization-matched, all of which are achieved by our specially-designed beam geometry, they interfere. Since $\mathbf{E_2'}$ contributes only to $\mathbf{E_f}$, we can tune the strength of this driving field to attain identical strengths for $\mathbf{E_f}$ and $\mathbf{E_s}$. The resultant amplified signal field at the line center becomes

$$\mathbf{E_c} = \mathbf{E_f} + \mathbf{E_s}$$

$$= \mathbf{A_c}\left\{ e^{-i\Delta\Phi_2(\Delta L_2)}\left[1 + e^{-i\Delta\Phi_1(\omega_1, \Delta L_1)}\right] + e^{-i\Delta\Phi_3(\Delta L_3)}\left[1 + e^{-i\Delta\Phi_1(\omega_1, \Delta L_1)}\right]\right\},$$

where $\mathbf{A_c}$ is the complex field $\mathbf{A_c} = A_c e^{-i(\omega_1 t - k_m z)}$ with real amplitude $A_c = A_f = A_s$. The path length difference ΔL_3 in MZ_3 is held fixed at $\Delta\Phi_3 = 0$, thereby reducing the signal's dependence to the two variable phases $\Delta\Phi_1$ and $\Delta\Phi_2$. The resulting signal intensity within the EIT-supported spectral bandwidth at the line center would thus be

$$I_c = (I_{c0}/4)\{ 1+ \cos[\Delta\Phi_1(\omega_1, \Delta L_1)]\} \{ 1+ \cos[\Delta\Phi_2(\Delta L_2)]\} \quad (1(a))$$

$$= (I_{c0}/4)\{ 1+ \cos[\Gamma^{-1}\omega_1 + k_1^* \Delta L_1]\} \{ 1+ \cos[k_2^* \Delta L_2]\} \quad (1(b))$$

where I_{c0} is the maximum fringe brightness (amplitude) occurring at $\Delta\Phi_1 = 0$ and $\Delta\Phi_2 = 0$. The linear dependence of $\Delta\Phi_1$ with ω_1 causes intensity fringes across the spectral bandwidth of the signal with spectral period Γ (2π Hz). Any additional phase change in $\Delta\Phi_1$, for instance due to a small shift in PZ_1 or any other phase shifting element placed in MZ_1, will result in a translation of the intensity fringes in the spectral domain spanned by ω_1 (figure 2(a)). The phase change can then be inferred from the spectral displacement, i.e. the spectral-domain phase shift, of the fringes. A change in $\Delta\Phi_2$, on the other hand, would alter the brightness of each fringe without altering their spectral positions (figure 2(b)). Equation 1 thus shows the main result of this work, namely the resolvable coupling of two different phase differences to two different continuous-variable parameters of a single intensity measurement.

For the beam geometry being considered, the Doppler-broadened FWM signal $\mathbf{E_D}$ driven by $\mathbf{E_p}$, $\mathbf{E_3}$ and $\mathbf{E_3'}$ in the lambda-type subsystem also travels along $\mathbf{k_m}$ ($\mathbf{k_D} = \mathbf{k_1} + \mathbf{k_3} - \mathbf{k_3'} \equiv \mathbf{k_m}$). However, since it is not supported by EIT, it is completely absorbed at the line center, and occurs only at the wings of this Doppler-broadened transition. That is, $\mathbf{E_D}$ is spectrally isolated, and does not coexist with $\mathbf{E_c} = \mathbf{E_f} + \mathbf{E_s}$. Since $\mathbf{E_D}$ is proportional to the product $\mathbf{E_3}(\mathbf{E_3'})^* \mathbf{E_p}$, it is also affected by the modulation in $\Delta\Phi_1$. Due to the large spectral bandwidth of this signal, it might be useful to utilize it in conjunction with the EIT-bandwidth-limited signal $\mathbf{E_c}$ for measuring $\Delta\Phi_1$. However, unlike I_c, this signal's intensity I_D does not contain the information of two phases, which is the primary objective of this work.

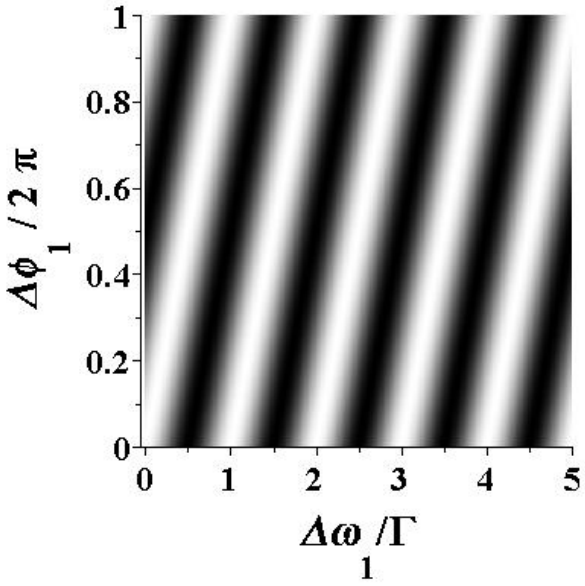

(a)

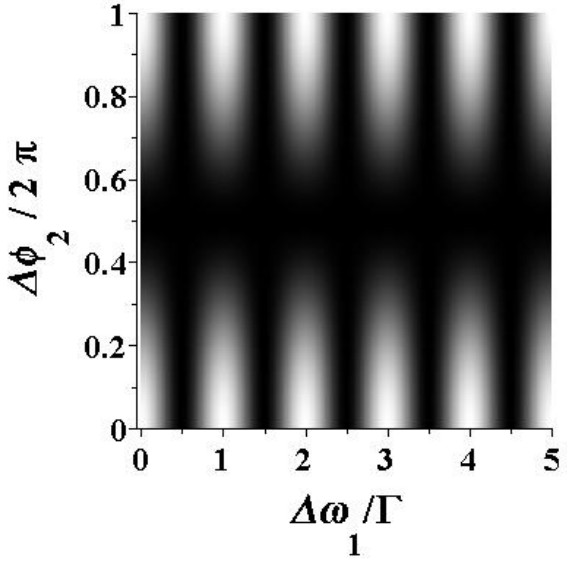

(b)

Figure 2. Theoretical plots for the signal intensity I_c. (a) Three-dimensional space spanned by I_c, $\Delta\omega_1/\Gamma$ and $\Delta\Phi_1/2\pi$ with $\Delta\Phi_2$ held fixed **(b)** Three-dimensional space spanned by I_c, $\Delta\omega_1/\Gamma$ and $\Delta\Phi_2/2\pi$ with $\Delta\Phi_1$ held fixed. In the

grayscale intensity representation of I_c, white = bright fringe and black = dark fringe. Any phase-difference modulation in the interferometer MZ_1 (MZ_2) is measurable as a phase-shift (amplitude-modulation) of the intensity fringes occurring when frequency is scanned.

VI.4.B Experimental observations

Figures 3 and 4 show the photocurrents measured by the APD for various frequency detunings and phases, when $\Delta L_1 = 7.84$ m ($\Gamma = 2\pi$ x 38 MHz). In figure 3((i)), the left box corresponds to the spectral bandwidth supported by the ladder-type EIT coherence, and shows the resultant intensity of the coexisting Doppler-free signals, I_c. In this spectral bandwidth, occurring at the line-center of the $|a\rangle \rightarrow |b\rangle$ transition, the other signals that are not EIT-supported vanish. The right box corresponds to the spectral region towards the blue-detuned wing of the Doppler-broadened transition, where the spectrally broad FWM signal $\mathbf{E_D}$ becomes measurable due to reduced absorption. The phase modulation in MZ_1 is evident in all cases. By keeping all other experimental parameters identical but shifting PZ_1 to alter ΔL_1 by $\lambda_1/2$, creating a π phase-shift between the MZ_1 beams, we observe a spectral translation of the fringes by $\Gamma/2$ (figure 3(ii)), while the amplitude of the peaks and envelope remain fixed. When $\Delta\Phi_2$ is altered, the spectral positions of the intensity fringes remain unchanged. However, in the spectral region containing the two coexisting signals, $\Delta\Phi_2$ modulates the amplitude of the fringes. Figure 4 shows I_c for three different values of PZ_2, corresponding to variations in the MZ_2's phase $\Delta\Phi_2$.

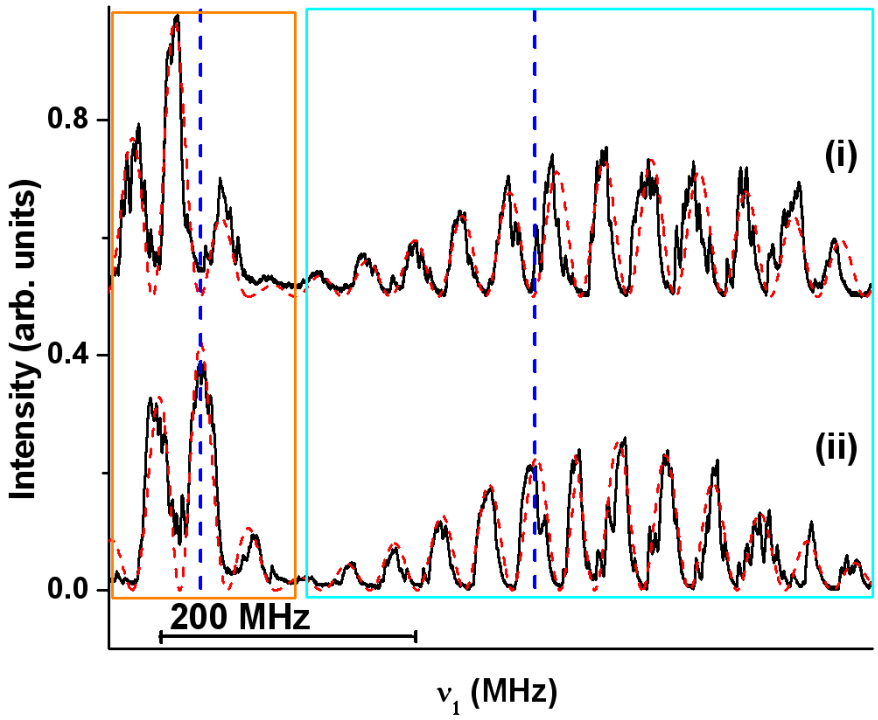

Figure 3. Observations for a varying $\Delta\Phi_1$. Experimental traces (black, solid) and theoretical fits (red, dashed) of the parametrically amplified signals. The left and right boxes highlight the spectral regions that amplify $\mathbf{E_c}$ and $\mathbf{E_D}$ (corresponding to the center and the blue-detuned regions of the Doppler-broadened D2 transition), respectively. When $\Delta\Phi_1$ is increased by π, the fringes in the upper trace **(i)** spectrally translate by $\Gamma/2$ in the lower trace **(ii)**. The two blue vertical dashed lines are guides to the eyes for two spectrally fixed positions. All other parameters, including $\Delta\Phi_2$, are held fixed.

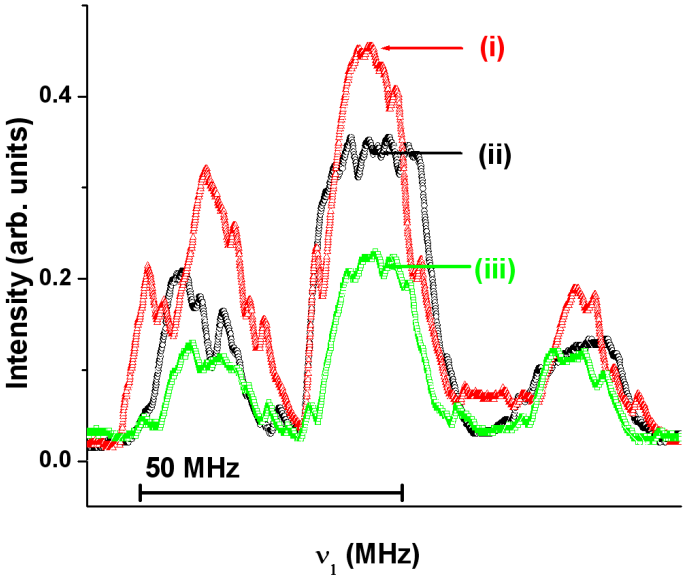

(a)

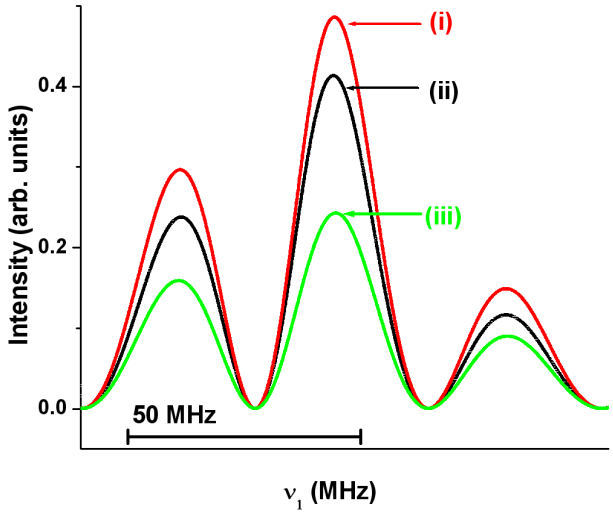

(b)

Figure 4. Observations for a varying $\Delta\Phi_2$. Experimental traces **(a)** and theoretical plots **(b)**, showing I_c for three different values of $\Delta\Phi_2$: (i) 0 (ii) $\pi/3$ (iii) $\pi/2$. All other parameters, including $\Delta\Phi_1$, are held fixed. Here, it is the brightness of the fringes that changes. The spectral region corresponds to the left box shown in Fig. 3.

VI.5. Conclusions and outlook

In conclusion, we have demonstrated a scheme for measuring the phase differences in two different Mach-Zehnder interferometers MZ_1 and MZ_2 in a single measurement of the signal intensity. The key lies in using a spectrally broad measurement in order to have two continuous-variable observables in the intensity: the phase and the brightness of the spectral-domain fringes. The two phases to be measured are then coupled to the two observables, respectively. To our knowledge, this is the first demonstration of identifying relative changes in two pairs of optical path lengths in a single intensity measurement, and might be useful in increasing the spatial dimensions being probed in interferometric measurements, for instance in the Laser Interferometer Gravitational-Wave Observatory (LIGO)[119]. Having phase-sensitive control over two continuous-variable intensity parameters also increases the information capacity per channel[129], which might be useful in optical and quantum communication. In particular, if one set of information is carried by the amplitude of the fringes (via amplitude-modulation), a second set of information can now be simultaneously and separately encoded in the phase of the fringes (via phase-modulation). Another advantage of the scheme is that an external local oscillator (LO) is not needed while measuring the multiple phases. The coexisting fields that are parametrically amplified in the phase-matched mode sufficiently produce the necessary interference and intensity variations at the detector. The lack of need for a LO could make the method valuable in multi-party, long-distance communication of phase-modulated signals.

VII. Phase-dependent spatial fusion of two weak optical fields

VII.1. Introduction

It is well known that two optical fields that are spatially apart can interact with each other in a nonlinear optical medium, and that the interaction can be tuned via the relative phase between the fields[130-138]. This effect has been demonstrated commonly in soliton collision experiments where, depending on the relative phase between the solitons, different outcomes are achieved such as fusion and repulsion. These experimental observations were made in photorefractive crystals as well as atomic vapors, which have different (quadratic and cubic) nonlinearities, respectively. In these experimental demonstrations, the solitons are achieved when the laser beams self-waveguide themselves. The underlying mechanism of self-waveguiding is self-focusing, which is a nonlinear effect arising due to an intensity-dependent refractive index n(I); because of the beam's Gaussian intensity distribution, n(I) causes a lensing effect for the beam as it propagates through the nonlinear medium, thus overcoming the natural tendency of the beam to diverge[139-141]. The conditions for stability of solitons of different dimensions have been extensively investigated[142-143]. The self-induced nonlinearities require the beams to have large intensities, and often high-powered pulses with very narrow temporal and spatial widths are used. In a two-soliton interaction, the interference between the two fields causes the intensity in the region between them to vary with their relative phase difference. For instance for the in-phase case, constructive interference enhances the intensity and the nonlinear refractive index in

this region, thus steering both solitons to this region and resulting in their fusion. Such phase-dependent outcomes for two beams that have an initial spatial separation can be important in constructing all-optical gates and switches, as shown in the schematic in Fig. 1. Recently, theoretical studies have predicted the generation of stable ultra-weak intensity solitons and their collisions in three- and four- level quantized systems[144-151], where the all-optical wave guiding is achieved via quantum coherence effects induced by additional strong coupling beams.

In this chapter, we experimentally demonstrate the phase-dependent interactions between two spatially separate optical fields having very weak intensities. In this case, the underlying mechanism is a waveguide that is induced by quantum coherence effects due to the presence of a strong coupling beam which is initially partially overlapped with both of the weak signal fields. By relying on the cross-Kerr effect, we relax the requirement for the two signal fields themselves to have large intensities. First, we will describe the experimental setup and the mechanism of the coupling-beam-induced waveguide. We will then show that once both the weak signal beams are steered into the waveguide, the resulting interaction between them can be controlled via the relative phase-difference between them. The interaction shown in Fig. 1 is demonstrated between these two weak beams; in addition, we also show that in this system, there are more tunable parameters compared to the scheme that uses two high-powered self-focusing fields.

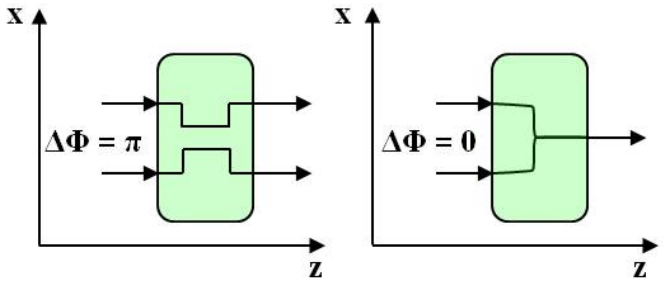

Fig. 1. Schematics of phase-dependent spatial interactions between two optical fields inside a nonlinear optical medium (green shaded region). The two fields propagate along **z**, and have an initial separation along **x**. The output state depends on the relative phase ΔΦ between the two fields.

VII.2. Experimental setup

The experimental setup and the atomic system are shown in Fig. 2. Two weak probe beams $\mathbf{E_1}$ and $\mathbf{E_1'}$ are derived from the same diode laser. The output of the diode laser is first fed into a single-mode polarization maintaining fiber (not shown in figure) for mode-cleaning. The strong coupling beam $\mathbf{E_c}$ is from a Ti:Sa ring laser. All three beams are continuous-wave (cw), nearly collimated, and have Gaussian spatial profiles. Beams $\mathbf{E_1}$ and $\mathbf{E_1'}$ are nearly collinear with a vertical separation between their centroids and negligible overlap. The beam $\mathbf{E_c}$ counterpropagates with $\mathbf{E_1}$ and $\mathbf{E_1'}$, such that $\mathbf{E_c}$'s centroid is in the middle of the centroids of $\mathbf{E_1}$ and $\mathbf{E_1'}$, and $\mathbf{E_c}$ has overlap with both $\mathbf{E_1}$ and $\mathbf{E_1'}$. That is, beams $\mathbf{E_1}$ and $\mathbf{E_1'}$ lie on the opposite sides of counterpropagating beam $\mathbf{E_c}$, and the centroids of the three beams lie in the x-z plane. $\mathbf{E_1}$ and $\mathbf{E_1'}$ are linearly polarized in the plane containing them, while $\mathbf{E_c}$ has a linear polarization

orthogonal to $\mathbf{E_1}$ and $\mathbf{E_1'}$. The strengths of $\mathbf{E_1}$ and $\mathbf{E_1'}$ can be controlled independently by the various half-wave plates and polarization beam-splitters, and together by the neutral density attenuator wheel. One of the mirrors M2 in the path of $\mathbf{E_1'}$ is piezo-actuated, allowing control of the relative phase $\Delta\Phi_1$ between $\mathbf{E_1}$ and $\mathbf{E_1'}$. Another mirror on $\mathbf{E_1'}$ s path (not shown in figure) is placed on a micro-meter translational stage, such that the relative separation between the fields can be easily tuned.

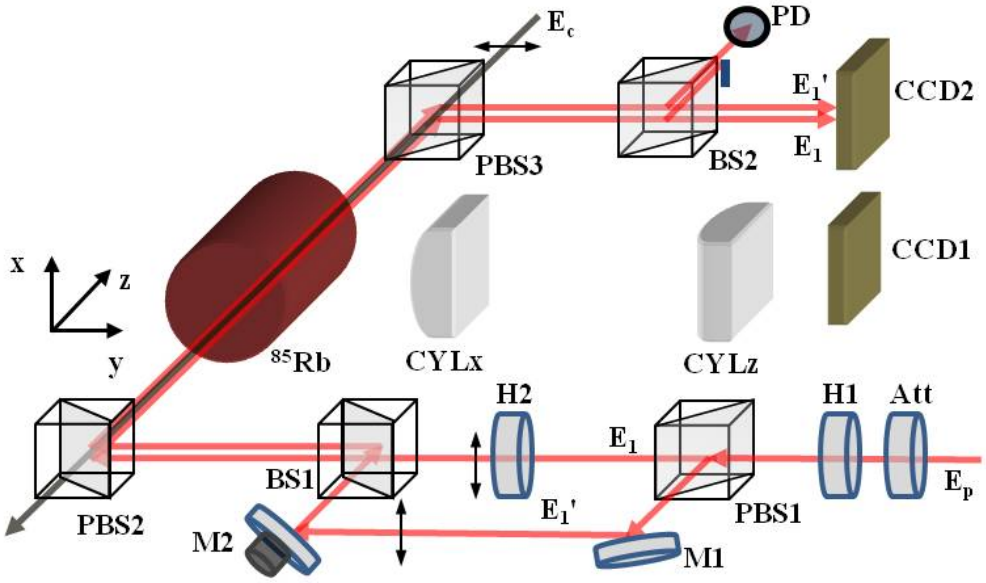

(a)

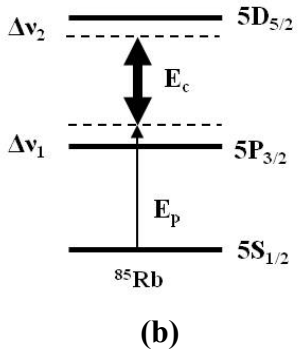

Fig. 2. (a) Experimental setup. Att = variable neutral-density attenuator wheel, (P)BS = (polarizing) beam splitting cube, H = half-wave plate, CYL = cylindrical lens, CCD = charge-coupled device camera, PD = fast photodiode, M = mirror. (b) Atomic system.

Various lenses (not shown in the figure) are used to control the widths and collimations of the fields. The average width of the coupling beam inside the vapor cell is w_c= 156 μm. The widths of the probe beams at the entrance of the vapor cell are w_1 = 133 μm and w_1'=148 μm, and the distance between their centers is 120 μm. When propagating in free space, these beams slowly diverge and by the time they travel 325 mm to the charge coupled device camera CCD2, where they are imaged without using a lens, their widths are w_1 = 670 μm and w_1' = 600 μm. In order to prevent the overlap of these probe beams at CCD2, they are aligned with a small angle between them so that at CCD2, the separation between their centers is larger than their widths (Fig. 3(a) and 4(a)).

The three fields pass through a Rb vapor cell that is heated to 95 °C by a heating coil. The vapor cell is 7.5 cm long, and 3.5 cm of the cell's central portion is accessible for

fluorescence imaging. The fields $\mathbf{E_1}$ and $\mathbf{E_1'}$ are nearly resonant with the D_2 transition (~780.23 nm). They have a frequency detuning of $\Delta\nu_1 = 400$ MHz towards the blue side of the F=3 → F' = 4 transition of ^{85}Rb isotope. The coupling beam E_c is tuned to the transition $5P_{3/2} \rightarrow 5D_{5/2}$ (~775.98 nm), and its frequency detuning $\Delta\nu_2$ can be tuned with a resolution of 10 MHz. The transverse spatial profiles (x-y dimension) of the transmitted probe beams are imaged at CCD2, which is 25 cm away from the Rb cell's exit. Due to the counter-propagating geometry, there is no scattering of the strong coupling beam on the camera. The transmitted field $\mathbf{E_1}$ is also monitored by a photodiode for spectral characterization.

When the camera is placed at position CCD1, it takes images of the x-z dimension of the beams inside the vapor cell via fluorescence from the side of the Rb cell. The fluorescence is imaged onto CCD1 by two cylindrical lenses CYLx and CYLz with focal lengths 10 cm each, which are positioned such that the x- and z- dimensions are magnified by factors of 4 and ¼ at CCD1, respectively. This way, a significant axial length of the beams within the vapor cell (almost 25 mm) can be imaged in a single image while still maintaining a good resolution of the transverse (x) dimension (about 1 mm), at the 7.04 mm x 5.28 mm CCD surface. This circumvents the need to take several axial images and patching them together per image for high resolution. Spherical lenses cannot provide this feature, since they magnify or demagnify both dimensions equally. CYLx, CYLz and CCD1 are each placed in three-dimensional micrometer-precision stages with translational and rotational degrees of freedom to facilitate the imaging process. Furthermore, the beams $\mathbf{E_1}$ and $\mathbf{E_1'}$ are linearly polarized in the x-z plane so as to maximize the dipole-scattered radiation pattern at CCD1.

VII.3. Discussion of the physical mechanism

In the three-level ladder-type atomic medium, a strong coupling beam alters the absorption and dispersion of a weak probe beam via quantum coherence. When both one-photon and two-photon resonances (TPR) are met, the atomic medium is rendered transparent for the probe beam by virtue of EIT. Within the spectral window of EIT, the transmission of the probe beam increases, and it also experiences a rapidly varying refractive index. The value of the refractive index can be controlled by the coupling beam's intensity I_c and the two-photon detuning. The modified absorption and refractive index of the probe beam in this three-level Doppler-broadened atomic medium are given by the imaginary and real parts, respectively, of the complex susceptibility χ shown in Chapter 1.

The dependence of the susceptibility on Ω_c^2 and the Gaussian spatial distribution of I_c, means that the weak probe beam can experience a spatially varying refractive index, which can in turn give rise to lensing and waveguiding behaviors. Such cross-Kerr induced focusing and defocusing for perfectly overlapped probe and coupling beams in the ladder-type configuration with counterpropagating geometry was reported in Ref. 19. The variation of absorption and refractive index as a function of the coupling beam's intensity in and EIT medium have been well characterized before, including in the ladder-type configuration[16, 17, 19].

In our setup the coupling beam $\mathbf{E_c}$, which is on the order of 10^5 more intense than the probe beams, has a rapidly varying spatial profile. The probe beams are placed at the opposite wings of this intensity distribution. When the probe beam is tuned to the blue of the D_2 resonance, a positive (negative) two-photon-detuning results in a positive (negative) value for the refractive index $n(I_c)$. When $\Delta\nu_2$ is positive with a value that is smaller than the power-broadened linewidth of the EIT window, the 400 nW probe beams experience enhanced transmission as

well as a spatially varying refractive index that increases with I_c. The probe beams, initially lying at the edges of the coupling beam, are thus now steered into the center of the all-optical waveguide formed by the optical volume of the coupling beam.

A theoretical description is currently underway. The model will consist of describing dark-state polaritons in a medium having a transversely varying refractive index. We will describe the modifications in the phase-fronts of the dark-state polaritons as they propagate in the spatially dispersive medium. Once the change in the directions of the two polaritons is described by the wave equations, and both of them are steered into a common spatial volume, the resulting fusion will then be allowed due to the bosonic nature of these quasi-particles[23].

VII.4. Experimental results

Once the two weak fields are steered inside this common waveguide, the interaction between them becomes dependent on their relative phase difference $\Delta\Phi_1$. When $\Delta\Phi_1 = 0$, the two fields fuse and the intensity in the central region of the waveguide is maximum (Fig. 3(b)). When $\Delta\Phi_1 = \pi$, the two fields interfere destructively and the central region of the waveguide remains dark (Fig. 3(c)). This is equivalent to the interaction of Fig. 1, which was previously experimentally demonstrated between two strong self-guided beams, and now demonstrated between two ultra-weak beams using quantum coherence. Furthermore, the output state in the current case has more tunability. For the in-phase fusion case (Fig. 3(b)), the output intensity of the central bright component can be all-optically tuned via the intensity of the coupling beam (Fig. 3(d)). This is because in this system we not only modify the refractive index, but the transparency of the medium itself. In the previous demonstrations of two-beam fusion using self-induced nonlinearities, the output intensity cannot be tuned since the fusion is critically dependent not

only on the relative phase, but also on the signal beam intensities themselves which cannot be reduced otherwise the self-induced nonlinearity will disappear. One-dimensional cross-sections of the transverse images are presented in Fig. 4. The asymmetry in the out-of-phase case is mostly due to small imperfections in beam alignment and collimation.

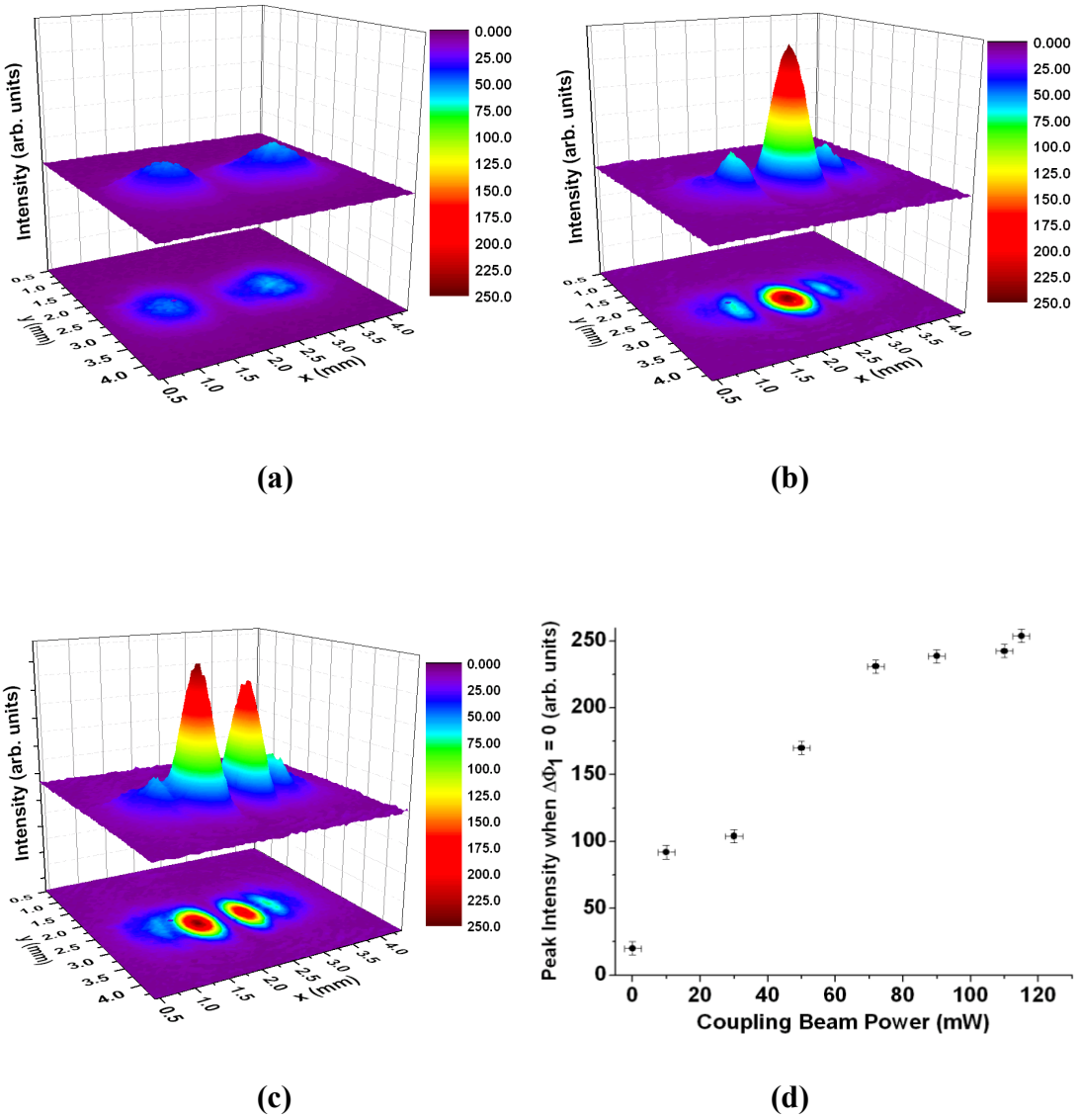

Fig. 3. Two-dimensional transverse images taken by CCD2 when two-photon detuning is nearly resonant. Cell temperature = 95 °C, $\Delta\nu_1$ = +300 MHz, $\Delta\nu_2$ = +10 MHz. Beam powers are

measured before Rb cell. $P_1 = P_1' = 400$ nW. (a) $P_2 = 0$ mW, (b) $P_2 = 115$ mW, $\Delta\Phi_1 = 0$, (c) $P_2 = 115$ mW, $\Delta\Phi_1 = \pi$, (d) Peak intensity of the central fused component when $\Delta\Phi_1 = 0$ (conditions similar to Fig. 3 (b)) as a function of the coupling beam's power P_2.

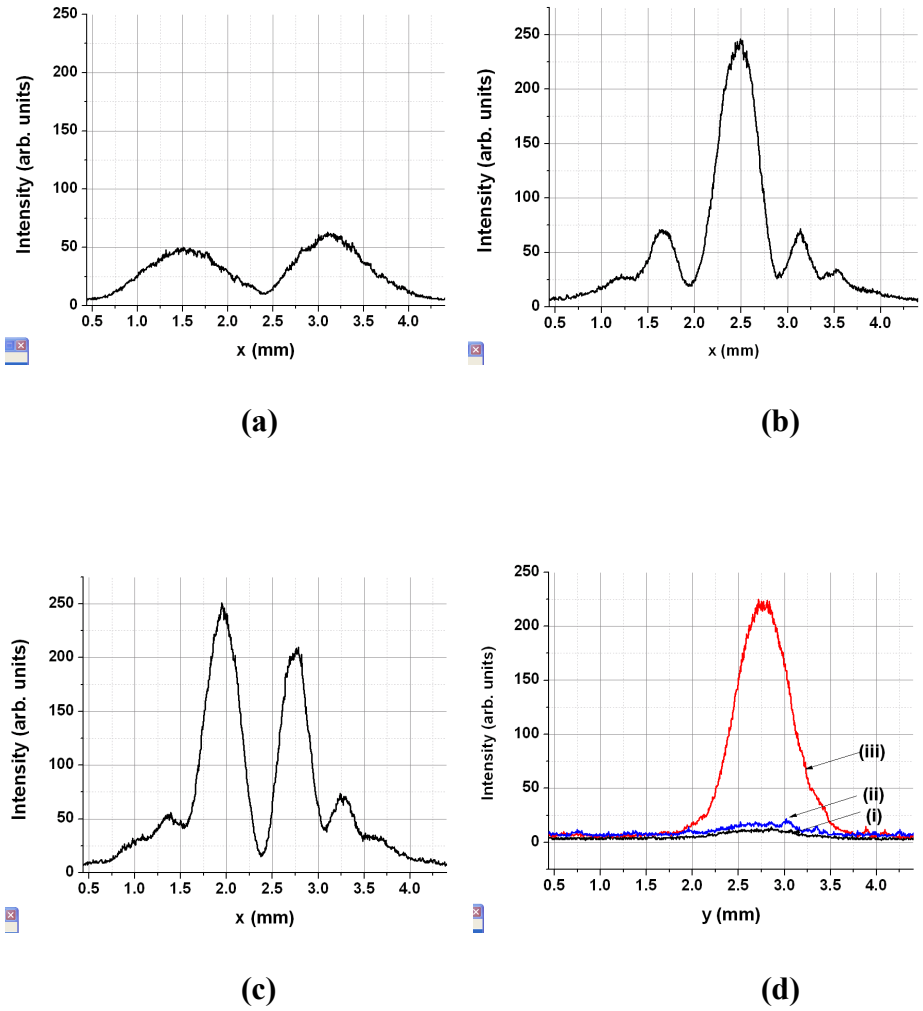

Fig. 4. (a), (b) and (c) are the one-dimensional cross-sections taken along **x** for a fixed value **y** = 2.75mm from the 2-D images shown in Fig. 3 (a), (b) and (c) respectively. In (d), (i), (ii) and (iii) are the one-dimensional cross-sections taken along **y** for a fixed value **x** = 2.38 mm from the 2-D images shown in Fig. 3 (a), (c) and (b) respectively.

Another novel feature of this system is that for the out-of-phase case, the two signal beams do not spatially deflect away; instead, due to the attractive central potential induced by the coupling beam, both beams are guided tightly to the central axis, while the axis itself remains dark due to destructive interference. This opens the room for generating dark vortices with enhanced depth. This feature is possible because in this system, the strength of the attraction is controlled externally by the frequency detuning and intensity of the coupling beam, and not by the intensities of the signal fields themselves.

For large two-photon detunings ($\Delta\nu_2 = \pm$ 250 MHz) the effects of EIT disappear and the transmission of the resonant probe beams through the vapor cell decreases sharply. In this case, we imaged the incoherent fluorescence signal through one side of the vapor cell. In order to increase fluorescence signal for imaging, the probe beam's powers were increased to 400 μW each. Even in these large-detuned cases, the spatially varying refractive index due to I_c presents itself as an attractive or a repulsive potential acting on the weak probe fields. The paths of the two resonant probe beams in the absence of the coupling beam are shown in the image taken by CCD1 in Fig. 5 (a). The beams look overlapped because in the region between, the intensities due to the fluorescence caused by each beam add up. Note the different scales of the x- and z-dimensions. For a positive (negative) $\Delta\nu_1$, we observe that a positive (negative) $\Delta\nu_2$ pulls both probe beams towards the wave-guide center (Fig. 5b) while a negative (positive) $\Delta\nu_2$ pushes the weak beams further apart (Fig. 5c). Transverse cross-sections of each image at a fixed longitudinal position are shown in Fig. 5d. While the enhancement and decrease of the resultant intensity in the central axis is apparent from these images and traces, the contrast is degraded due to the large frequency detuning and thus weaker atomic coherence, and also due to background scattering by the windows of the vapor cell. On the other hand, this noise would have been

overwhelming had we used the lambda-type atomic configuration, since in this case the strong coupling beam also has access to the ground state atoms and causes single resonance fluorescence. One of the main motivations for using the ladder-type scheme is that the strong

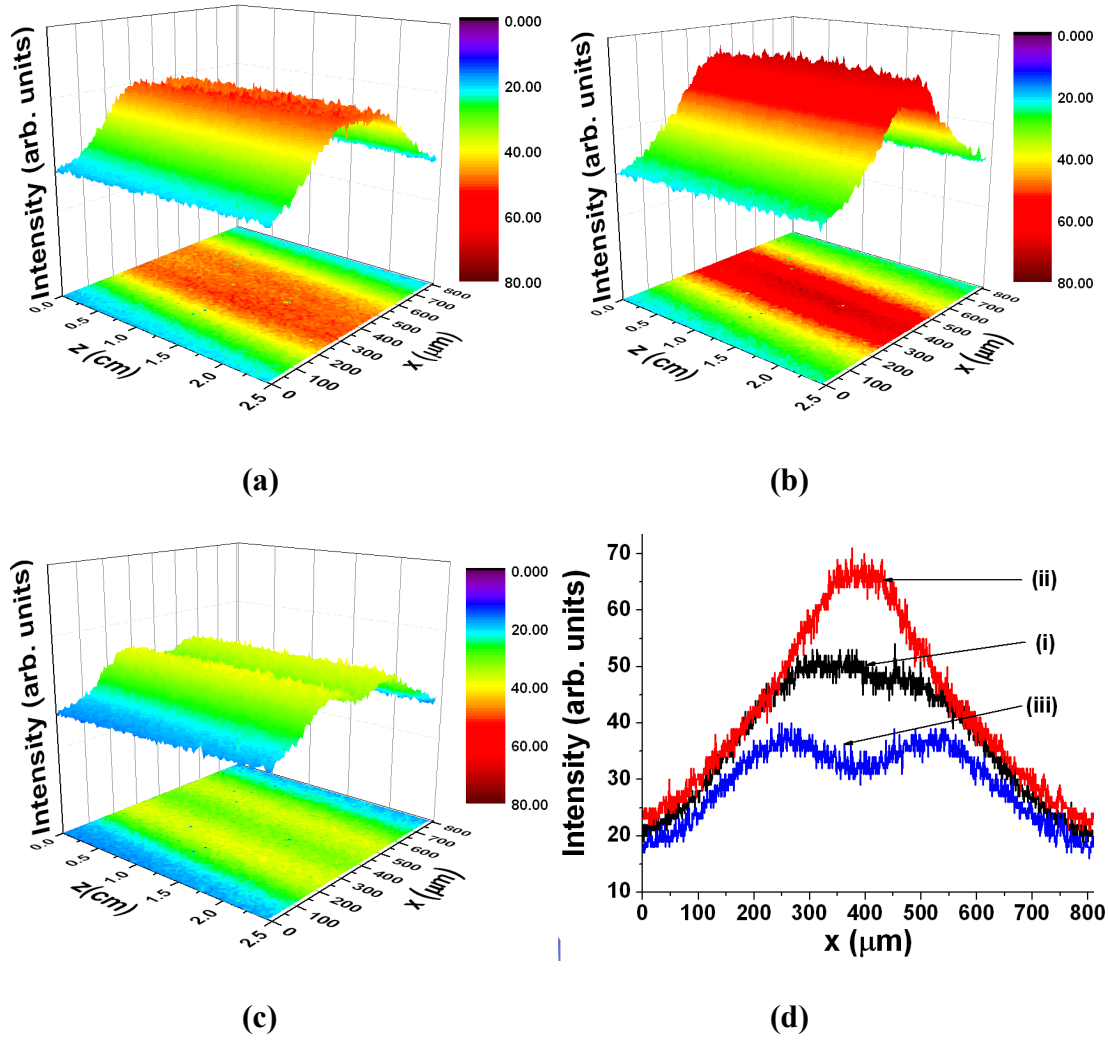

Fig. 5. Longitudinal images taken by CCD1 when two-photon detuning is off-resonant. Cell temperature = 95 °C, $\Delta\nu_1$ = +400 MHz. Beam powers are measured before Rb cell. P1 = P1' = 400 μW. Note the different scaling of the axes: **x** is in μm but **z** is in cm, achieved by the specially designed imaging. (a) P_2 = 0 mW, (b) P_2 = 90 mW, $\Delta\nu_2$ = + 250 MHz, attractive (c) P_2 = 90 mW, $\Delta\nu_2$ = - 250 MHz, repulsive. In (d), (i), (ii) and (iii) are the one-dimensional cross-

sections taken along **x** (at **z** = 2.35 cm) from the 2-D images shown in (a), (b) and (c) respectively.

coupling beam drives the transition between two excited states which have no atomic population in equilibrium, and thus does not contribute to fluorescence unless the probe beam is present. As a result, the measurable image signal-to-noise ratio is much higher in this atomic configuration.

VII.5. Conclusions and outlook

We have thus utilized quantum coherence induced by a strong coupling beam in a three-level atomic system to observe spatial interactions between two ultra-weak beams, for resonance as well as off-resonance of the two-photon frequency detuning. In the on-resonance case, the enhanced transmission due to EIT allowed us to measure the transverse profile of the interacting probe beams in the far-field, in which case we observed phase-dependent interactions akin to soliton fusion and repulsion. In the off-resonance case, where incoherent scattering is large, we observed side-ways fluorescence images and observed the dependence of the interaction between the two weak beams depending on the TPR frequency detuning. We have shown that this system has a large set of tunable parameters (single-photon and two-photon frequency detunings, coupling beam's power, relative phase between the probe beams), and that it allows all-optical switching and routing of ultra-weak beams, as well as interaction between them. Furthermore, since EIT is a natural test bed for slow light as well as stored light[22-30], it will be useful to extend this system to study quantum memory and quantum logic gates involving two ultra-weak fields having phase-dependent spatial interactions.

VIII. Conclusions and outlooks

In this thesis, we have described various studies in which atomic coherence was used to enhance nonlinear optical processes. A wide parameter space traversing the spatial, temporal and spectral domains was investigated. In each case, attention was paid to phenomena that are sensitive to the phases in the driven atomic coherences, and methods were developed to use all-optical phase-control to manipulate the nonlinear atomic response and, alternately, to use the nonlinear atomic response to measure the phases in the driving optical fields.

In chapter 1, we provided a basic introduction to the concepts necessary for understanding atomic coherence enhanced nonlinear optical processes in multi-level atoms. We described two-, three- and four-level atomic systems and some important features such as dark-states and EIT that enhance nonlinear-optical wave-mixing processes by allowing dissipation-free resonant transitions. We discussed FWM and SWM processes facilitated by EIT, and then introduced some phase-sensitive results that will be discussed in the rest of the chapters.

In chapter 2, we described experimental observations of multiple EIT spectral windows in a ladder-type atomic system that became resolvable when the probe beam was elliptically polarized. The multiple peaks arise because the uppermost excited state is comprised of several hf levels that are closely lying in energy. Furthermore, the multiple transparency peaks switched when the phase in the elliptically polarized beam was varied. To account for this phase-sensitive switching phenomenon, we developed a theoretical model treating the interference between dark-states in a four-level sub-system. The theoretical results were in qualitative agreement with the

experimental observations. Various possible applications exist for such phase-sensitive switching of multiple transparency window across frequency, such as AND and OR logic gates.

In the work described in chapter 3, a coherent FWM transition was driven in a ladder-type configuration, such that the initial vacuum mode between the upper excited states was parametrically amplified giving rise to the measured FWM radiation signal at that transition frequency. Here again, the FWM signal consisted of spectrally asymmetric multiple peaks. We experimentally characterized this radiation by varying many parameters, and identified the underlying causes for each spectral feature. Unlike FWM radiation driven between the ground state and the first excited state, this FWM system showed more complex one-photon and two-photon decay channels, making it an interestingly mixed system. These spectrally varying decay channels, along with the diverse multiplicities of the participating energy levels and the associated transition strengths, were studied in order to understand FWM between the 5D and 5P fine structures, and also to find the optimum conditions for using this system for practical applications.

The atomic parameters govern the spectral waveform of the generated FWM signal, often imparting spectral asymmetries. In chapter 4, we developed an all-optical interferometric method to gain external control over the spectral waveform of the coherent FWM signal. The key lies in modulating the relative phase between the two frequency-swept driving beams as their frequency is scanned. In the closed atomic contour being driven, this spectral phase evolution is then propagated to the optical phase of the parametrically amplified signal. By controlling the rate of the spectral phase evolution and the frequency detunings, we demonstrated some waveform-control applications such as linewidth narrowing, line shape symmetrization and all-optical bandwidth switching. The important feature of this method is that drastic changes in the signal

waveform can be achieved without altering beam powers, beam directions, or atomic densities. Instead, only a phase-shift between the driving beams is enough, making the process desirable for situations demanding thermodynamic adiabaticity. In chemical reactions involving several multi-photon transitions in close spectral proximity, the phase-controlled waveform shaping methods could also be useful in selectively switching transitions on and off (bandwidth switching example), or tuning the relative transition strengths between the various transitions (line shape symmetrization example). Moreover, the relative phase at optical frequencies can be controlled with a greater precision and resolution than other parameters, and it is gratifying that the system response is very sensitive to this highly controllable parameter. Finally, while we have discussed controlling the signal waveform by precision control of the input relative phase, the converse process will also be useful for interferometric applications. That is, if one of the driving beams has passed through an unknown phase-varying element, the FWM signal phase yields a measurement of the unknown phase. In light of the fact that FWM processes are ideal for quadrature-noise squeezing, this process deserves further study in measuring interferometric phase-shifts beyond the shot-noise limit. Also, testing the quantum correlation between different spectral mode pairs (spectral-domain fringes) of the amplified fields would augment the studies where correlations between spatial mode pairs have been demonstrated[54-56].

In chapter 5, we described an experiment in which two coexisting MWM transitions were driven simultaneously in the same atomic cloud. One transition was a FWM process, while the other transition was a SWM process. We demonstrated techniques to control: the relative strengths between these two coexisting processes such that they could be made of equal magnitudes; the directions between the two amplified signal fields so as to overlap them in the same spatial mode; and the relative phase between them so that their phase coherence could be

measured. By precision control of the time-delay between two frequency-degenerate driving fields, the relative phase between the FWM and SWM signals was varied and the resulting temporal beat signal monitored. In this way, the resonant frequency of the atomic transition that was driven by the time-delayed fields, i.e. the $5D_{5/2}$ - $5P_{3/2}$ transition in ^{85}Rb, which is in the femtosecond time scale, was measured. The high contrast of the interference signals demonstrated the phase-coherence between these two coexisting $\chi^{(3)}$ and $\chi^{(5)}$ processes. Besides high-resolution spectroscopy of optical transitions, such amplitude- and phase-tunability between processes of different nonlinear orders will also be important in various avenues, in particular in the study of generating high-dimensional stable solitons. The ability to coherently control four- and six- photon transitions and selectively tune their nonlinear transition amplitudes will also be important in the coherent control of chemical reactions.

The work described in chapter 6 dealt with increasing the interferometric capacity of an interferometer. In this method, the output of the interferometer has a spectral bandwidth with a spectrally evolving phase. This spectral phase is sensitive to one Mach-Zehnder interferometer, while the intensity of the signal envelope is sensitive to a second Mach-Zehnder interferometer. In this way, unlike traditional interferometers that can measure the phase difference between one pair of optical fields, this interferometer can measure the phase difference between two pairs of optical fields in parallel. The underlying mechanism involves coherently mixing all the optical fields probing the various arms of the interferometers in one atomic cloud, which then processes the various phases and encodes them in the resulting atom-radiated signal field. The method is a synergy of the spectral-phase-evolution method of chapter 4 and the coexisting and coherent parametric amplifiers of chapter 5.

This enhanced phase-processing dimensionality could be useful in various future applications. It could be useful when one has to measure space dilations in two orthogonal spatial planes synchronously, for instance to measure complex gravitational waveforms. The advantage of using this interferometer as opposed to using two independent orthogonal Mach-Zehnder interferometers is that the latter scheme will require an intermediary clock to synchronize the two phase measurements, which can itself be affected by the unknown space-time dilations being measured, thus contributing to systematic errors. In our two-phase measurement scheme, on the other hand, the two phases are coupled in the same output optical field simultaneously by the atomic nonlinearity and no post-processing temporal synchronization is necessary. Besides being useful for measuring unknown phase-shifts, this system can also be useful for optical communication in generating optical signals with enhanced information capacity. In particular, by precisely controlling the phases of all the driving beams, we can simultaneously encode two sets of information in the coherent atom-radiated signal, one of which can be amplitude-modulated and the other phase-modulated.

In the experiment described in chapter 7, we explored the possibility of phase-sensitive fusion and repulsion between two optical beams at ultralow intensities. Such studies have been important in soliton collisions, which are typically driven at high intensities, and recently much theoretical interest has been given to observing such collisions between weak optical fields by utilizing atomic coherence. Our experiment's motivation was to observe these interesting features. By steering two weak optical fields towards each other by using atomic coherence due to a common strong coupling beam, we were able to observe different phase-dependent spatial outcomes between the weak optical fields. When the two fields were in phase, they fused and enhanced the intensity in the central spatial mode. When they were out of phase, the central

spatial mode remained dark while the fields propagated close to this mode due to the attractive nature of the induced atomic coherence. Some of the potential applications for this study are all-optical beam-combination of ultra-weak fields, phase-sensitive gates for multi-port beam routing and optical information processing. An immediate and interesting task, which we are currently doing, is to complete the theoretical model of the process being investigated. The model consists of the transversely varying propagation of dark-state polaritons[23], whose bosonic quasi-particle nature allows them to occupy the same spatial mode and fuse.

References

1. M. O. Scully and M. S. Zubairy, Quantum Optics (Cambridge Univ. Press, 1997).
2. L. Mandel and E. Wolf, Optical Coherence and Quantum Optics (Cambridge Univ. Press, 1995).
3. N. Bloembergen, Nonlinear Optics (World Scientific Publishing, Singapore, 1996).
4. R. Boyd, Nonlinear Optics (Academic Press, New York, 1992).
5. P. Hariharan, Optical Interferometry (Academic Press, San Diego, CA, 1985).
6. J. A. Armstrong, N. Bloembergen, J. Ducuing, and P. S. Pershan, Phys. Rev. **127**, 1918 (1962).
7. N. Bloembergen and Y. R. Shen, Phys. Rev. **133**, A37 (1964).
8. P. D. Maker and R. W. Terhune, Phys. Rev. 137, A801 (1965).
9. J-L. Oudar and Y. R. Shen, Phys. Rev. A **22**, 1141 (1980).
10. T.W. Hänsch and P. Toschek, Z. Physik **236**, 213 (1970).
11. K. –J. Boller, A. Imamoglu, and S. E. Harris, Phys. Rev. Lett. **66**, 2593 (1991).
12. S. E. Harris, Phys. Today **50**, 36–42 (1997).
13. E. Arimondo in Progress in Optics (ed. Wolf, E.) 257–354 (Elsevier Science, Amsterdam, 1996).
14. J.P. Marangos, J. Mod. Opt. **45**, 471 (1998).
15. M. Fleischhauer, A. Imamoglu, and J.P. Marangos, Rev. Mod. Phys. **77**, 633 (2005).
16. M. Xiao, Y.-Q. Li, S.-Z. Jin, and J. Gea-Banacloche, Phys. Rev. Lett. **74**, 666 (1995).
17. J. Gea-Banacloche, Y.-Q. Li, S.-Z. Jin, and M. Xiao, Phys. Rev. A **51**, 576 (1995).
18. S. Jin, Y. Li, and M. Xiao, Opt. Comm. **119**, 90 (1995).
19. R. R. Moseley, S. Shepherd, D. J. Fulton, B. D. Sinclair, and M. H. Dunn, Phys. Rev. Lett. **74**, 670 (1995).

20. R.R. Moseley, S. Shepherd, D.J. Fulton, B.D. Sinclair, and M.H. Dunn, Opt. Comm. **119**, 61 (1995).

21. J. C. Petch, C. H. Keitel, P. L. Knight, and J. P. Marangos, Phys. Rev. A **53**, 543 (1996).

22. L. V. Hau, S. E. Harris, Z. Dutton, and C. H. Behroozi, Nature **397**, 594 (1999).

23. M. Fleischhauer and M. D. Lukin, Phys. Rev. Lett. 84, 5094 (2000).

24. C. Liu, Z. Dutton, C. H. Behroozi, and L.V. Hau, Nature (London) **409**, 490 (2001).

25. D. F. Phillips, A. Fleischhauer, A. Mair, R. L. Walsworth, and M.D. Lukin, Phys. Rev. Lett. **86,** 783 (2001).

26. A. Mair, J. Hager, D. F. Phillips, R. L. Walsworth, and M.D. Lukin, Phys. Rev. A **65**, 031802(R) (2002).

27. X.–L. Song, L. Wang, Z.–H. Kang, R.–Z. Lin, X. Li, Y. Jiang, and J.Y. Gao, Appl. Phys. Lett. **91**, 071106 (2007).

28. R. M. Camacho, C. J. Broadbent, I. A-Khan, and J. C. Howell, Phys. Rev. Lett. **98**, 043902 (2007).

29. L. Zhao, T. Wang, Y. Xiao, and S. F. Yelin, Phys. Rev. A **77**, 041802(R) (2008).

30. G. Hetet, J. J. Longdell, M. J. Sellars, P. K. Lam, and B. C. Buchler, Phys. Rev. Lett. **101**, 203601 (2008).

31. M. Shuker, O. Firstenberg, R. Pugatch, A. Ron, and N. Davidson, Phys. Rev. Lett. **100**, 223601 (2008).

32. R. Zhang, S. R. Garner, and L. V. Hau, Phys. Rev. Lett. **103**, 233602 (2009).

33. O. Firstenberg, P. London, M. Shuker, A. Ron, and N. Davidson, Nature Physics **5**, 665 (2009).

34. U. Khadka, Y. Zhang, and M. Xiao, Phys. Rev. A **81**, 023830 (2010).

35. J. Sheng, X. Yang, U. Khadka, and M. Xiao, Opt. Express **19**, 17059 (2011).

36. S. E. Harris, J. E. Field, and A. Imamoglu, Phys. Rev. Lett. **64**, 1107 (1990).

37. M. Jain, H. Xia, G. Y. Yin, A. J. Merriam, and S. E. Harris, Phys. Rev. Lett. **77**, 4326 (1996).

38. H. Schmidt and A. Imamoglu, Opt. Lett. **21**, 1936 (1996).

39. S. E. Harris and L. V. Hau, Phys. Rev. Lett. **82**, 4611 (1999).

40. M. M. Kash et al., Phys. Rev. Lett. **82**, 5229 (1999).

41. P. R. Hemmer et al., Opt. Lett. **20**, 982 (1995).

42. Y. -Q. Li and M. Xiao, Opt. Lett. **21**, 1064 (1996).

43. B. Lu, W. H. Burkett, and M. Xiao, Opt. Lett. **23**, 804-806 (1998).

44. A. S. Zibrov, M. D. Lukin, and M. O. Scully, Phys. Rev. Lett. **83**, 4049 (1999).

45. M. D. Lukin et al., Phys. Rev. Lett. **82**, 1847 (1999).

46. H. Kang, G. Hernandez, and Y. Zhu, Phys. Rev. A **70**, 061804 (2004).

47. Y. P. Zhang, A. W. Brown, and M. Xiao, Opt. Lett. **32**,1120 (2007).

48. Y. P. Zhang, B. Anderson, A. W. Brown, and M. Xiao, Appl. Phys. Lett. **91**, 061113 (2007).

49. Y. P. Zhang, A. W. Brown, and M. Xiao, Phys. Rev. Lett **99**,123603 (2007).

50. Y. P. Zhang, U. Khadka, B. Anderson, and M. Xiao, Appl. Phys. Lett. **91**, 221108 (2007).

51. Y. P. Zhang, B. Anderson, and M. Xiao, Phys. Rev. A **77**, 061801(R) (2008).

52. P. K. Vudyasetu, R. M. Camacho, and J. C. Howell, Phys. Rev. Lett. **100**, 123903 (2008).

53. J. Wen, S. Du, Y. Zhang, M. Xiao, and M. H. Rubin, Phys. Rev. A. **77**, 033816 (2008)

54. V. Boyer, A. M. Marino, R. C. Pooser, and P. D. Lett,, Science **321**, 544 (2008).

55. V. Boyer, A. M. Marino, and P. D. Lett, Phys. Rev. Lett. **100**, 143601 (2008).

56. A. M. Marino et al., Nature **457,** 859 (2009).

57. R. M. Camacho, P. K. Vudyasetu, and J. C. Howell, Nature Photonics **3**, 103 (2009).

58. Y. P. Zhang, U. Khadka, B. Anderson, and M. Xiao, Phys. Rev. Lett. **102** 013601 (2009).

59. U. Khadka, H. Zheng, and M. Xiao, Phys. Rev. A **84**, 043814 (2011).

60. H. Zheng, U. Khadka, J. Song, Y. Zhang, and M. Xiao, Europhys. Lett. **93**, 23002 (2011).

61. X. Yang, J. Sheng, U. Khadka, and M. Xiao, Phys. Rev. A **83**, 063812 (2011).

62. H. Zheng, U. Khadka, J. Song, Y. Zhang, and M. Xiao, Opt. Lett. **36**, 2584 (2011).

63. X. Yang, J. Sheng, U. Khadka, and M. Xiao, Phys. Rev. A **85**, 103824 (2012).

64. U. Khadka, H. Zheng, and M. Xiao, Opt. Express **20**, 6204 (2012).

65. U. Khadka, J. Sheng, X. Yang, and M. Xiao, New Journal of Physics **14**, 043026 (2012).

66. M.D. Lukin, S.F. Yelin, M. Fleischhauer, and M.O. Scully, Phys. Rev. A **60**, 3225 (1999).

67. B.S. Ham and P.R. Hemmer, Phys. Rev. Lett. **84**, 4080 (2000).

68. M.D. Lukin, Rev. Mod. Phys. **75**, 457 (2003).

69. J. Zhang, G. Hernandez, and Y. Zhu, Opt. Exp. **16**, 19112 (2008).

70. D. V. Kosachiov, B. G. Matisov, and Y. V. Rozhdestvensky, J. Phys. B **25**, 2473 (1992).

71. E. A. Korunsky, N. Leinfellner, A. Huss, S. Baluschev, and L. Windholz, Phs. Rev. A **59**, 2302 (1999).

72. T. A-Salloum, J. P. Davis, C. Lehman, E. Elliott, and F. A. Narducci, J. Mod. Opt. **54**, 2459 (2007).

73. V. A. Sautenkov, H. Li, Y. V. Rostovtsev, G. R. Welch, J. P. Davis, F. A. Narducci, and M. O. Scully, J. Mod. Opt. **56**, 975 (2009).

74. S. J. Buckle, S. M. Barnett, P. L. Knight, M. A. Lauder, and D. T. Pegg, Optica Acta: Int. J. of Opt. **33,** 1129 (1986).

75. G. Morigi, S. F- Arnold and G- L. Oppo, Phys. Rev. A **66,** 053409 (2002).

76. S. Clow and T. Weinacht, Phys. Rev. A **82,** 023411 (2010).

77. C. Chen, Y. Yin, and D. S. Elliott, Phys. Rev. Lett. **64**, 507 (1990).

78. E. Dupont et al., Phys. Rev. Lett. **74**, 3596 (1995).

79. L. Zhu, V. Kleiman, X. Li, S. P. Lu, K. Trentelman, and R. J. Gordon, Science **270**, 77 (1995).

80. K. Ohmori, Y. Sato, E. E. Nikitin, and S. A. Rice, Phys. Rev. Lett. **91**, 243003 (2003).

81. Gunawardena and D. S. Elliott, Phys. Rev. Lett. **98**, 043001 (2007).

82. R. Yamazaki and D. S. Elliott, Phys. Rev. Lett. **98**, 053001 (2007).

83. . Rabitz, R. de Vivie-Riedle, M. Motzkus, and K. Kompa, Science **288**, 824 (2000).

84. S. A. Rice and M. Zhan, Optical Control of Molecular Dynamics (Wiley, New York, 2000).

85. K. J. Kubarych, C. J. Milne, and R. J. D. Miller, Int. Rev. Phys. Chem. **22**, 497 (2003);

86. S. Saito and I. Ohmine, Phys. Rev. Lett. **88**, 207401 (2002);

87. D. J. Ulness, J. C. Kirkwood, and A. C. Albrecht , J. Chem. Phys. **108**, 3897 (1998).

88. T. Udem, R. Holzwarth, and T.W. Hänsch, Nature **416**, 233 (2002).

89. L. Allen and J. Eberly, Optical Resonance and Two-Level Atoms (Dover Books on Physics, 1987).

90. H. Tanji-Suzuki, W. Chen, R. Landig, J. Simon, and V. Vuletić, Science **333**, 1266-1269 (2011).

91. P. A. Franken, A. E. Hill, C. W. Peters, and G. Weinreich, Phys. Rev. Lett. 7, 118 (1961).

92. L. Deng, E. W. Hagley, J. Wen, M. Trippenbach, Y. Band, P. S. Julienne, J. E. Simsarian, K. Helmerson, S. L. Rolston and W. D. Phillips, Nature **398**, 218 (1999).

93. J. M. Vogels, K. Xu, and W. Ketterle, Phys. Rev. Lett. **89**, 020401 (2002).

94. W. RuGway, S. S. Hodgman, R. G. Dall, M. T. Johnsson, and A. G. Truscott, Phys. Rev. Lett. **107**, 075301 (2011).

95. J. Sheng, H. Wu, X. Yang, U. Khadka, and M. Xiao, Opt. Lett., accepted (2012).

96. D. McGloin, M.H. Dunn, and D.J. Fulton, Phys. Rev. A **62**, 053802 (2000).

97. S. Li, B. Wang, X. Yang, Y. Han, H. Wang, M. Xiao, and K. C. Peng, Phys. Rev. A **74**, 033821 (2006).

98. Y. Zhu, S. Wang, N.M. Mulchan, Phys. Rev. A **59**, 4005 (1999).

99. S.F. Yelin, V.A. Sautenkov, M.M. Kash, G.R. Welch, and M.D. Lukin, Phys. Rev. A **68**, 063801 (2003).

100. B. Wang, Y. Han, J. Xiao, X. Yang, C. Xie, H. Wang, and M. Xiao, Opt. Lett. **31**, 3647 (2006).

101. D.V. Brazhnikov, A.V. Taĭchenachev, A.M. Tumaĭkin, V.I. Yudin, S.A. Zibrov, Ya.O. Dudin, V.V. Vasil'ev, and V.L. Velichansky, JETP Lett. **83**, 64 (2006).

102. J. Dimitrijević, Z. Grujić, M. Mijailović, D. Arsenović, B. Panić, and B. M. Jenković, Opt. Exp. **16**, 1343 (2008).

103. H. Zheng, Y. Zhang, U. Khadka, R. Wang, C. Li, Z. Nie, and M. Xiao, Opt. Exp. **17**, 15468 (2009).

104. A.M. Akulshin, S. Barreiro, and A. Lezama, Phys. Rev. A **57**, 2996 (1998).

105. C. Goren, A.D. Wilson-Gordon, M. Rosenbluh, and H. Friedmann, Phys. Rev. A **67**, 033807 (2003).

106. E. F. McCormack and E. Sarajlic, Phys. Rev. A **63**, 023406 (2001).

107. S. Williams, E. A. Rohlfing, L. A. Rahn, and R. Zare, J. Chem. Phys. **106**, 3090 (1997).

108. H. S. Moon, W. K. Lee, L. Lee and J. B. Kim, Appl. Phys. Lett. **85**, 3965 (2004).

109. H. R. Noh and H. S. Moon, Phys. Rev. A **84**, 053827 (2011).

110. R. Gupta, S. Chang, C. Tai, and W. Happer, Phys. Rev. Lett. **29**, 695 (1972).

111. J. E. Bjorkholm and P. F. Liao, Phys. Rev. Lett. **33**, 128 (1974).

112. B. Chatel, J. Degert, S. Stock, and B. Girard, Phys. Rev. A **68**, 041402 (2003).

113. M. C. Stowe, A. Pe'er, and J. Ye, Phys. Rev. Lett. **100**, 203001 (2008).

114. H. J. Eichler, P. Gunter, and D. W. Pohl, Laser-induced dynamic gratings (Springer, Berlin, 1986).

115. A. M. C. Dawes et al., Science **308**, 672 (2005).

116. Y. Q. Li et al., Phys. Rev. Lett. **78**, 3105 (1997).

117. H. Wang et al., Opt. Lett. **25**, 1732 (2000).

118. H. Wu and M. Xiao, Opt. Lett. **32**, 3122 (2007).

119. A. Abramovici et al., Science **256**, 325 (1992).

120. P. A. Coe, D. F. Howell, and R. B. Nickerson, Meas. Sci. Technol. **15**, 2175 (2004).

121. N. P. Georgiades, E. S. Polzic, and H. J. Kimble, Opt. Lett. **21**, 1688 (1996).

122. R. E. Slusher et al., Phys. Rev. Lett. **55**, 2409 (1985).

123. M. Xiao, L. A. Wu, and H. J. Kimble, Phys. Rev. Lett. **59**, 278 (1987).

124. W. N. Plick, J. P. Dowling, and G. Agarwal, New J. Phys. **12**, 083014 (2010).

125. J. Jing, C. Liu, Z. Zhou, Z. Y. Ou, and W. Zhang, Appl. Phys. Lett. **99**, 011110 (2011).

126. H. Lee, P. Kok, and J. P. Dowling, J. Mod. Opt. **49**, 2325 (2002).

127. V. Giovannetti, S. Lloyd, and L. Maccone, Science **306**, 1330 (2004).

128. V. Giovannetti, S. Lloyd, and L. Maccone, Nat. Phot. **5**, 222 (2011).

129. D. Hillerkuss et al., Nature Photonics **5**, 364-371 (2011), and references therein.

130. J. S. Aitchison, A. M. Weiner, Y. Silberberg, D. E. Leaird, M. K. Oliver, J. L. Jackel, and P. W. E. Smith, Opt. Lett. **16**, 15 (1991).

131. M. Shalaby and A. Barthelemy, Opt. Lett. **16**, 1472 (1991).

132. M. Shalaby, F. Reynaud, and A. Barthelemy, Opt. Lett. 17, 778 (1992).

133. V. Tikhonenko, J. Christou, and B. Luther-Davies, Phys. Rev. Lett. **76**, 2698 (1996).

134. M-F. Shih, M. Segev, and G. Salamo, Phys. Rev. Lett. **78**, 2551 (1997).

135. H. Meng, G. Salamo, M-f. Shih, and M. Segev, Opt. Lett. **22**, 448 (1997).

136. G. I. Stegeman and M. Segev, Science **286**, 1518 (1999).

137. G. I. Segeman, D. N. Christodoulides, and M. Segev, IEEE Journal on Selected Topics in Quantum Electronics **6**, 1419 (2000).

138. S. Trillo, and W. E. Torruellas (eds.), Spatial Solitons (Springerlink, NY, 2001).

139. R. Y. Chiao, E. Garmire, and C. H. Townes, Phys. Rev. Lett. **13**, 479 (1964).

140. P. L. Kelley, Phys. Rev. Lett. **15**, 1005 (1965).

141. J. E. Bjorkholm and A. Ashkin, Phys. Rev. Lett. **32**, 129 (1974).

142. Y. Silberberg, Opt. Lett. **15**, 1282 (1990).

143. Z. Jovanoski, J. Mod. Opt. **48**, 865 (2001).

144. T. Hong, Phys. Rev. Lett. **90**, 183901 (2003).

145. Y. Wu and L. Deng, Phys. Rev. Lett. **93**, 143904 (2004).

146. H. Shpaisman, A. D. Wilson-Gordon, and H. Friedmann, Phys. Rev. A **71**, 043812 (2005).

147. H. Michinel, M. J. P-Alonso, and V. M. P-Garcia, Phys. Rev. Lett. **96**, 023903 (2006).

148. D. D. Yavuz, Phys. Rev. A **75**, 041802(R) (2007).

149. G. Huang, C. Hang, and L. Deng, Phys. Rev. A **77**, 011803(R) (2008).

150. H-J. Li., L. Dong, C. Hang, and G. Huang, Phys. Rev. A **83**, 023816 (2011).

151. H-J. Li, Y-P. Wu, and G. Huang, Phys. Rev. A **84**, 033816 (2011).

A. Publications of dissertation author

A1. Journal papers

15. "Observation of phase-dependent fusion between two ultra-weak optical beams using atomic coherence",
Utsab Khadka, Jiteng Sheng and Min Xiao,
In final preparation.

14. "Measurement of two independent phase-shifts using coupled parametric amplifiers",
Utsab Khadka, Jiteng Sheng, Xihua Yang and Min Xiao,
*New Journal of Physics **14**, 043026 (2012). [arXiv:1112.4880v1].*

13. "Noise correlations in a doubly-resonant atomic optical parametric oscillator",
Jiteng Sheng, Haibin Wu, Xihua Yang, **Utsab Khadka**, and Min Xiao,
Opt. Lett., accepted February 2012.

12. "Four-wave-mixing between the upper excited states in a ladder-type configuration",
Utsab Khadka, Huaibin Zheng, and Min Xiao,
*Opt. Express **20**, 6204 (2012).*

11. "Generation of correlated and anticorrelated multiple fields via atomic spin coherence",
Xihua Yang, Jiteng Sheng, **Utsab Khadka**, and Min Xiao,
*Phys. Rev. A **85**, 103824 (2012).*

10. "Interferometric control of parametrically-amplified waveforms",
Utsab Khadka, Huaibin Zheng, and Min Xiao,
*Phys. Rev. A **84**, 043814 (2011).*

9. "Three-field noise correlation via third-order nonlinear optical processes",
Huaibin Zheng, **Utsab Khadka**, Jianping Song, Yanpeng Zhang, and Min Xiao,
*Opt. Lett. **36**, 2584 (2011).*

8. "All-optical switching in an N-type foul-level atom-cavity system",
Jiteng Sheng, Xihua Yang, **Utsab Khadka**, and Min Xiao,
*Opt. Express **19**, 17059 (2011).*

7. "Simultaneous control of two four-wave-mixing fields via atomic spin coherence",
Xihua Yang, Jiteng Sheng, **Utsab Khadka**, and Min Xiao,
*Phys. Rev. A **83**, 063812 (2011).*

6. "Measurement of ac-Stark shift by a two-photon dressing process via four-wave mixing",
Huaibin Zheng, **Utsab Khadka**, Jianping Song, Yanpeng Zhang, and Min Xiao,
*Europhys. Lett. **93**, 23002 (2011).*

5. "Control of multitransparency windows via dark-state phase manipulation",
Utsab Khadka, Yanpeng Zhang, and Min Xiao,
*Phys. Rev. A **81**, 023830 (2010).*

4. "Modulating the multi-wave mixing processes via the polarizable dark states",
Huaibin Zheng, Yanpeng Zhang, **Utsab Khadka**, Ruimin Wang, C. Li, Z. Nie, and Min Xiao,
*Optics Express **17**, 15468 (2009).*

3. "Temporal and spatial interference between four-wave and six-wave mixing channels",
Yanpeng Zhang, **Utsab Khadka**, Blake Anderson, and Min Xiao,
*Phys. Rev. Lett. **102**, 013601 (2009).*

2. "Spatial interference between four- and six-wave mixing signals",
Blake Anderson, Yanpeng Zhang, **Utsab Khadka**, and Min Xiao,
*Opt. Lett. **33**, 2029 (2008).*

1. "Controlling four-wave and six-wave mixing processes in multilevel atomic systems",
Yanpeng Zhang, **Utsab Khadka**, Blake Anderson, and Min Xiao,
*Appl. Phys. Lett. **91**, 221108 (2007).*

A2. Conference presentations

3. "Interferometry with vacuum-amplified waveforms",
Utsab Khadka, Huaibin Zheng and Min Xiao,
CLEO: QELS 2011, Paper QThS5, Baltimore, Maryland (May 1, 2011).

2. "Four-wave-mixing between the upper-excited states in a cascade configuration",
Utsab Khadka, Huaibin Zheng and Min Xiao
Frontiers in Optics (FiO) 2010, Paper FWZ5, Rochester, New York (October 24, 2010).

1. "Spatial and temporal interferences between four-wave mixing and six-wave mixing channels",
Utsab Khadka, Yanpeng Zhang, Blake Anderson and Min Xiao
Int. Quantum Electronics Conf. (IQEC) 2009, Paper IWB5, Baltimore, MD (May 31, 2009)